View metadata, citation and similar papers at core.ac.uk

brought to you by CORE

provided by Clemson University: TigerPrints

Clemson University
TigerPrints

All Dissertations | Dissertations

8-2010

Modeling of Cell Transfer and Process-Induced Cell Damage in Laser-Assisted Cell Direct Writing

Wei Wang
Clemson University, wwang@clemson.edu

Follow this and additional works at: https://tigerprints.clemson.edu/all_dissertations

 Part of the Engineering Mechanics Commons

Recommended Citation
Wang, Wei, "Modeling of Cell Transfer and Process-Induced Cell Damage in Laser-Assisted Cell Direct Writing" (2010). *All Dissertations*. 590.
https://tigerprints.clemson.edu/all_dissertations/590

This Dissertation is brought to you for free and open access by the Dissertations at TigerPrints. It has been accepted for inclusion in All Dissertations by an authorized administrator of TigerPrints. For more information, please contact kokeefe@clemson.edu.

MODELING OF CELL TRANSFER AND PROCESS-INDUCED CELL DAMAGE IN LASER-ASSISTED CELL DIRECT WRITING

A Dissertation
Presented to
the Graduate School of
Clemson University

In Partial Fulfillment
of the Requirements for the Degree
Doctor of Philosophy
Mechanical Engineering

---

by
Wei Wang
August 2010

Accepted by:
Dr. Yong Huang, Committee Chair
Dr. Richard Miller
Dr. Lonny Thompson
Dr. Gang Li

ABSTRACT

Laser-assisted cell direct-write technique has been obtaining more and more attention in different biomaterial direct writing applications. A typical laser-assisted cell direct-write process can be divided into two main stages: the cell droplet ejection and cell droplet landing. The objective of this study is to model the cell mechanical profile during the cell droplet ejection and cell landing and further model the cell damage.

The possible cell damage during the droplet ejection process in laser-assisted cell direct writing may come from two different sources: the phase explosion-induced bubble expansion and the thermoelastic stress wave. The bubble expansion-induced stress wave is the dominant effect in ejection. It is found that the cell velocity increases initially and then smoothes out gradually with a constant ejection velocity. Both the cell acceleration and pressure can be very high at the beginning period of bubble expansion and then quickly approach zero in an oscillation manner. A high viscosity can lead to an observable velocity increment at the initial stage, but the ejection velocity decreases. The pressure magnitude decreases when the cell-bubble distance is large, and a larger initial pressure induces a larger cell pressure as expected. If the thermal and stress confinement conditions are satisfied, the thermoelastic stress wave may introduce an alternative impact to cells to be transferred in laser-assisted cell direct writing. It is found that a bipolar pressure pair has been developed within a finite thin coating medium. The stress waves reflected from the coating-air free surface change its sign and have decreasing magnitude when traveling inside the coating. Shorter duration laser pulses lead to higher thermoelastic stresses and higher laser fluence leads to higher thermoelastic stresses.

The impact between the cell and the receiving culture coating/substrate during the cell landing may lead to cell damage. It is found that the cell membrane usually undergoes a relatively severe deformation and the cell mechanical loading profile is dependent on the cell droplet initial velocity and the substrate coating thickness. Generally, a larger initial velocity poses a higher probability of cell damage, and a substrate coating can significantly reduce the cell mechanical damage severity.

A new mathematical approach was proposed to biophysically predict the biofabrication-induced cell damage based on the triggered molecular signaling pathway in the cellular network. The proposed cell damage model includes two characteristics: 1) the cell may be dead only when the external stress exceeds a certain threshold value. Below this value, the cell does not commit any fate decision; and 2) if the external stress is higher than the threshold stress, the signaling pathway is triggered and may cause cell death depending on the time accumulative effect of external stress. That is, cell damage depends on the stress threshold, the external stress magnitude and its duration. This cell damage model is validated in damage modeling of a muscle-skin tissue and shows a good prediction of cell viability in laser assisted cell direct writing. More importantly, the proposed methodology provides a biophysics-based approach to investigate cell damage under influences of a variety of mechanical, chemical and biological environments by considering specific molecular networks in a cell.

In summary, this work modeled the laser-assisted cell direct writing and further modeled the cell damage based on a biophysics understanding.

DEDICATION

This dissertation is dedicated to my parents and my wife who give me great support for my study at Clemson University.

ACKNOWLEDGEMENTS

I wish to express my deepest gratitude to my advisor, Professor Yong Huang. His knowledge, supervision and continuous encouragement throughout this research are indispensible for the accomplishment of this work.

Sincere gratitude is also given to the other members of my dissertation committee, Professor Richard Miller, Professor Gang Li, and Professor Lonny Thompson for their good suggestions and comments during the research. Their interest and appreciation gave me great motivation and confidence to work on this research. I would thank Professor Thomas Boland for his recommendations in this work. I would also thank Dr. Nicole Coutris for her help and discussion throughout my research and study.

I would like to thank my group members: Yu Long, Mason D. Morehead, Kevin Foy, Xiaoyu Wang, Lei Tang, Yafu Lin, Jun Yin, Leigh Herran, and Changxue Xu.

I would like to acknowledge the financial support from the National Science Foundation and the National Textile Center.

Deepest thanks will also be given to my parents. Their support and encouragement give me a good opportunity to study in the United States. At last, I would like to give my special thanks to my wife, Yijun Tuo. She has been supporting me and giving me a lot of encouragement to pursue my research career.

TABLE OF CONTENTS

Page

LIST OF TABLES

LIST OF FIGURES

CHAPTER 1

INTRODUCTION

1.1 Motivation and Objective

Biomaterial direct-write technologies are being favored as rapid prototyping innovations in the areas of tissue engineering, regenerative medicine, and bio-sensor/actuator fabrication based on computer-aided designs (CAD). Direct-write technologies include any techniques or processes capable of depositing, dispensing, or processing different types of materials over various surfaces. During a typical direct-write approach, patterns or layered structures are built directly using a CAD design without the use of masks, allowing rapid prototyping of three dimensional constructs. Among the available direct-write technologies, inkjet and laser-based technologies have been most pioneered to precisely position both nonviable and viable biological patterns and constructs over different substrates (Wang et al. 2008) under non-contact, maskless, and low temperature conditions.

Laser-assisted cell direct writing has been obtaining more and more attention in different biomaterial direct writing applications (Barron et al. 2004a; Ringeisen et al. 2004; Ringeisen et al. 2006; Lin et al. 2009a) since it does not have any specific viscosity requirements as ink-jetting methods do. Unlike ink-jetting or manual spotting techniques, the laser-assisted process delivers small volume of biomaterials without the use of an orifice, thus eliminating potential clogging issues and enabling diverse classes of biomaterials to be deposited.

As shown in Fig. 1.1, a typical laser-assisted cell direct-write process can be divided into two main stages: 1) the cell droplets are formed and ejected due to the laser energy converted momentum and 2) the cell droplets land onto a receiving substrate after traveling through a writing height. During the above two stages, the cells may undergo a severe mechanical deformation which poses a potential mechanical damage to the cells. During the cell droplet ejection, cells exposed to laser-induced stress waves are subject to structural and functional injuries. During the cell landing, the ejection velocity of a propelled droplet and the thickness of the film on the receiving substrate are very critical to a viable transfer. These processes must be carefully studied to understand the cell damage due to mechanical stresses.

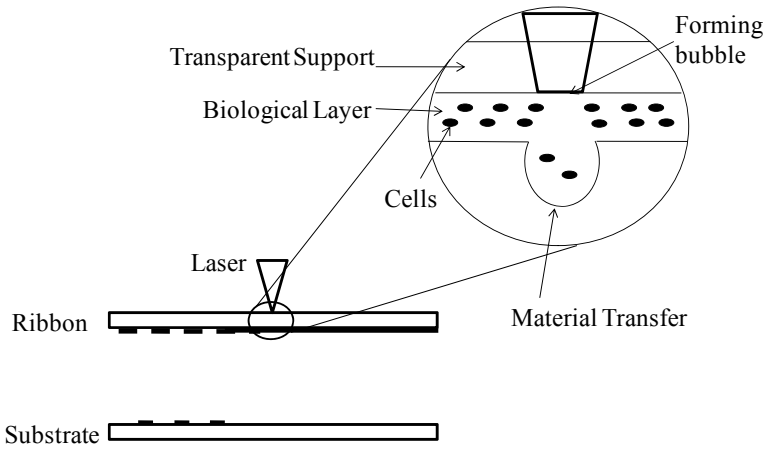

Figure 1.1: Schematic of a typical laser-assisted cell direct writing

In order to commercially implement the different direct-write technologies in the healthcare industry, some biomanufacturing issues need to be carefully addressed. Previous research indicated that under certain conditions laser-assisted cell direct writing yielded cell viabilities greater than 50%. Coatings thicker than 40 μm resulted in near

100% viability (Ringeisen et al. 2004). However, manufacturing process-induced damage to cells, especially fragile mammalian cells, still poses a significant challenge to achieve a perfect cell post-transfer viability. The process-induced cell damage must be carefully addressed for cell direct writing to be a viable technology.

Although some experimental work has been done in the study of the cell viability under different operating conditions in printing cells, the theoretical and/or computational investigation of these processes and the study of the process-induced cell damage are still lacking. The research in this dissertation will fill in this gap, which will facilitate the optimization and wide application of laser-assisted cell direct writing in tissue regeneration research.

The objective of this dissertation is to model the cell mechanical profile during the cell droplet formation and cell landing and further model the cell damage using the cell mechanical profile in laser-assisted cell direct writing. The cell mechanical profile may include the velocity, acceleration, pressure, etc., and the von Mises stress is used to study cell damage in this study. The main content of this work includes four parts: 1) computational modeling of the bubble expansion-induced cell mechanical loading profile in laser-assisted cell direct writing. To validate the modeling accuracy of the finite element method (FEM), the simplified Rayleigh bubble dynamics model-based approach is implemented in an infinite domain to benchmark the FEM method in modeling the cell velocity due to the bubble expansion; 2) to better understand the effect of thermoelastic stress on the cell damage in laser-assisted cell direct writing, the thermoelastic stress wave propagation is modeled by considering the unique boundary conditions in laser-assisted cell direct writing; 3) the smooth particle hydrodynamic (SPH) method, which is

meshfree-based, is used in this study to model large deformations during the cell-hydrogel coating impact process. The representative simulation results are presented and further discussed to appreciate the mechanical effect of process variables on the cell von Mises stress, vertical acceleration, and maximum shear strain component; 4) a new mathematical approach is proposed to biophysically predict the biofabrication-induced cell damage based on the triggered molecular signaling pathway in the cellular network. The key contribution is to elucidate and model how an external stress signal leads to cell death in a dynamic process. More importantly, the proposed methodology provides a biophysics-based approach to investigate cell damage under influences of a variety of mechanical, chemical and biological environments by considering specific molecular networks in a cell.

1.2 Research Background

1.2.1 Process of Matrix-Assisted Pulsed-Laser Evaporation Direct-Write

Among the available direct-write technologies, inkjet and laser-based technologies have been most pioneered to precisely position both nonviable and viable biological patterns and constructs over different substrates. Successful inkjet printing endeavors include *E. coli* bacteria (Xu et al. 2004) and viable mammalian cells (Xu et al. 2005a) deposition using a modified thermal inkjet printer. Laser-based technologies mainly include the use of laser light to form living cell clusters (Odde et al. 2000), matrix-assisted pulsed-laser evaporation direct-write (MAPLE DW) to deposit two dimensional (2D) (Ringeisen et al. 2004) and three dimensional (3D) (Barron et al. 2004b) mammalian cellular structures, and absorbing film-assisted laser-induced forward

transfer (Hopp et al. 2005) to assist rat Schwann and astroglial cell deposition. Recently, the electrohydrodynamic jetting (EHDJ) method has also been successfully demonstrated to print viable cells (Ringeisen et al. 2006). Using a bottom-up approach, different direct-write methods are envisioned to seed cells and biomolecules to mimic natural tissues which would yield an enhanced approach for regenerative growth of tissue implants.

Laser-assisted cell direct writing is favored in this research. Figure 1.2 depicts a classical print setup and landing process schematic using matrix-assisted pulsed-laser evaporation direct-write (MAPLE DW) at Clemson University, SC. As shown in Fig. 1.2, during a typical laser-assisted cell direct writing, focused highly energetic laser pulses are directed through the backside of the quartz support, over which the cell-based biomaterial is coated. These pulses are then absorbed by a laser-absorbing matrix of the biomaterial coating. Once the laser-absorbing material absorbs most of the laser pulse energy, it evaporates and forms a bubble due to localized heating. Finally, this sublimation releases the remaining coating as a droplet from the interface by ejecting it away from the quartz support to the movable receiving substrate underneath, to form two or three-dimensional structures by controlled droplet deposition. The MAPLE DW technique has demonstrated the ability to deposit scaffolding material, biomolecules, and living mammalian cells at the 10 μm to 100 μm (Ringeisen et al. 2004).

The schematic of the cell droplet formation in the first stage is shown in Fig. 1.1. In laser-assisted cell direct writing, upon the absorption of laser pulse energy, the matrix material of the biomaterial coating is first vaporized into gaseous phase products and may be further ionized into plasma, forming a bubble in the cell-based biomaterial coating along the quartz support interface. The bubble starts to expand due to the pressure inside

the bubble. The bubble expansion results in the ejection of the beneath biomaterial away from the coating layer and forms cell droplets. Since the expansion of the gas bubble is inhibited by surrounding media, the confining effect results in significant higher pressure and temperature than ablation in a gaseous environment (Vogel et al. 2003). When the laser-induced stress wave possess a sufficiently short rise time, their propagation may result in the formation of a shock wave (Vogel et al. 2003; Vogel et al. 1996).

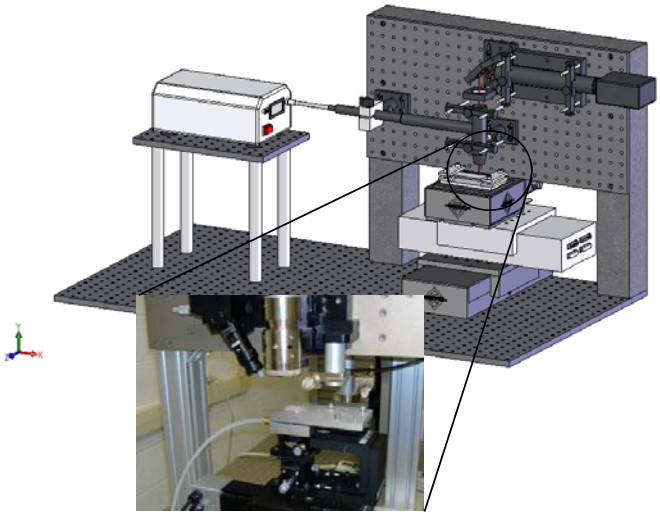

Figure 1.2: Experimental setup in MAPLE DW

The thermoelastic stress wave may introduce an alternative impact to cells to be transferred in laser-assisted cell direct writing even if the incident laser pulse energy is not high enough to induce the vaporization or optical breakdown of coating materials. Generally speaking, the thermoelastic stress is caused by the localized heating and thermal expansion of a material. Two confinement conditions are necessary for the prominent generation of the thermoelastic stress: 1) the pulse duration should be much shorter than the characteristic thermal relaxation/diffusion time; and 2) the pulse duration

should be also shorter than the characteristic acoustic relaxation time to achieve a high-amplitude thermoelastic stress wave (Paltauf et al. 1998; Georgiou et al. 2003).

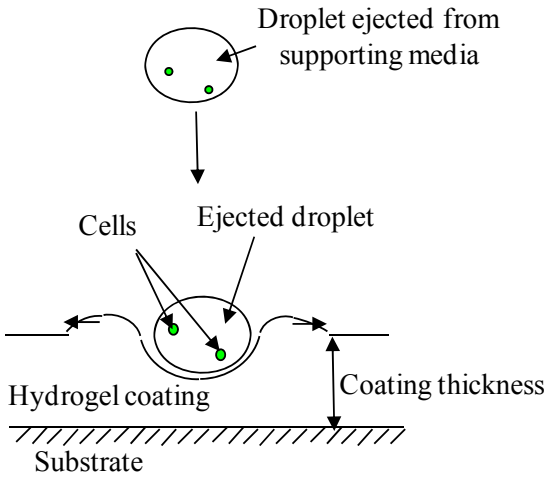

Figure 1.3: Schematic of cell landing onto the receiving substrate

The second stage is the cell landing. A typical schematic is shown in Fig. 1.3. Once a cell droplet, typically enclosed by a hydrogel, is ejected from a supporting medium with an initial velocity, it travels through the air first. Eventually, the cell droplet reaches a receiving substrate, typically a glass slide coated with the hydrogel that allows for cell adhesion and growth and cell impact reduction during landing. During landing, cells penetrate into the cell coating. In the subsequent process, cells continue to move in the coating. If the velocity is high enough, cells may impact with the rigid glass slide. This impact is usually referred as a second impact in cell landing. During these processes, cells undergo significant deceleration and impact(s) and survive a much higher external force than they are capable of under steady state conditions.

The outcome of droplet impact depends on the landing velocity, its direction relative to the surface, droplet size, the properties of the liquid (its density, viscosity,

viscoelasticity, and some other effects for rheologically complex fluids). The impact velocities in MAPLW DW typically range from 50 m/s to 1000 m/s (Young et al. 2001). In high velocity impact, liquid compressibility becomes important and the elasticity is negligible compared to inertial effects. Gravity effects are usually characterized by the Froude number $Fr = V^2 / gD$ (V is the impact velocity, g is the gravity acceleration and D is the droplet diameter). Thus, gravity is typically negligible in the droplet impact.

1.2.2 Cell Damage

All living cells dwell in a mechanical environment. The physical forces can be converted into biochemical signals which are integrated into cellular response of cells. The process is called mechanotransduction (Huang et al. 2004). The effect of external loading on tissues, cells, organelles and macromolecules have been extensively investigated in diverse fields, including laser-generated stress wave (Lee et al. 1997), ultrasound-induced shock wave (Sundaram et al. 2003), high pressure (Yamaguchi et al. 2008), UV irradiation (Scoltock et al. 2004), and shear stress (Tzima et al. 2005; Fitzgerald et al. 2008). Cells may be injured as a result of the mechanical and irradiation stimuli. The mechanisms underlying the damage are very complex since a lot of factors, e.g., heat shock (Rylander et al. 2005), mechanical stresses (Bilek et al. 2003), exposure time (Leverett et al. 1972), etc., come into play in the biological response of tissues. Although the response of tissues and cells exposed to the external loadings has been the subject of considerable studies (Leverett et al. 1972; Doukas et al. 1993; Doukas et al. 1995; Doukas et al. 1996; Doukas 1998; Bilek et al. 2003), an investigation of the

mechanism underlying the induction of cell injury in dynamic mechanical environments has not been studied yet.

During the laser-assisted cell direct writing, cells may undergo a severe mechanical deformation. The cells in the ejected material experience very high acceleration. In the previous studies, it has been found that the acceleration is as high as $10^7 g$-$10^8 g$ (g is gravity acceleration) in the ejection process (Hopp et al. 2005; Wang et al. 2008). A similar acceleration experience was also observed in the cell landing process (Ringeisen et al. 2004). The cell droplets impact on the receiving substrate with an initial velocity after ejection from the coating of the ribbon. Cells undergo deceleration over the short duration (Ringeisen et al. 2004). This severe deceleration due to the impact between the cells and the receiving substrate may lead to membrane rupture and even cell damage (Ringeisen et al. 2004). During the cell landing process, the thickness of the coating on the receiving substrate is of importance to achieve desirable cell viability. Based on Ringeisen's study, 5% cell viability after printing was achieved using an uncoated quartz receiving substrate; however, roughly 50% of the cells transferred onto a thinner hydrogel coating (20 μm) appeared to remain viable posttransfer, whereas viability reached 95% for cells transferred onto a thicker coating (40 μm) (Ringeisen et al. 2004).

Shear stress-induced cell damage has been intensively studied in the laminar flow and turbulent hydrodynamic flow on animal cells (Leverett et al. 1972; Born et al. 92). Leverett et al. studied the red blood cell damage in a rotational viscometer (Leverett et al. 1972). Midler and Finn used a coaxial cylindrical viscometer to study the protozoa damage induced by shear stresses (Milder et al. 1966). They found a rapid initial loss and a secondary damage at a lower rate. The secondary damage might be due to the fatigue

effects or some more subtle phenomena such as retard biosynthetic activity (Al-Rubeai et al. 1990). Born et al. (Born et al. 1992) modeled cell damage based on the duration-independent laminar shear stress-induced cell membrane tension.

Shear stress often occurs during the shock wave generation and bubble collapse process. In pulsed laser ablation of biological tissues, rapid laser energy deposition induces hot vapor or plasma formation. The expansion of the gaseous phase into the surrounding air generates acoustic transients which evolve into shock wave for very high energy densities in the ablated materials (Vogel et al. 2003). Due to the pressure and temperature increase caused by the phase explosion or laser plasma, an initial bubble with high internal energy expands. The wall of the initial gas bubble travels at supersonic speeds for nanosecond pulses and subsonic speeds for picoseconds pulses (Vogel et al. 1996). The rapid growth of bubble induces high pressure on the adjacent cell culture media and damages the cells by shear forces. When the bubble reaches its maximum expansion, it will undergo collapse due to the huge pressure difference between the inside and outside medium. When the adjacent fluid rushes into the cavity, a significant shear stress applies on cells in this area.

The source of shear stress may also come from pressure gradient. The large pressure gradients are produced in the vicinity of a bubble and lead to local rupture of the tissue. Pressure gradients create imbalances of the normal stresses on the cell membrane over the length of the cell which results in nonuniform cell compression, leading to "pinching" of the cell and rupturing of the cell membrane (Bilek et al. 2003).

Tensile stress can also result in tissue damage. The tissue is more susceptible to the tensile stress than to the compressive stress. In laser-induced tissue ablation, the recoil

stress and thermoelastic stress are often the sources of tissue damage by generating the tensile stresses on the tissue.

The flow of ablation products perpendicular to the tissue surface induces a recoil pressure that may result in additional material impulsion and damage to the tissue. The tensile stress can be produced if the compressive recoil stresses are partially reflected at the free surface or at the interfaces with materials of lower acoustic impedance. The tensile stress, which can reach up to 3.5 MPa due to the recoil stress wave, has been demonstrated by Pini et al. (Pini et al. 1996).

Thermoelastic stresses usually contain a tensile stress component which emits from the edge of the laser spot when the dimension of the irradiated spot is comparable with the penetration depth (Paltauf et al. 1998). Many studies have been done to study the effect of these tensile stresses on tissues and fluid surface by causing cavitation bubbles and spallation (Dingus et al. 1991; Paltauf et al. 1992). It is known that the thermoelastic stresses with an amplitude of 9.5 MPa can induce the breakage of viruses (Cleary et al. 1994). In the case of ablation in the air-tissue interface, a positive pressure wave is reflected on the free surface and forms a bipolar stress wave.

Time duration of the mechanical forces is important and influences the cell damage as many investigators observed (Leverett et al. 1972; Tschumperlin et al. 2000). Therefore, in order to fully understand the physical mechanism underlying the stress-induced cell damage, time effect must be taken into account. Some studies discussed the effect of loading duration on cell damage. Leverett et al. discussed the time effect in the study of red blood cell injury (Leverett et al. 1972). Tschumperlin et al. studied the injury

of alveolar epithelial cells with the effect of time duration, deformation peak value and frequency (Tschumperlin et al. 2000).

The mechanism of the mechanical stresses on the cell damage is complex. Recent research reveals that a lot of stimuli trigger the programmed cell death in a caspase dependent manner (Scoltock et al. 2004; Yamaguchi et al. 2008). Apoptosis is the major cause of cell death in cell culture systems (Cotter et al. 1995). It is well known that in response to a variety of mechanical and chemical stimuli, cells can initiate the signaling events, which lead to apoptosis, characterized by a number of specific changes, including chromatin condensation, cytoplasmic condensation, membrane blebbing, and internucleosomal fragmentation of DNA (Scoltock et al. 2004). Cells cultivated in bioreactors are sensitive to changes in their extracellular environment, including nutrient deprivation, O2 limitation, waste accumulation and excessive shear stress (Arden et al. 2004). Nuclear and cell membrane effects can contribute to cell apoptosis independently due to exposure to UV radiation (Kulms et al. 1999).

It has been found that the mechanical signals may induce the regulation of pathways through transforming into a biological signal, leading to the activation of effector caspases, which are cysteine proteases with specificity for aspartic acid residue (Apenberg et al. 2003; Sahoo et al. 2006; Yamaguchi et al. 2008). Sahoo et al. demonstrated that shear stress led to apoptosis-like cell death in *Bacillus subtilis* (Sahoo et al. 2006). Yamaguchi et al. demonstrated that caspase 3 was activated in the pressure-induced apoptosis of murine erythroleukemia (MEL) cells through both intrinsic and extrinsic pathways (Yamaguchi et al. 2008). Apenberg et al. found that the apoptosis of the vascular smooth muscle cells (VSMCs) was induced by shear stress via an autocrine

fas/fasL pathway although the mitochondria-associated pathway was also involved (Apenberg et al. 2003). Fitzgerald et al. concluded that laminar shear stress stimulated VSMC apoptosis via the intrinsic pathway, which was regulated by the Akt pathway (Fitzgerald et al. 2008). In situ detection of activated caspases, the enzymatic mediators of the apoptosis cascade showed that these proteases were involved in shear-induced apoptosis and were activated in a shear-dependent manner (Shive et al. 2002).

Cells usually trigger apoptosis through two pathways: intrinsic pathway and extrinsic pathway. Both pathways can be triggered either separately (Eissing et al. 2004; Zhang et al. 2009) or independently in an additive manner (Kulms et al. 1999). The intrinsic pathway is activated by various cellular stresses, including staurosporine treatment, serum deprivation, oxidative stress and DNA damage. In this pathway, the rupture of mitochondrial membrane results in the release of proapoptotic proteins from the mitochondrial intermembrane space into the cytoplasm. The released proteins include cytochrome c and the second-mitochondria-driven activator of caspase (SMAC). In the cytoplasm, cytochrome c binds to APAF-1 to form an apoptosome, which activates caspase 9 and the downstream effector caspase, caspase 3. Extrinsic pathway signaling is mediated by the activation of "death receptors" such as Fas (CD95) or the members of tumor necrosis factor receptor (TNF-R) superfamily. Binding of death ligands and their death receptors usually induce the oligomerization of the associated death receptors, followed by recruitment of adaptor proteins Fas-associated death domain proteins (FADD) to the cytoplasmic portions of the receptor (Bagci et al. 2006). FADD then recruits procaspase 8, resulting in the formation of death-inducing signaling complex (DISC) and ultimately provokes caspase 8 activation. Two types of cells have been

recognized based on their sensitivity to Fas-induced apoptosis (Jost et al. 2009). In type I cells, such as lymphocytes and thymocytes (Jost et al. 2009), the death-inducing signaling complex is easily formed. Activation of caspase 8 leads to the activation of other caspases, including the executioner caspase 3, which ultimately results in cell apoptosis. This direct and main caspase-dependent apoptosis pathway usually occurs when the amount of activation of caspase 8 is large. On the contrary, small amount of caspase 8 requires signaling amplification via the mitochondria-dependent apoptosis for type II cells (Bagci et al. 2006) such as hepatocytes and pancreatic β cells (Jost et al. 2009). This process is initiated by the cleavage of Bid. The truncated BID (tBid) translocates to the mitochondria, where it acts with the Bcl-2 family members BAX and BAK. Cytochrome c and SMAC are then released to the cytoplasm. Cytochrome c can bind to Apaf-1 to activate caspase 9 molecules, which in turn activate caspase 3, ultimately resulting in cell death. The type I cell was analyzed in this study. One important reason is that it is the main route for the extrinsic pathway especially when the death-inducing signaling complex (DISC) formation is strong.

1.3 Current State of Research

1.3.1 Modeling of Laser-Induced Bubble Expansion

Laser-induced bubble formation and expansion in different media such as living tissues has been of modeling interest since it was observed (Vogel et al. 1996; Glinsky et al. 2001; Lokhandwalla et al. 2001; Friedman et al. 2002; Vogel et al. 2003; Tomita et al. 2003; Byun et al. 2004; Brujan et al. 2006). Once a bubble nucleus is formed upon absorbing the laser pulse energy, the bubble expansion process and its mechanical effect

on the surrounding medium can be generally modeled in two approaches: analytically and numerically. The analytical approach is mainly based on the Rayleigh bubble dynamics model (Lokhandwalla et al. 2001) and its modified versions, such as the Gilmore bubble dynamics model (Glinsky et al. 2001; Byun et al. 2004; Brujan et al. 2006), to consider the effect of compressible medium and/or include the effect of different medium material properties. However, the analytical approach generally ignores the complexity of material models and it is good for one-dimensional (1D) problems. Alternatively, the finite difference/finite element-based numerical approach has also been applied to capture the one or two dimensional bubble expansion process and its mechanical effect (Glinsky et al. 2001; Friedman et al. 2002). The numerical method allows the consideration of complex bubble and medium geometry as well as enables the application of more realistic material models, which are difficult to be implemented using the analytical approach.

In the case of laser-assisted cell direct writing, the interactions among the expanding bubble and the surrounding cells are of interest in addition to the bubble expansion dynamics modeling. The mechanical effect of the general bubble expansion on the cell stress and velocity has been studied by applying the Rayleigh bubble dynamics model to model the bubble expansion and the bubble-induced flow field method to estimate the cell mechanical profile (Lokhandwalla et al. 2001); however, the whole modeling process and material models are oversimplified for the sake of an analytical solution. To better elucidate the effect of laser-induced bubble expansion on cell damage in laser-assisted cell direct writing, the FEM approach is applied to investigate the cell mechanical profile due to the bubble expansion process.

1.3.2 Modeling of Laser-Induced Thermoelastic Stress Wave

The thermoelastic stress wave has been widely utilized or observed in laser-assisted cleaning (Park 1994) and laser ablation (Paltauf et al. 1997; Paltauf et al. 1998; Vogel et al. 2003) including biological tissue removing (Dingus et al. 1991; Dingus et al. 1994). Many efforts have been done to understand this thermoelastic stress-based photoacoustic effect, which can be both compressive and tensile, due to the absorption of laser radiation in fluids under low laser energy inputs (Carome et al. 1964; Frenz et al. 1996). A high amplitude tensile stress wave can lead to the ejection of material via mechanical rupture of materials (spallation) (Georgiou et al. 2003), which may lead to cell damage in cell direct writing. It should be pointed out that the mechanism of material ejection due to the bipolar thermoelastic stress wave is different from that of the explosive phase change-induced material ejection, which is driven by the high pressure from the expanding bubble (Paltauf et al. 2003).

Previous work has been performed to model the resulting thermoelastic stress wave. If the laser beam size is taken as finite (the laser spot diameter is comparable to the optical penetration depth), the wave generation becomes three dimensional (3D), which can be solved analytically using Green's function; unfortunately, this approach usually assumes that the wave propagation is within a homogenous infinite medium. The image source method has also been explored to model this wave propagation challenge when one of the boundaries is rigid (Paltauf et al. 1998).

The coating layer in laser-assisted direct writing as seen from Fig. 1.1 is usually very thin, and this layer cannot be treated as an infinite medium since the wave is reflected at the free surface. To better understand the effect of thermoelastic stress on the

cell damage in laser-assisted cell direct writing, the thermoelastic stress wave propagation is modeled here by considering the free surface boundary condition in cell direct writing which is different from others (Paltauf et al. 1998).

1.3.3 Modeling of Cell Landing

The cell landing involves complex impact dynamics which is still far from being fully understood. The phenomenon of droplet impact with a rigid surface has been studied by some researchers numerically (Haller et al. 2002) and experimentally (Xu et al. 2005b). When the droplets impact with the surface, the droplets are compressed and deformed continuously before collapse. For high-speed liquid droplet impact, the compressibility of the liquid medium needs to be considered (Haller et al. 2002). The phenomenon in droplet-liquid impact is not well understood. Cossali, Wang, and Rioboo et al. studied single-drop impacts on thin liquid films of the same liquid (Cossali et al. 1997; Wang et al. 2000; Rioboo et al. 2003). In these cases, splashing was studied at sufficiently high impact velocities. Yarin et al. established the experimental threshold velocity for drop splashing in a train of frequency of the impacts (Yarin et al. 1995).

The effect of impact on the cell damage has been obtaining intensive attention since impact-induced high stress causes cell damage. Chan et al. investigated the impact-induced *E. coli* cell damage during processing (Chan et al. 2006). In laser-assisted cell direct writing, the transferred cell droplets decelerate after ejection, and cells are sometimes damaged if the impact between cell and receiving culture coating/substrate leads to cell damage. The ejection velocity of a propelled droplet is very critical to avoid cell damage in the cell landing process when it is deposited onto the receiving substrate. High-speed imaging discovered that the velocities of MAPLE DW-ejected material can

range from 50 to 1000 m/s (Young et al. 2001). Under conservative assumptions, such as linear deceleration over the impact process and a forward velocity of 50 m/s, one-dimensional motion calculations assuming a final velocity of 0 m/s indicate that the cells undergo deceleration at approximately 10^7 m/s^2 for roughly 4 μs of transit through a 100 μm thick gel coating.

Modeling of cell landing in the cell direct-write process is still lacking in the literature. One difficulty lies in the complexity of the impact dynamics. For the computational modeling, the large deformation of the coating materials probably results in a computational breakdown in certain cases. Since the impact process is crucial to the cell viability in laser-assisted cell direct writing, it is important to investigate the impact-induced cell mechanical loading profile in cell landing in terms of stress, acceleration, and maximum shear strain. The cell mechanical loading profile information facilitates the understanding and prediction of the possible impact-induced cell damage.

1.3.4 Cell Damage Model

Some studies (Ringeisen et al. 2004; Ringeisen et al. 2006; Chang et al. 2008; Lin et al. 2009a; Lin et al. 2010a) have been conducted to investigate biofabrication process-induced cell injury. For example, in the study of MAPLE DW-based cell direct writing, there have been some interesting contributions, which include the experimental study of the effect of the coating thickness of the matrigel on the receiving substrate on the post-transfer mammalian cell viability (Ringeisen et al. 2004) and the effect of laser fluence (laser pulse energy / area of laser spot size) on the post-transfer yeast cell viability (Lin et al. 2009a) and human colon cell viability (Lin et al. 2010a) as well as some modeling

attempts regarding the MAPLE DW process-induced mechanical stress profile during bubble expansion and cell droplet landing (Wang et al. 2008; Wang et al. 2009a).

The mechanisms underlying the cell damage are very complex since many factors influence the biological response of tissues. A variety of studies of the cell damage have been done (Born et al. 1992; Lee et al. 97; Lee et al. 1999; Bilek et al. 2003; Sundaram et al. 2003), but most of them focused on the macroscopic stress or strain level (Lee et al. 1999; Sundaram et al. 2003). Born et al. (Born et al. 1992) modeled cell damage based on the duration-independent laminar shear stress-induced cell membrane tension. Sundaram et al. (Sundaram et al. 2003) used the area strain to determine the cell membrane disruption status and cell viability in the presence of ultrasound-induced shock wave or bubble wall motion. Fife et al. (Fife et al. 2006) applied the logistic and Gompertz models to estimate the damage percentage of a biological pesticide using the energy dissipation rate of the complex flow as a damage index. While the above approaches have modeled cell damage as duration independent, some other studies have also considered the effect of loading duration on cell damage (Leverett et al. 1972; Tschumperlin et al. 2000; Bouten et al. 2001; Breuls et al. 2003a; Breuls et al. 2003b). Leverett et al. studied the time effect in the study of red blood cell injury (Leverett et al. 1972). An experimental study of time duration effect and deformation magnitude was conducted in Tschumperlin's work (Tschumperlin et al. 2000). Tschumperlin et al. (Tschumperlin et al. 2000) studied the injury of alveolar epithelial cells with the effect of time duration, deformation peak value and frequency. A couple of features can be found considering the effect of loading duration on cell damage. During a short time, a higher peak value is required to damage a cell. As time increases, a smaller peak value can also lead to cell

damage. The ability to transform a cell from a native to an injured state depends on not only the magnitude of the mechanical profile but also the time duration of exposure to the external loading. To model the time effect on the cell damage, the power law was applied to study red blood cell damage by considering both the shear stress and exposure duration effects (Blackshear et al. 1965; Grigioni et al. 2005). Breuls et al. proposed a damage law which considers the time accumulative effect on the cell damage (Breuls et al. 2003b). This model gave a good prediction of damage evolution of skeletal muscles cells as observed in the in vitro experiments (Breuls et al. 2003a).

However, biological materials such as living cells are much more complex than any other engineering materials in terms of their failure criteria. There is no available systematic study to understand and model cell damage using a combined biological and engineering approach. It is necessary to propose a new mathematical approach to biophysically predict the biofabrication-induced cell damage based on the triggered molecular signaling pathway in the cellular network.

1.4 Organization of This Dissertation

The general frame of this work is shown in Fig. 1.4. The possible cell damage during the droplet formation and subsequent ejection process in laser-assisted cell direct writing may come from two different sources: the phase explosion-induced bubble expansion and the thermoelastic stress wave. In the cell landing, the cell droplets land onto a receiving substrate after traveling through a writing height. The material ejection and cell landing processes are first modeled to investigate the physical processes. The study of these processes helps to understand the cell damage in these processes. At last, a

cell damage model is proposed to biophysically predict the biofabrication-induced cell damage based on the triggered molecular signaling pathway in the cellular network. The predicted effects of laser fluence, cell droplet land velocity, and substrate coating thickness on the post-transfer cell viability match the experimental results reasonably well.

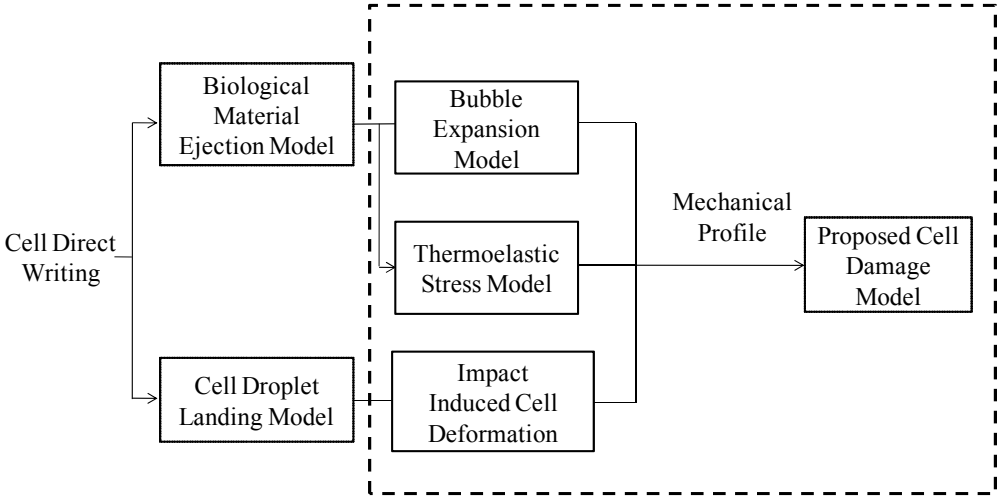

Figure 1.4: Framework of research plan

The organization of this dissertation is as follows:

In Chapter 1, the motivation and objective of this work are first introduced. The research background and the current state of research are then reviewed. Finally, the organization of this dissertation is provided.

In Chapter 2, the bubble expansion-induced cell mechanical loading profile is modeled. The FEM approach is implemented in LS-DYNA to study the cell mechanical profile during ejection here with a different mesh for different computational domains, respectively. The cell is modeled as a hyperelastic material using the Lagrangian mesh for its straightforward and fast implementation, while the bubble, coating medium, and

air are modeled using the Eulerian mesh to avoid any extreme element distortion of these materials during ejection. The complete definition of a transient non-linear dynamics problem requires material models that define the relationships among the flow variables. In this study, four materials, vaporized bubble gas, air, hydrogel (coating material), and cell, are utilized within the computational domain. The evolution of cell center velocity, cell center acceleration, and pressure is studied by using the FEM approach, and the effects of coating viscosity, cell-bubble distance, and initial bubble pressure on the cell mechanical profile are further investigated during cell ejection. The modeled mechanical profile information helps to reveal the cell damage mechanism in laser-assisted cell direct writing.

In Chapter 3, the thermoelastic stress wave propagation is modeled by considering the free surface boundary condition in cell direct writing to better understand the effect of thermoelastic stress on the cell damage in laser-assisted cell direct writing. The proposed computational procedure is first validated with the documented results in modeling the pressure profile near a water-glass interface under laser radiation. Once the modeling methods are validated, the proposed numerical approach is further used to model the thermoelastic stress generation process. The thermoelastic stress profile considering the reflection effect due to the coating-air interface and the rigid coating-glass interface is studied. The governing equation can be solved to obtain the thermoelastic stress within the thin coating layer under the given boundary and initial conditions. The effect of coating absorbing coefficient on the thermoelastic stress wave generation and resulting pressure profiles is also studied. It helps to understand the photomechanical stress and its relevance with biomaterial damage in laser-assisted cell direct writing.

In Chapter 4, the cell-hydrogel coating impact process is studied to model the cell mechanical profile during the cell landing process. The droplets land on the receiving substrate after ejection. Two important impact processes may occur during the cell droplet landing: the first impact between the cell droplet and the substrate coating and the second impact between the cell and substrate. This study assumes that the cell is uniformly enclosed by the hydrogel to form a droplet, and the receiving substrate is also coated with hydrogel. During the cell landing, cells undergo significant deceleration and impact(s) and survive a much higher external force than they are capable of under steady state conditions. This landing process and its induced impact can be modeled using the mass, momentum and energy conservation equations, respectively. To solve the large element distortion challenge in modeling of cell printing process, the smooth particle hydrodynamic (SPH) method, which is meshfree-based, is used in this study to model large deformations during the cell-hydrogel coating impact process. The impact-induced cell mechanical loading profile in terms of the velocity, acceleration, stress and maximum shear strain component during the cell landing is studied. The effect of typical process variables such as the droplet initial velocity and the coating thickness on the cell stress, acceleration and shear strain during the cell landing is carefully studied to understand the cell damage.

In Chapter 5, a new mathematical approach is proposed to biophysically predict the biofabrication-induced cell damage based on the triggered molecular signaling pathway in the cellular network. The model shows how an external stress signal leads to cell death through a dynamic process. The von Mises stress is used in the cell damage

model and it is obtained from the FEM simulation results. The total accumulative effect is obtained by using the numerical integral over the time exposure duration.

At last, as the conclusion and future work of the dissertation, Chapter 6 summarizes the conclusions, contributions and future work of this dissertation.

CHAPTER 2

MODELING OF BUBBLE EXPANSION-INDUCED CELL MECHANICAL PROFILE IN LASER-ASSISTED CELL DIRECT WRITING

2.1 Introduction

During a typical laser-assisted cell direct writing, focused highly energetic laser pulses are directed through the backside of the quartz support, over which the cell-based biomaterial is coated. These pulses are then absorbed by either a laser-absorbing matrix of the biomaterial coating (as in matrix-assisted pulsed-laser evaporation direct-write (MAPLE DW)) or a specific laser-absorbing energy conversion layer between the quartz support and the coating to be transferred (as in Biological Laser Printing (BioLP)). Once the laser-absorbing material absorbs most of the laser pulse energy, it evaporates and forms a bubble due to localized heating in the immediate vicinity of the energy-absorbing material, which is the same for both MAPLE DW and BioLP. Finally, this sublimation releases the remaining coating as a droplet from the interface by ejecting it away from the quartz support to the movable receiving substrate underneath, to form two or three-dimensional structures by controlled droplet deposition.

The aforementioned cell direct writing process can be divided into two main stages: 1) the cell droplets are formed and ejected due to the laser energy converted momentum and 2) the cell droplets land onto a receiving substrate after traveling through a writing height (Wang et al. 2008). During the above two stages, the cells may undergo a severe mechanical deformation which poses a potential mechanical damage to the cells by making cell membrane permeable (Lee et al. 1999) or even membrane rupture. This

chapter focuses on the first stage. The bubble expansion-induced cell mechanical profile is modeled.

Two mechanisms are possibly responsible for cell damage during ejection in laser-assisted cell direct writing: the bubble expansion-induced stress wave and the thermoelastic stress wave (Vogel et al. 2003). The bubble expansion-induced cell mechanical deformation is of interest since it is the dominant effect during ejection. In laser-assisted cell direct writing, upon the absorption of laser pulse energy, the matrix material of the biomaterial coating or the material of the energy conversion layer is first vaporized into gaseous phase products and may be further ionized into plasma, forming a nucleus in the cell-based biomaterial coating along the quartz support interface. The formed nucleus evolves into an expanding bubble, and the bubble expansion-induced pressure ejects the surrounding coating material away, forming cell droplets. Since the expansion of the gas bubble is inhibited by surrounding media, the confining effect results in significant higher pressure and temperature than those due to ablation in a gaseous environment (Vogel et al. 2003). When the laser-induced stress transients possess a sufficiently short rise time, their propagation may result in the formation of a shock wave (Vogel et al. 1996; Vogel et al. 2003).

The objective of this chapter is to numerically investigate the bubble expansion-induced cell mechanical profile during the laser-assisted cell ejection process. While the bubble initial formation process is not of particular interest here, the following bubble expansion-induced cell mechanical profile such as the velocity, acceleration and pressure was studied. Either Lagrangian or Eulerian mesh has been applied for different computational domains to model this cell mechanical profile using a finite element

method (FEM)-based approach. The modeling study enables a quantitative understanding of the cell mechanical profile during the ejection process and helps to understand the process-induced cell damage.

This chapter is organized as follows. Firstly, some assumptions are given for modeling. Secondly, necessary material models are introduced. To validate the modeling accuracy of the FEM method, the simplified Rayleigh bubble dynamics model-based approach is implemented in an infinite domain to benchmark the FEM method in modeling the cell velocity due to the bubble expansion. The validated FEM method is further applied to study the cell mechanical profile such as velocity, acceleration, and pressure during bubble expansion, and the effects of coating viscosity, cell-bubble distance, and initial bubble pressure on the cell pressure are also studied. Finally, the main conclusions are drawn for better cell direct writing process optimization. This study serves as a foundation for further cell damage investigation in various jet-based cell direct-write technologies as they all deal with the interactions between cells and the surrounding medium during the cell droplet formation process.

2.2 Computational Modeling and Its Validation

2.2.1 Problem Statement and Assumptions

Figure 2.1 shows the schematic of the laser-induced bubble formation and expansion in a typical laser-assisted cell direct writing setup (MAPLE DW). While the MAPLE DW schematic is shown here, the proposed modeling approach is still applicable to BioLP by assuming the energy conversion thickness (usually less than 100 nm) negligible. During the bubble expansion process after the bubble is formed, the high

pressure pulse and shock wave are generated, which interact with the cells inside the hydrogel-based cell coating medium. It should be pointed out that the coating medium can be any materials other than hydrogel, which it is commonly used. To model the effect of the bubble expansion on the cells during the cell droplet ejection process, the following assumptions are introduced:

1. The formed bubble geometry, temperature, and pressure right after the material thermal evaporation and/or optical breakdown process are assumed known, and the bubble is modeled as the gaseous phase (Vogel et al. 2003; Brujan et al. 2006). Also, the gas diffusion and further evaporation of biomaterials during the bubble expansion are also ignored.
2. Energy loss due to heat conduction is negligible during the bubble expansion process, and the bubble expansion always moves faster than the speed of heat diffusion (Barron et al. 2004b; Byun et al. 2004);
3. The bubble gas maintains a constant mass, and the gas gain or loss due to the surrounding material evaporation and the gas diffusion through the bubble wall is negligible (Vogel et al. 1996);
4. The cell coating includes only a cell which is directly beneath the center of laser pulse;
5. The initial bubble is semi-spherical (Byun et al. 2004);
6. Since the Froude number (a dimensionless number comparing inertial and gravitational forces) is very large (on the order of 10^7), the gravitational effect is neglected; and

7. Surface tension is not considered. During the ejection process, the Weber number (a dimensionless number comparing the inertial effect to the surface tension effect) is high (on the order of 10^2~10^4), so the effect of surface tension on the cell deformation and motion may be negligible. For the detailed cell droplet formation simulation, the surface tension should also be carefully considered in the future study.

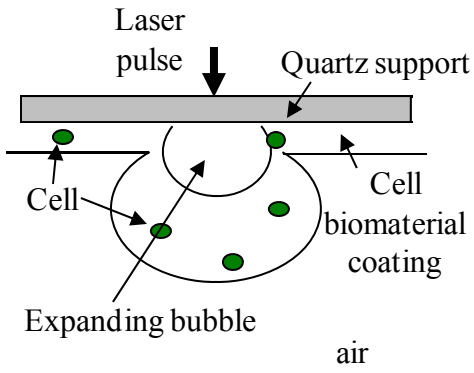

(a)

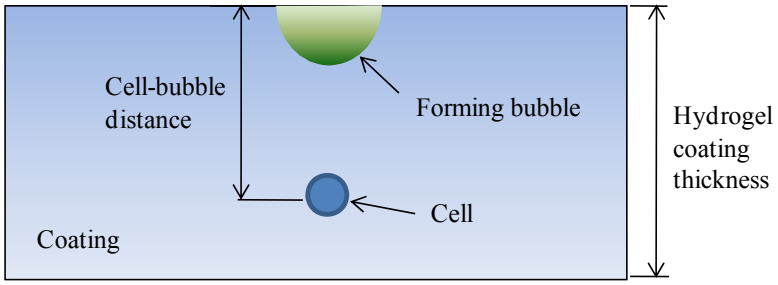

(b)

Figure 2.1: (a) Cell direct writing schematic and (b) modeling domain for the bubble expansion-induced cell deformation

The FEM approach is implemented in LS-DYNA to study the cell mechanical profile during ejection here with a different mesh for different computational domains, respectively. In this study, four materials, vaporized bubble gas, air, hydrogel (coating material), and cell, are utilized within the computational domain, and the following sections briefly introduce the material models adopted for each material. The cell is modeled as a solid type material using the Lagrangian mesh for its straightforward and fast implementation, while the bubble, coating medium, and air are modeled using the Eulerian mesh to avoid any extreme element distortion of these materials during ejection. The Lagrangian domain overlaps over the Eulerian domain while the different Eulerian domains share nodes on the common boundaries. The cell/hydrogel interaction is modeled using the appropriate Euler/Lagrange coupling option (all directions coupling method as in LS-DYNA) to capture the viscosity effect within the cell boundary layer, and the interaction among the hydrogel, bubble gas, and air is modeled by defining these materials in multi-material grouping.

2.2.2 Material Models

The complete definition of a transient non-linear dynamics problem requires material models that define the relationships among the flow variables (pressure, mass density, energy density, temperature, etc.). The following sections briefly introduce the material models of four materials, vaporized bubble gas, air, hydrogel, and cell of the computational domain. These relations generally involve an equation of state, a constitutive equation, and a failure criterion for each constituent material. The numerical simulation is implemented using LS-DYNA 971, and all the material parameters defined

in the remainder of the section are available in the LS-DYNA material library (LS-DYNA 2007).

2.2.2.1 Vaporized Bubble Gas

In laser-assisted cell direct writing, the laser energy-absorbing material along the cell coating-quartz interface (as in MAPLE DW) or of the energy conversion layer (as in BioLP) evaporates upon the absorption of laser pulse energy and may further ionize, forming a bubble within the confined coating domain. For simplicity, the bubble gas is modeled as an ideal gas with an equation of state defined as follows:

$$P_b = \rho_b (C_{P-V} - C_{V-V}) T_b \tag{2.1}$$

where P_b is the bubble pressure, ρ_b is the current mass density, T_b is the temperature, and C_{P-V} and C_{V-V} are defined as the specific heat with respect to the constant pressure and constant volume for the bubble gas, respectively. When the bubble expands, both the density and temperature vary as the bubble volume changes, so does the bubble pressure. The pressure at the initial state (P_{b0}) is defined by the initial mass density and temperature (ρ_{b0} and T_{b0}) as follows:

$$P_{b0} = \rho_{b0} (C_{P-V} - C_{V-V}) T_{b0} \tag{2.2}$$

Since the bubble gas is a gaseous material and has no ability to support either the shear stress or the negative pressure, no failure model is adopted for the bubble gas.

2.2.2.2 Air

As the bubble expands, the expanding bubble applies a pressure wave over the cell coating beneath. The cell coating is pushed towards the surrounding air and consequently forms a cell droplet. In the computational analysis, an Eulerian

computational domain is used to model the surrounding air, and the air equation of state is modeled as follows:

$$P_a = (\gamma_A - 1)\frac{\rho_a}{\rho_{a0}} E_a \tag{2.3}$$

where P_a is the air pressure, $\gamma_A = \frac{C_{P-A}}{C_{V-A}}$ is the air constant pressure specific heat over the constant volume specific heat, ρ_a is the current air mass density, ρ_{a0} is the mass density at the reference state, and E_a is the air internal energy per unit reference volume. Since the air pressure and temperature are much smaller than those of the bubble, the air initial internal energy is set as zero for simplicity. Since air is a gaseous material and has no ability to support either the shear stress or the negative pressure, no failure model is adopted for air.

2.2.2.3 Hydrogel

Natural and synthetic hydrogels contain water within a three-dimensional network of polymer chains (Stammen et al. 2001). By their nature, hydrogels are highly swollen fluid-like solids which are water swollen, cross-linked, hydrophilic polymers. Due to their biocompatibility and the ease of their synthesis, the gels have been already extensively used as cell culture and proposed for a wide range of biomedical applications (Vijayasekaran et al. 1998; Young et al. 1998). The properties of a particular hydrogel are highly dependent on its structure characteristics, constitutes, and chemical environment (Wang et al. 2004; Nam et al. 2005), and some hydrogel mechanical property characterization studies have also been performed (Roeder et al. 2002; Drury et al. 2004;

Lin et al. 2004). However, the knowledge of mechanical properties of hydrogel is still under the development stage.

Equation of state of hydrogel is expected to provide a hydrodynamic material model by which the hydrogel volumetric strength can be determined. Mie-Grüneisen equation of state as shown in Eq. (2.4) is used to define the equation of state of hydrogel to consider the compressibility (LS-DYNA 2007):

$$P_h = \frac{\rho_{h0} C^2 \mu \left[1 + \left(1 - \frac{\gamma_0}{2}\right)\mu - \frac{a}{2}\mu^2\right]}{\left[1 - (S_1 - 1)\mu - S_2 \frac{\mu^2}{\mu + 1} - S_3 \frac{\mu^3}{(\mu + 1)^2}\right]} + E_h(\gamma_0 + a\mu) \tag{2.4}$$

where P_h is the hydrogel pressure, C is the intercept of the U_s-U_p curve (sound velocity) as the U_s axis, U_s is the speed of a shockwave through the material, U_p is the speed of the shocked material, S_1, S_2, and S_3 are the coefficients of the slope of the U_s-U_p curve, γ_0 is the Grüneisen gamma, E_h is the internal energy per initial volume, a is the first order volume correction to γ_0, the compression μ is defined as $\frac{\rho_h}{\rho_{h0}} - 1$, and ρ_h and ρ_{h0} are the density and initial density. The Mie-Grüneisen equation is typically determined based on material parameters c, S_1, S_2, S_3, and γ_0 as specified by LS-DYNA (LS-DYNA 2007). In this study, since water is the dominant component of hydrogel, the parameters for water are used to define the hydrogel equation of state to simplify the problem.

Since the hydrogel demonstrates fluid-like behavior during large deformation, for simplicity, the null material provided by the LS-DYNA material library (LS-DYNA 2007) is used as the hydrogel constitutive model. When using the null material model, the

pressure and deviatoric stress are decoupled. The pressure is determined by the equation of state as Eq. (2.4), and the deviatoric stress is calculated based on the strain rate and viscosity as follows:

$$\sigma^D = 2\eta\dot{\varepsilon}^D \tag{2.5}$$

where η is the hydrogel viscosity, σ^D is the deviatoric stress, and $\dot{\varepsilon}^D$ is the deviatoric strain rate. In addition, the cutoff pressure is used to control the hydrogel failure by allowing the hydrogel to numerically cavitate when hydrogel undergoes dilatation (tensile negative pressure) above a certain value, which is usually zero or a small negative value for liquid-type materials.

2.2.2.4 Cell

During the bubble expansion-induced cell ejection process, the cells undergo complex dynamic pressure and velocity variations, eventually forming the cell droplets. In order to model the complexity of cell structure and compositions, numerous cell constitutive models have been developed to characterize mechanical responses of living cells subject to both transient and dynamic loads (Lim et al. 2006). Generally, cell models can be considered on two levels, macroscopic continuum approaches, and microscopic structural approaches. The continuum approaches aim to investigate the overall behavior of cells while microscopic structural approaches focus on the effect from the local component deformation of cells.

Among the continuum approaches, the hyperelastic formulation, Neo-Hookean model, has been widely used by some researchers in modeling the cells and biological materials since it can well capture the cell nonlinear large deformation (Breuls et al.

2003b; Ohayon et al. 2005). The Neo-Hookean model is also used as the cell is modeled as a generic one here, and the cell strain energy potential is described as follows:

$$U = C_{10}(\bar{I}_1 - 3) + \frac{1}{D_1}(J-1)^2 \tag{2.6}$$

where U is the strain energy potential, C_{10} is dependent on the shear modulus G_0 as $C_{10} = \frac{G_0}{2}$, D_1 is dependent on the initial bulk modulus K_0 as $D_1 = \frac{2}{K_0}$, $\bar{I}_1$ is the first deviatoric strain invariant, and J is the determinant of the deformation gradient. The Cauchy stress tensor can be determined based on the second Piola-Kirchhoff stress tensor, which can be calculated by taking the partial differentiation of the strain energy potential with respect to the Green-Lagrange strain tensor. The cell pressure is determined based on the mean stress of the Cauchy stress. As the cytoplasmic membrane, cell wall, and internal structure of a cell may play an important role in determining the cell mechanical profile during ejection, future modeling study should also include the effect of cell biological structure.

Since the goal of this study is to study the companying cell mechanical profile during the cell ejection, the cell failure is not of interest here and the predicted mechanical profile values are not compared with the failure threshold values of any cells. Instead, this study is a foundation for future cell damage/failure modeling in laser-assisted cell direct writing.

2.2.3. FEM Approach Validation Using the Rayleigh Approach

The FEM approach for cell ejection modeling is first validated before implementation. In this study, it is validated by comparing its modeling performance with that of the classical Rayleigh bubble dynamics model-based approach in capturing the

cell velocity due to the bubble expansion in an infinite incompressible medium. For this validation study, the hydrogel coating medium of Fig. 2.1 is assumed infinite.

The Rayleigh bubble dynamics model (Plesset et al. 1977) is often used to study the response of surrounding incompressible flow to the expansion of a single spherical bubble. The equation for this gas bubble expansion within a hydrogel medium is described as follows:

$$\ddot{R}R + \frac{3}{2}\dot{R}^2 = \frac{1}{\rho_h}(p_i(t) - p_\infty(t)) - \frac{1}{\rho_h}(\frac{2\sigma}{R} + \frac{4\eta\dot{R}}{R}) \tag{2.7}$$

where R is the current gas bubble radius, $\dot{R}$ is the first order derivative of R, $\ddot{R}$ is the second order derivative of R, t is the time, $p_\infty(t)$ is the pressure in the hydrogel flow at the infinite distance from the gas bubble, $p_i(t)$ is the pressure inside the bubble, and σ is the surface tension. When the pressure inside the bubble is significantly larger than the pressure introduced by the bubble wall surface tension, the surface tension effect is negligible. Then Eq. (2.7) can be further reduced to:

$$\ddot{R}R + \frac{3}{2}\dot{R}^2 = \frac{1}{\rho_h}(p_i(t) - p_\infty(t)) - \frac{4\eta\dot{R}}{\rho_h R} \tag{2.8}$$

where the gas pressure inside the bubble $p_i(t)$ is assumed to obey an isentropic law as follows:

$$p_i(t) = p_0(R_0 / R)^{3\gamma} \tag{2.9}$$

where p_0 is the initial bubble gas pressure, γ (γ = 1.4) is the ratio of the specific heat with respect to the constant pressure and constant volume, and R_0 is the initial bubble radius.

The flow velocity $u(r,t)$ at a distance r from the bubble center can be obtained based on the flow incompressibility:

$$u(r,t) = \frac{R^2}{r^2}\dot{R} \tag{2.10}$$

If the cell deformation is negligible (this simplification is only for this validation case) and the cell volume is also ignored in modeling, the cell center velocity can be approximated as follows:

$$u_{cell} = \frac{R^2}{d^2}\dot{R} \tag{2.11}$$

where u_{cell} is the cell (center) velocity and d is the cell-bubble distance.

The computational flow chart of the Rayleigh approach is shown in Fig. 2.2 and Eq. (2.8) can be solved using the Runge-Kutta routine. The output of interest of the above Rayleigh model-based approach is the cell velocity, which is to be compared with that from the FEM approach.

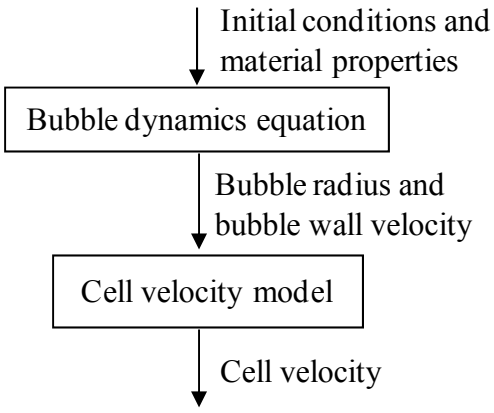

Figure 2.2: Computational flow chart of bubble dynamics equation

To better compare with the results using the Rayleigh model-based approach, the cell deformation should be modeled negligible in the FEM implementation since the Rayleigh model was developed by neglecting the effect of cell deformation. This is

achieved by modeling the cell using a linear elastic material model with an artificially high Young's modulus of 1.79 GPa (10^3 times higher than that commonly adopted (Wang et al. 2008)).

In this validation study the coating medium is assumed incompressible, so a linear polynomial equation of state is selected for the hydrogel coating to make it behave incompressible in this validation study. This equation of state is as follows:

$$P = C_0 + C_1\mu + C_2\mu^2 + C_3\mu^3 + (C_4 + C_5\mu + C_6\mu^2)E \tag{2.14}$$

where the coefficients μ and E are defined similarly as in Eq. (2.4). The incompressible approximation of hydrogel can be achieved by setting C_1 as 150 GPa while others C_i (i = 0, 2, 3, 4, 5, and 6) are zero. The hydrogel cutoff pressure is set as zero in this case.

The other material properties and computational parameters are as follows: the bubble gas specific heats (C_{P-V} and C_{V-V}) are taken as 2.080 J/(g·K) and 1.485 J/(g·K), respectively, the initial hydrogel coating density (ρ_{h0}) is 1000 kg/m^3, and the hydrogel viscosity (η) is 12 ×10^{-3} Pa·s. The cell-bubble distance is 50 μm. The validation case has been performed under an initial bubble gas pressure (P_{b0}) of 221 MPa, which is picked as one order higher than the bubble pressure in a similar laser-assisted surgery process (Gerstman et al. 1996) to simulate the possible effect of vaporization and/or plasma formation. This initial pressure value is equivalent to an initial bubble gas density (ρ_{b0}) of 574.08 kg/m^3 and an initial bubble gas temperature (T_{b0}) of 647 K based on Eq. (2.2). For the implemented FEM computational domain, 186330 solid elements are used for the hydrogel coating medium (500×500×500 μm³), 1380 solid elements for the bubble gas

(R_0 = 24 μm), and 108 solid elements for the cell (6 μm radius). The top surface of the coating is set as the symmetric boundary, and the other surfaces are set as free.

Figure 2.3 shows the modeling results using both the Rayleigh and FEM approaches. It can be seen that the both approaches lead to similar velocity estimations. Since the hydrogel coating is assumed incompressible, the cell instantaneously moves once the gas bubble expands. The reason that the FEM approach underestimates the cell velocity may be attributed to two reasons: 1) the hydrogel cannot be modeled as perfectly incompressible, which leads to more energy dissipation during the bubble expansion in the FEM implementation, and 2) Eq. (2.11) of the Rayleigh approach tends to overestimate the cell velocity since both the cell deformation and volume are ignored. This velocity difference is found to be less pronounced under higher initial bubble pressures. The observed velocity oscillation in using the FEM approach is attributed to the elasticity of cell.

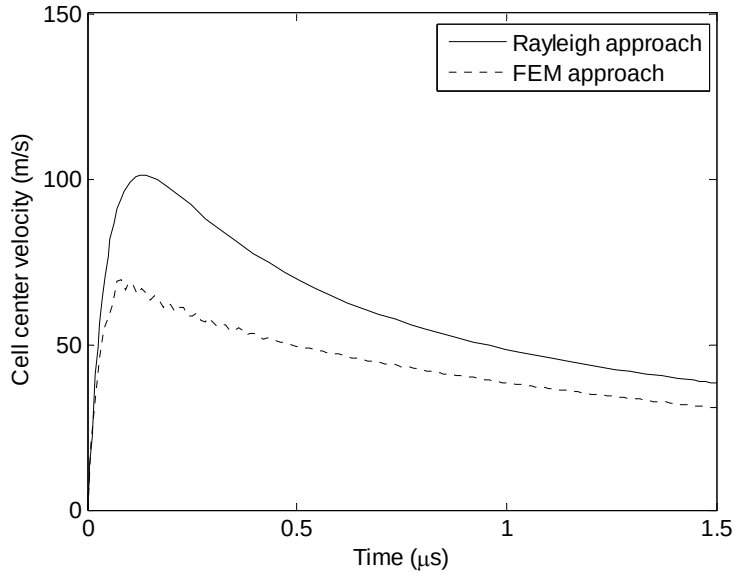

Figure 2.3: Cell center velocity comparison under a 221 MPa initial bubble pressure

Generally speaking, the FEM approach can well capture the bubble expansion-induced cell velocity, and it is expected that the FEM approach should also well capture the cell deformation given proper material models. Compared with the Rayleigh approach, the FEM approach can better model the realistic cell ejection process without unnecessary assumptions on the cell deformation and cell volume as the Rayleigh approach does.

2.3 Numerical Study of Cell Mechanical Profile

2.3.1. Model Implementation

The discussed FEM approach is further implemented to study the cell mechanical profile upon the gas bubble expansion during cell ejection. Since the problem described in Fig. 2.1 is axisymmetric, a quarter of the computational model is analyzed. Figure 2.4 shows a representative quarter symmetric model for this analysis: a quarter cylinder with a radius of 100 μm and a height of 100 μm represents the hydrogel coating, a semi-sphere with a radius of 24 μm denotes the initial bubble gas phase, and a spherical cell with a radius of 6 μm is embedded in the center line of cylinder and 55 μm (cell-bubble distance) away from the center of bubble. The air domain is partially shown in Fig. 2.4. Larger coating domains have also been implemented; however, there is negligible difference in terms of simulation results. A total of 50318 solid elements are used in which 108 elements for the cell, 11330 elements for the coating, 37500 elements for the air, and 1380 elements for the bubble gas. Element 1, the closest to the expanding bubble, represents the top surface region, Element 2 the middle region, and Element 3 the bottom surface region.

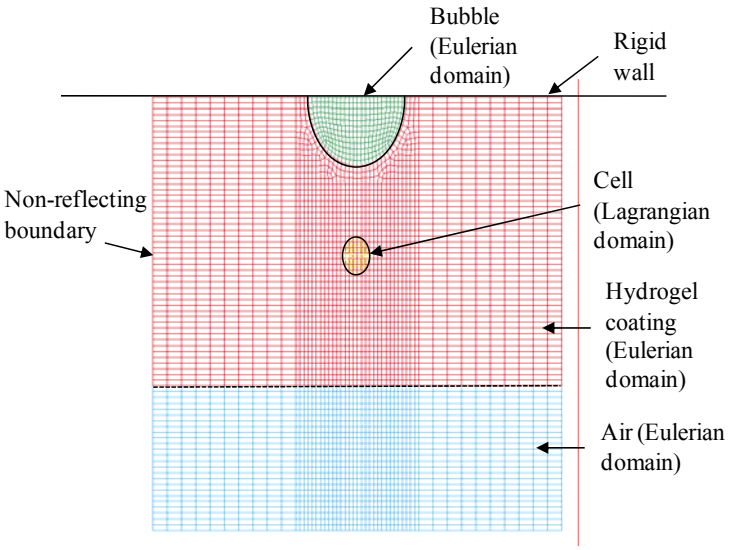

(a)

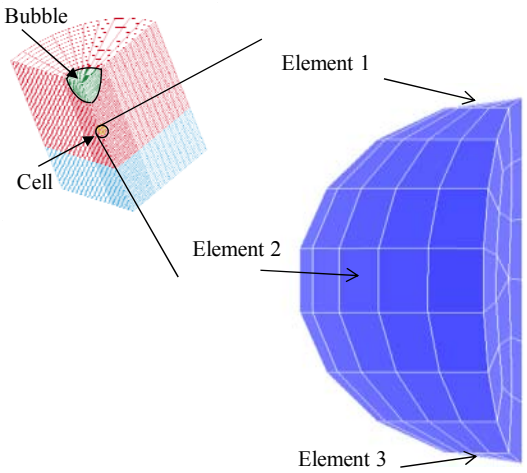

(b)

Figure 2.4: (a) Coupled Lagrangian and Eulerian computational domains and (b) distribution of cell elements

A rigid wall boundary condition is used to model the rigid quartz support. To reduce the effect of reflection of the stress waves at the outer surface of the hydrogel and

air domains, a non-reflecting boundary condition is applied for the faces associated with these domains. The non-reflecting boundary condition enables the propagation of pressure waves across the boundaries mimicking an infinitely large coating domain.

The aforementioned material models are applied here. If not specially specified, the same material properties and computational parameters used in the previous validation section are used here too. The hydrogel cutoff pressure is set as 25 kPa (Drury et al. 2004; Wang et al. 2008). The cell shear modulus is set as 15.6 kPa (Breuls et al. 2003b), the Poisson's ratio 0.475 and the density 1000 kg/m^3, which are used to estimate C_{10} and D_1. The initial air mass density (ρ_{a0}) is specified as 1.28 kg/m^3, and the initial bubble gas pressure as 221 MPa.

2.3.2. Mechanical Profile of Cell

In order to appreciate the cell mechanical profile such as the cell center velocity, cell center acceleration, and pressure changes during the bubble expansion-induced ejection, some representative simulation results are presented in the following based on the condition of a 221 MPa initial bubble pressure and a 55 μm cell-bubble distance. Such cell mechanical information will help better understand and model cell damage during laser-assisted cell direct writing.

2.3.2.1 Evolution of Cell Center Velocity and Acceleration

The ejection velocity of cell droplet is of importance in determining the cell viability during the subsequent cell droplet landing process as studied in (Wang et al. 2008). The ejection velocity is the initial velocity at which the cell droplet impacts the receiving substrate. For some applications, the cell droplet ejection velocity should be well controlled to minimize the possible cell damage during landing. Figure 2.5 shows

the cell center velocity evolution during the ejection process. It can be seen that the cell velocity oscillates initially and then smoothes out gradually with a constant ejection velocity (107 m/s in this simulation), and this velocity oscillation is attributed the elasticity of cell, implying a negative acceleration. Due to the compressibility of hydrogel, there is a delay in the velocity response to the bubble expansion as seen from Fig. 2.5. After around 2 μs, the cell droplet has a very weak connection with the coating and starts to leave the hydrogel coating with a constant velocity.

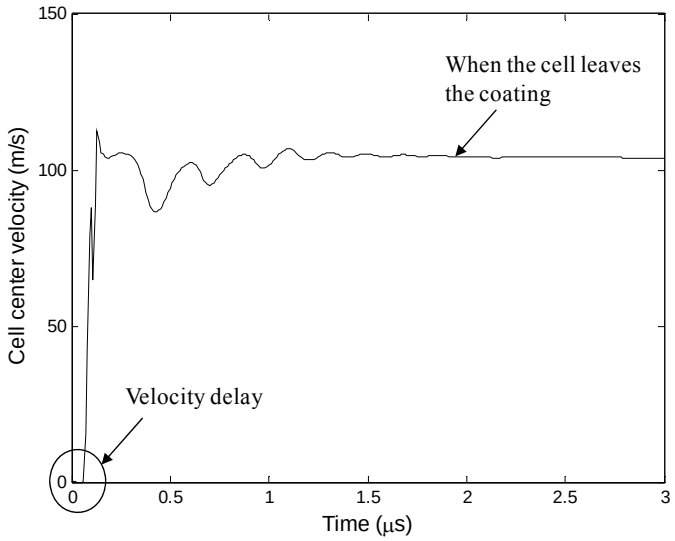

Figure 2.5: Evolution of cell center velocity

Figure 2.6 shows the simulation result of cell acceleration. As seen from Fig. 2.6, the cell first accelerates as high as 10^9 m/s^2 at the beginning period of bubble expansion and then quickly approaches zero in an oscillation manner. The high acceleration period only lasts a very short period (about 0.1 μs), and the very short duration is critical to

guarantee the cell survival. The absolute magnitude of acceleration depends on the material properties of the hydrogel and cell as well as the initial bubble gas pressure.

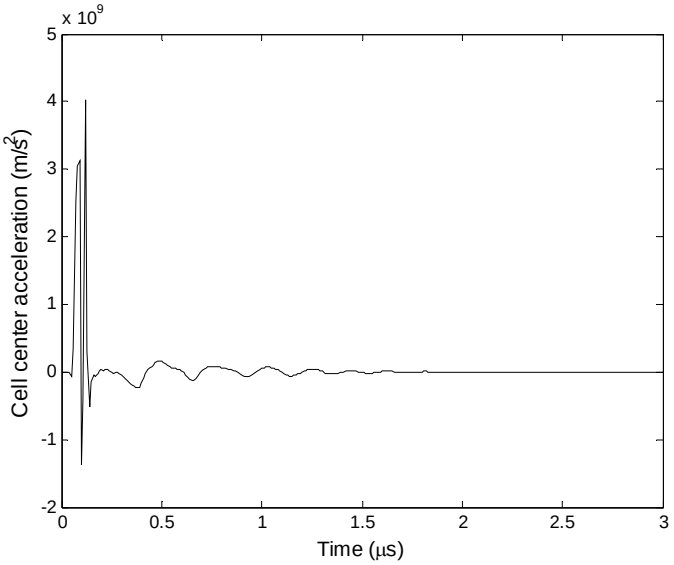

Figure 2.6: Evolution of cell center acceleration

2.3.2.2 Evolution of Pressure

The transferred cells are easily damaged during cell manipulation especially when being subject to the high pressure induced by the stress waves (Lee et al. 1999). The stress waves may make the cell membrane permeable, and the molecules in the extracellular medium diffuse into the cytoplasm under the concentration gradient. Subsequently, the plasma membrane reseals to keep the exogenous molecules inside the cell, which may lead to functional cell injury. On the other hand, the stress may induce the cell membrane or other cell components structurally broken, which also can cause cell damage. For this ejection process, the cell pressure due to the bubble expansion should be carefully understood.

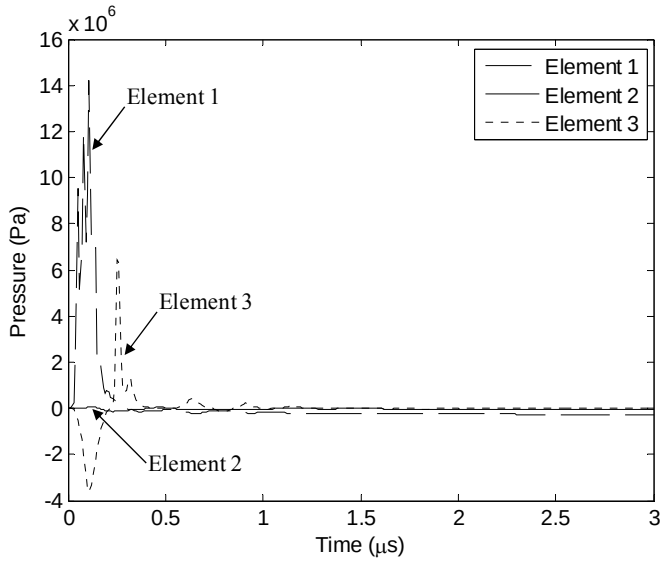

Figure 2.7: Cell pressure at different cell internal regions

Figure 2.7 shows the simulation result of cell pressure at different cell internal regions. Generally speaking, the pressure can be as high as 10 MPa at the beginning period of bubble expansion and quickly decreases to zero in an oscillation manner as seen from the cell acceleration evolution in Fig. 2.6. At a specified moment, the top surface region (Element 1 of Fig. 2.4(b)), which is close to the expanding bubble, experiences the highest pressure level, followed by the bottom surface region (Element 3) and the middle region (Element 2).

2.3.3 Parametric Study

For the cell damage control during cell direct writing, the effect of typical controllable process conditions such as the coating viscosity, cell-bubble distance, and initial bubble pressure needs to be carefully studied to minimize the possible cell damage while maintaining process efficiency. Since the top surface region of cell (Element 1) usually experiences a relatively severe pressure condition as discussed before, Element 1

is selected as the representative cell region to study the effect of the coating viscosity, cell-bubble distance, and initial bubble pressure on the cell pressure. For this parametric study, only the initial bubble gas density (ρ_{b0}) is changed to 57.408 kg/m^3, which is determined based on a 22.1 MPa initial bubble pressure. For the sake of simulation efficiency, the 22.1 MPa pressure is selected based on the critical pressure of water as in a previous study (Gerstman et al. 1996).

2.3.3.1 Effect of Coating Viscosity

Figure 2.8 shows the effect of coating viscosity on the cell center velocity, cell center acceleration and pressure under the initial pressure of 22.1 MPa and the cell-bubble distance of 55 μm. Three different viscosity values (1.2, 12, and 120×10^{-3} Pa·s) have been studied, and these values are also close to the viscosity of various glycerol solutions, which are gaining widely applications in biological printing (Lin et al. 2009b). It is shown that there is a small difference between the results using the viscosities of 1.2×10^{-3} Pa·s and 12×10^{-3} Pa·s; however, the simulation using the viscosity of 120×10^{-3} Pa·s leads to higher velocity, acceleration and pressure at the beginning of the process but a lower ejection velocity at the moment of ejection. When the viscosity is 120×10^{-3} Pa·s, there is an observable increment of velocity at the initial stage due to a pronounced viscous friction effect; however, the ejection velocity is the lowest because of the excessive viscous energy dissipation during the ejection process. It should be noted that the viscosity within the cell-extracellular medium boundary layer should also be considered in the future study even under a larger Reynolds number condition since this effect introduces a viscous force to the cell.

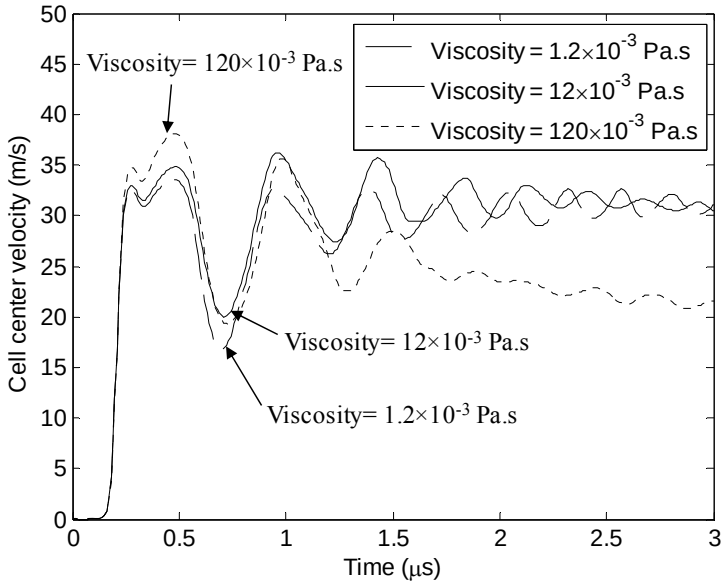
Viscosity = 1.2×10-3 Pa.s
Viscosity = 12×10-3 Pa.s
Viscosity = 120×10-3 Pa.s
Viscosity= 120×10-3 Pa.s
Viscosity= 12×10-3 Pa.s
Viscosity= 1.2×10-3 Pa.s
Cell center velocity (m/s)
Time (μs)

(a)

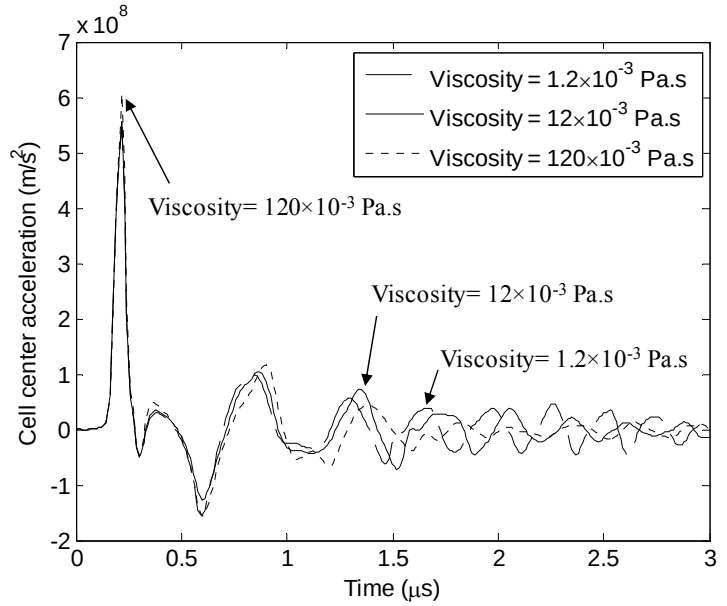
x 10^8
Viscosity = 1.2×10-3 Pa.s
Viscosity = 12×10-3 Pa.s
Viscosity = 120×10-3 Pa.s
Viscosity= 120×10-3 Pa.s
Viscosity= 12×10-3 Pa.s
Viscosity= 1.2×10-3 Pa.s
Cell center acceleration (m/s2)
Time (μs)

(b)

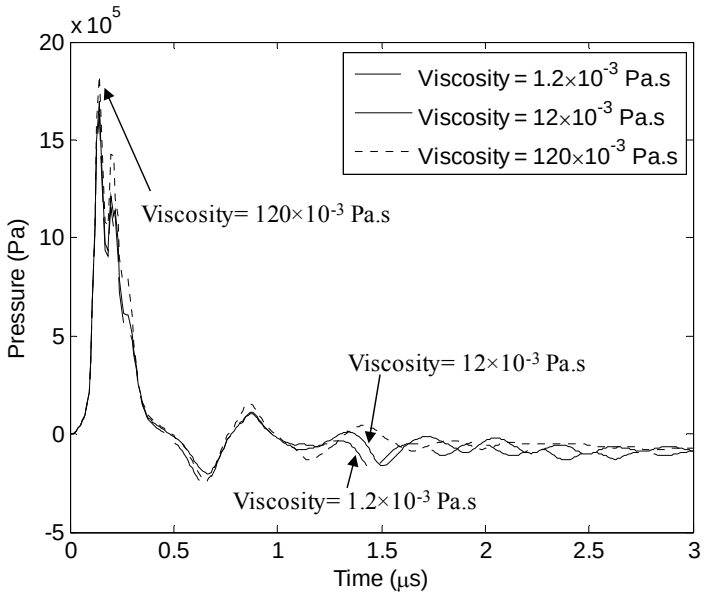

(c)

Figure 2.8: (a) Cell center velocity (b) cell center acceleration and (c) cell pressure under different coating viscosity conditions (the initial pressure is 22.1 MPa and the cell-bubble distance is 55 μm)

2.3.3.2 Effect of Cell-Bubble Distance

The cell response depends on not only the coating material properties but also the operating conditions such as the cell-bubble distance and initial bubble pressure. To study this cell-bubble distance effect, Figure 2.9 shows the effect of bubble distance on the cell center velocity, acceleration and pressure under the initial pressure of 22.1 MPa and the coating viscosity of 12×10^{-3} Pa·s. It is observed that the velocity, acceleration and pressure magnitude decreases when the distance increases. Also, it is found that the profiles shift right a little bit when the cell-bubble distance increases, which indicates that it takes more time for the stress wave to reach the far away cell. It is generally expected

that for the coating embedded with multiple cells, the cells close to the bubble are more susceptible to mechanical damage.

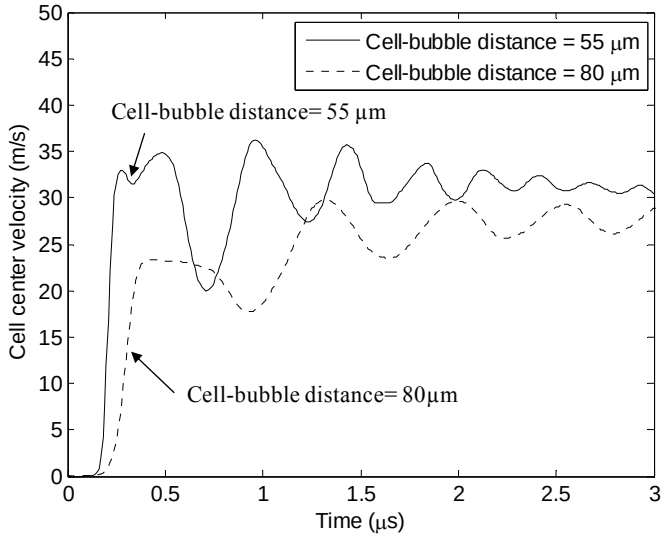

(a)

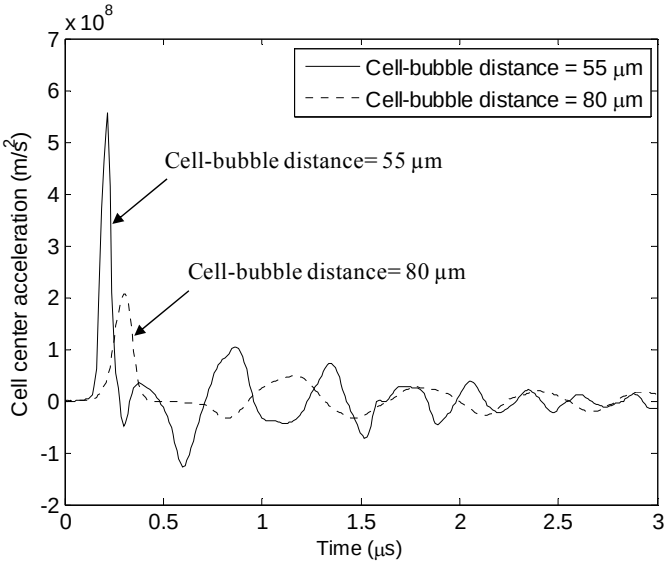

(b)

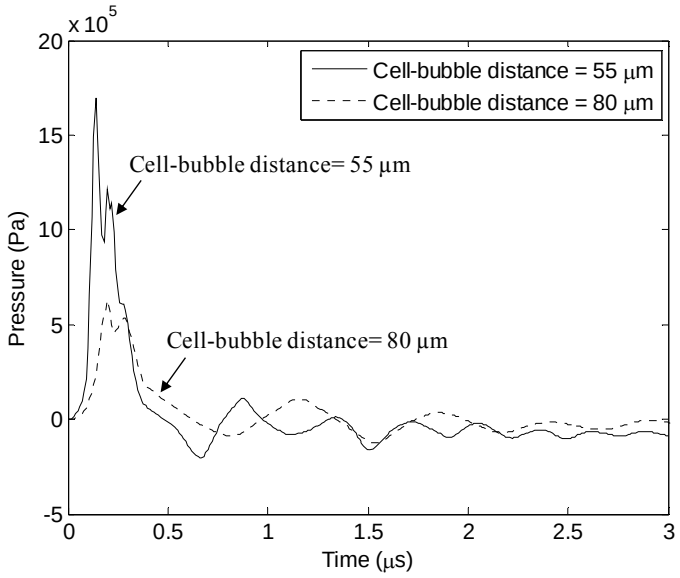

(c)

Figure 2.9: (a) Cell center velocity (b) cell center acceleration and (c) cell pressure under different cell-bubble distances (the initial pressure is 22.1 MPa and the coating viscosity is 12×10^{-3} Pa·s)

2.3.3.3 Effect of Initial Bubble Pressure

The initial bubble pressure also plays an important role in cell ejection, and the magnitude of initial pressure can be controlled by the laser fluence, laser pulse, and energy absorption property of coating material. Generally, when the laser energy is high enough to cause the coating material to vaporize and even ionize, the cell ejection is easily caused by the bubble expansion mechanism rather than the thermoelastic stress wave. Thus, the study of how the cell responds to the initial bubble pressure is critical to mitigate the cell damage in direct writing.

Figure 2.10 shows the effect of initial bubble pressure on the cell center velocity, acceleration and pressure under the coating viscosity of 12×10^{-3} Pa·s and the cell-bubble distance of 55 μm. It is shown that the larger initial pressure induces a larger cell velocity, acceleration and pressure as expected. As a result, the cell viability is adversely affected by large initial bubble pressures.

It should be noted that when the initial gas bubble pressure increases, the flow velocity magnitude increases accordingly. Thus, the inertial effect becomes dominant over the viscosity effect, and the coating material behaves more like a non-viscous flow. If it is the case, the bubble expansion-induced material motion is a non-viscous flow except within the boundary layer around the cells.

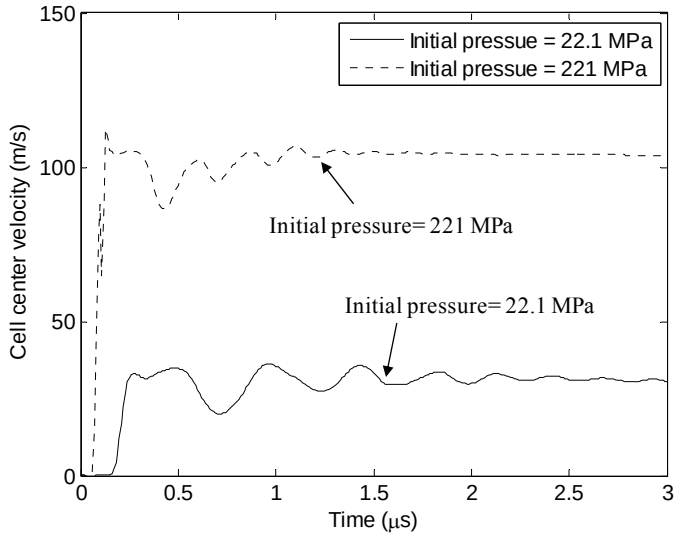

(a)

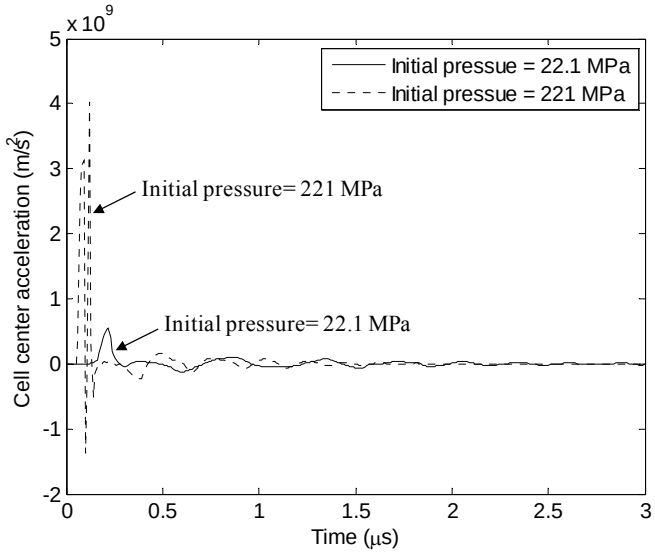

(b)

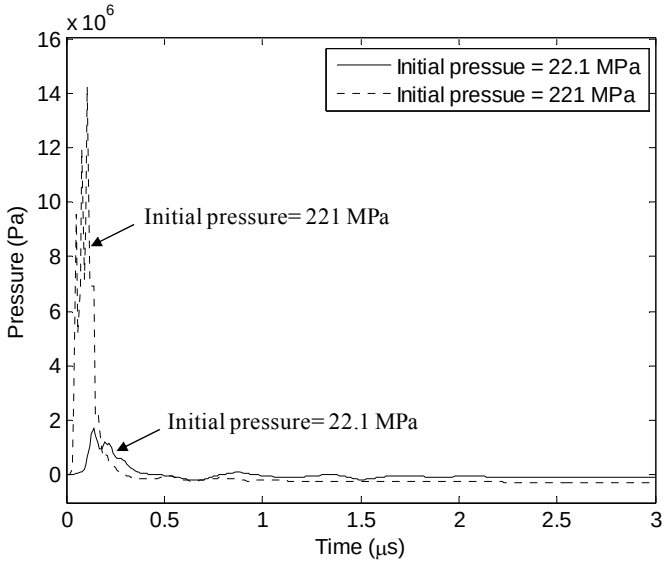

(c)

Figure 2.10: (a) Cell center velocity (b) cell center acceleration and (c) cell pressure under different initial bubble pressures (the coating viscosity is 12×10^{-3} Pa·s and the cell-bubble distance is 55 μm)

2.4 Discussion

The velocity, acceleration and pressure profile, which cells experience during the ejection process in laser-assisted direct writing, has been investigated in this study. While the initial bubble formation process is not of particular interest here, the following bubble expansion-induced cell mechanical profile is studied. This modeling study firstly enables a quantitative understanding of the cell mechanical profile during the ejection process and offers some insight into the process-induced cell damage.

The transferred cells after direct writing are sometimes damaged and may not be viable mainly due to the pressure/stress loading studied. The effect of laser-induced pressure/stress wave on cell/tissue damage has been of interest in the laser-tissue interaction research community. It is generally recognized (Lee et al. 1999) that the laser-generated stress wave during the laser-tissue interaction may make a cell membrane permeable. As a result, molecules present in the extracellular medium may diffuse into the cytoplasm under the concentration gradient. Subsequently, the plasma membrane reseals, keeping the exogenous molecules inside the cell, which may lead to the functional cell injury (Lee et al. 1999). The mechanisms of membrane permeabilization due to the laser-generated stress wave have been studied (McAuliffe et al. 1997; Lee et al. 1997), but are still not elucidated yet. Furthermore, a strong stress wave may directly induce the cell membrane or other components structurally broken. The stress-induced cell damage mechanism is similar for both the laser-assisted direct writing process and the laser-tissue direct interaction. It should be pointed out that there may be some additional photomechanical effect-induced thermoelastic stress waves present in laser-assisted direct writing although they are negligible when using high energy laser pulses.

The cell damage degree due to the pressure or stress depends on many different factors such as stress magnitude and/or stress duration (Lee et al. 1999; Wang et al. 2008). Exposure of cells to high pressures may induce a high degree of membrane permeabilization and substantial damage of intercellular components which may prevent cells from recovering from permanent injury after the removal of pressure or stress loading. It is observed in this study that the cell can first accelerate as high as 10^9 m/s^2 at the beginning period of bubble expansion and then quickly approaches zero in an oscillation manner. The acceleration rate is extremely high for a cell to survive. Fortunately, this high acceleration only lasts a very short period (about 0.1 μs), and this duration might be too short for a cell to fully respond to a very high acceleration since the cell itself is a viscoelastic material (Kasza et al. 2007). As a result, cells can still survive under a high acceleration rate if the combined effect of stress magnitude and duration is tolerable by the cell (Ringeisen et al. 2004; Wang et al. 2008). It was studied that the cell damage depends on not only the process-induced stress magnitudes but also the stress duration (Wang et al. 2008). This combined stress magnitude and duration effect on cell damage should be further modeled for cell viability control in cell direct writing.

The cell velocity information after ejection is also studied here since the impact-induced damage during landing also poses a significant challenge to achieve a high cell viability post-cell transfer (Ringeisen et al. 2004; Wang et al. 2008). A higher ejection velocity of the formed cell droplet usually leads to a lower post-transfer cell viability (Wang et al. 2008). This modeling study is expected to help optimize the cell direct writing process by better estimating the landing velocity for given operating direct writing conditions.

2.5 Conclusions

The bubble expansion-induced cell ejection in laser-assisted cell direct writing has been carefully studied using the FEM approach in this study. Using the validated FEM approach, the evolution of cell center velocity, cell center acceleration, and pressure is studied, and the effects of coating viscosity, cell-bubble distance, and initial bubble pressure on the cell mechanical profile are further investigated during cell ejection. The main computational predictions can be drawn as follows:

1. The cell velocity oscillates initially and then smoothes out gradually with a constant ejection velocity. The cell can first accelerate as high as 10^9 m/s^2 at the beginning period of bubble expansion and then quickly approaches zero in an oscillation manner; fortunately, this high acceleration period only lasts a very short period (about 0.1 μs).
2. The cell pressure can be very high at the beginning period of bubble expansion and quickly decreases to zero in an oscillation manner as seen from the cell acceleration evolution. The cell top surface region usually experiences the highest pressure level, followed by the bottom surface and the middle regions
3. A high viscosity can lead to an observable velocity increment at the initial stage due to the pronounced viscous friction effect, but the ejection velocity decreases because of the excessive viscous energy dissipation.
4. The pressure magnitude decreases when the cell-bubble distance is large. It is generally expected that for the coating embedded with multiple cells, the cells close to the bubble are more susceptible to mechanical damage.

5. A larger initial pressure induces a larger cell pressure as expected. As a result, the cell viability is adversely affected by large initial pressures.

As discussed before, while the MAPLE DW schematic is used in Figure 2.1 for illustration, the proposed modeling approach is applicable to BioLP by assuming the energy conversion thickness negligible as well as other jet-based cell direct-write processes.

CHAPTER 3

MODELING OF THERMOELASTIC STRESS WAVE IN LASER-ASSISTED CELL WRITING

3.1 Introduction

The possible stress field and cell injury during the droplet ejection process may come from two different sources: the bubble expansion-induced stress wave and the thermoelastic stress wave. In Chapter 2, the bubble expansion-induced cell mechanical profile was studied. Generally speaking, the pressure generated by the phase explosion-induced bubble expansion is usually one order of magnitude higher than that due to thermoelastic effect (Sigrist et al. 1978; Park et al. 1996), and the effect of thermoelastic stress wave is usually neglected in predicting the droplet formation and ejection-induced mechanical profile during the process (Wang et al. 2009a). However, the thermoelastic stress wave may introduce an alternative impact to cells to be transferred in laser-assisted cell direct writing even if the incident laser pulse energy is not high enough to induce the vaporization or optical breakdown of coating materials. Under this circumstance, it is of interest to study the thermoelastic stress wave inside the coating.

The objective of this chapter is to model the thermoelastic stress wave propagation inside the coating in laser-assisted cell direct writing when the vaporization or optical breakdown of coating materials is not available. It is also assumed that the resulting thermoelastic stress does not induce any cavitation bubble formation.

This chapter is organized as follows. First, the laser irradiation-induced thermoelastic stress is discussed as the background information. Second, modeling of the

thermoelastic stress is introduced and its computational implementation using a finite difference method is explained. Then the finite difference method is validated with a documented study and further applied to study thermoelastic pressures in laser-assisted direct writing. Finally, main conclusions are drawn and future work is discussed. This study will help to understand the photomechanical stress and the thermoelastic stress-induced cell injury in cell direct writing.

3.2 Problem Formulation and Computational Implementation

3.3.1 Problem Formulation

A representative thermoelastic stress wave propagation schematic in laser-assisted cell direct writing is illustrated in Fig. 3.1 under a large laser spot size input (a one-dimensional (1D) computation case for a two-dimensional (2D) pressure wave propagation process). A compressive plane wave is developed and propagates towards the free surface. At the free surface the incoming compressive wave is reflected as a tensile wave back into the medium. Close to the surface region the superposition of pressure leads to cancellation of the pressure. In Fig. 3.1, the tensile pressure results from the free surface reflection. It should be pointed out if the laser spot size is comparable or smaller than the laser optical penetration depth, there will be a tensile stress wave immediately following the compressive stress wave and this tensile wave is emitted from the edge of laser spot. Under such a circumstance, while the wave generation is three dimensional (3D), it is a 2D computation case due to its symmetrical property.

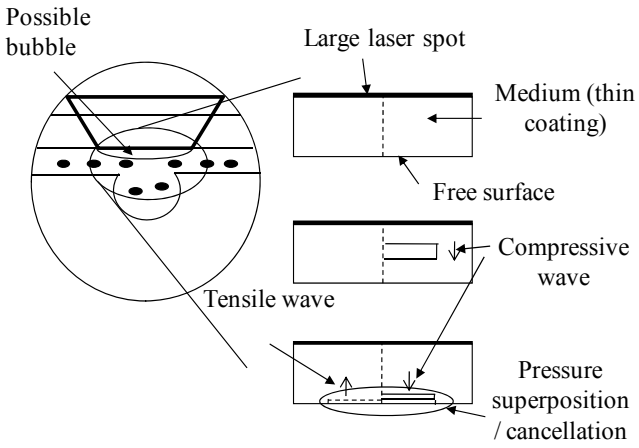

Figure 3.1: Schematic of the stress propagation in a 1D computation scenario

As discussed, transient thermoelastic stress-induced material damage can be induced by laser irradiation under certain confinement conditions (Anderson et al. 1983; Paltauf et al. 1998; Georgiou et al. 2003). As in laser ablation, the heated volume in laser-assisted direct writing is typically defined by the optical penetration depth, and the characteristic time is thus given from the thermal diffusion equation as (Paltauf et al. 1998):

$$t_{th} = \frac{d^2}{4\kappa} \tag{3.1}$$

where κ is the thermal diffusivity and d the smallest dimension of the heated volume, typically the optical penetration depth. By introducing a dimensionless quantity as a measure of laser pulse duration t_p relative to the characteristic thermal diffusion time $t_d^* = 4t_p\kappa / d^2$, the thermal confinement condition can be expressed as $t_d^* \le 1$ (Vogel et al. 2003).

Another important time scale is the relaxation time of stress t_{ac} given by (Paltauf et al. 1998):

$$t_{ac} = \frac{d}{c} \tag{3.2}$$

where c is the speed of sound in the medium. If the laser pulse is shorter than t_{ac}, the stress confinement condition is satisfied.

As the thermoelastic stress wave is generated, it can be modeled using the equation of motion by assuming no viscous damping. The stress wave equation inside an aqueous medium as in this study is given in terms of velocity potential ϕ as follows (Gusev et al. 1993):

$$\nabla^2(\phi) - \frac{1}{c^2}\frac{\partial^2 \phi}{\partial t^2} = \frac{\beta}{\rho C_p} S \tag{3.3}$$

where β is the thermal volumetric expansion coefficient of the medium, t the time, ρ the mass density, C_p the specific heat capacity, and S the heat generated per unit time and volume. In this study, S is the absorbed energy of each laser pulse. The relationships among the pressure p, particle velocity v, and velocity potential ϕ are as follows, respectively,

$$v = \nabla \phi \tag{3.4}$$

$$p = -\rho(\partial \phi / \partial t) \tag{3.5}$$

The laser beam is usually assumed a circularly symmetric shape with a finite radius. Compared with the radius of the laser beam, the thermal penetration thickness is very small, e.g., the thickness of coating is around 1μm for aqueous biolayers (Vogel et

al. 2003). Thus, the laser energy absorption-induced heated zone has a disk shape. During the laser pulse duration, partial laser energy is absorbed by the biological materials and converted into thermal energy, which raises the temperature and further induces the prominent thermoelastic stress if the confinement conditions are satisfied.

For the instantaneous heat deposition case, the heat source term S can be expressed as follows:

$$S(r,z,t) = W(r,z)\delta(t) \tag{3.6}$$

where $W(r)$ is the absorbed volumetric energy density and $\delta(t)$ the Dirac delta function. For the case of the finite pulse duration with a Gaussian pulse, the heat source can be represented alternatively as follows (Noack et al. 1999):

$$S(r,z,t) = W(r,z)\exp\left(-4\log(2)\left(\frac{t}{t_p}\right)^2\right) \tag{3.7}$$

The energy density in a pure absorber can be written as:

$$W(r,z) = \mu_a H_0 f(r)\exp(-\mu_a z) \tag{3.8}$$

where H_0 is the incident laser fluence/radiant exposure at the surface of the absorbing material, μ_a is the absorption coefficient, and $f(r)$ is a dimensionless function describing the radial laser beam profile (Paltauf et al. 1998). For a perfect top-hat laser beam, $f(r)$ can be described as follows:

$$f(r) = 1, \quad r \le a \tag{3.9}$$

$$f(r) = 0, \quad r > a \tag{3.10}$$

For a trapezoidal profile laser, $f(r)$ is as follows:

$$f(r) = 1, \quad r \le a \tag{3.11}$$

$$f(r) = \exp(-(r-a)^2 / d^2), \qquad r > a \tag{3.12}$$

where a is the radius of the laser spot and d characterizes the falling slope of the beam profile.

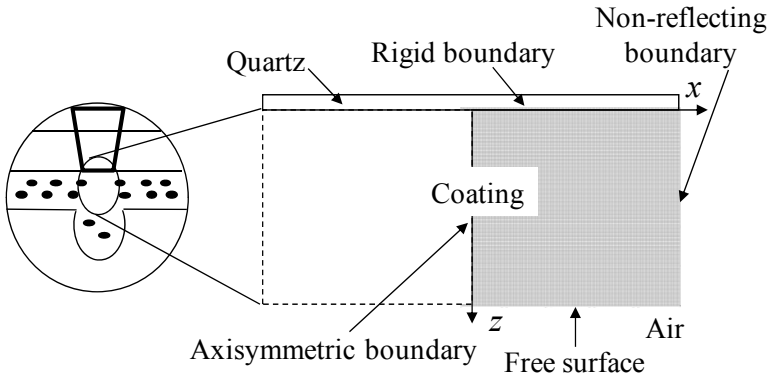

Figure 3.2: Schematic of the computational domain

As seen from Fig. 3.2, the boundary conditions in this study are as follows:

$$\frac{\partial \phi}{\partial r} = 0 \quad \text{at} \quad z = L \quad \text{(Free surface)} \tag{3.13}$$

$$\phi = 0 \quad \text{at} \quad z = 0 \quad \text{(Rigid boundary)} \tag{3.14}$$

$$\frac{\partial \phi}{\partial r} = 0 \quad \text{at} \quad r = 0 \quad \text{(Axisymmetric boundary)} \tag{3.15}$$

$$\frac{\partial \phi}{\partial r} + \frac{1}{c}\frac{\partial \phi}{\partial t} = 0 \quad \text{at} \quad r = w \quad \text{(Non-reflecting boundary)} \tag{3.16}$$

where L is the thickness of the coating, and w is the radial dimensional size of the computational domain.

Instantaneous heating causes a distribution of photoacoustic pressure at the initial state, and this initial condition is defined as follows (Vogel et al. 2003):

$$p_0 = A\Gamma W(r,z) \tag{3.17}$$

where Γ is the Grüneisen coefficient and A is the factor considering the finite laser pulses. The whole modeling procedure is illustrated in Fig. 3.3.

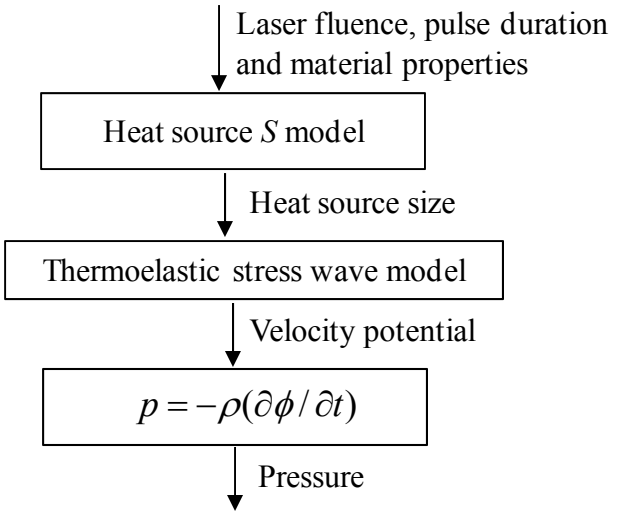

Figure 3.3: Schematic of the computational domain

3.2.2 Computational Implementation

As shown in Fig. 3.2, the computational domain to simulate the thermoelastic stress generation is treated as two dimensional (2D) in computational modeling for this laser pulse-centered axisymmetric scenario in laser-assisted direct writing. The stress wave governing equation in the 2D axisymmetric coordinates can be written as follows:

$$\frac{1}{r}\frac{\partial\phi}{\partial r} + \frac{\partial^2\phi}{\partial r^2} + \frac{\partial^2\phi}{\partial z^2} - \frac{1}{c^2}\frac{\partial^2\phi}{\partial t^2} = \frac{\beta}{\rho C_p}S \tag{3.18}$$

where r is the radial coordinate and z is the axial coordinate.

The second order central difference scheme is used to approximate the spatial derivatives, and the backward difference scheme is used for the time derivative of Eq. (3.18). The approximations are given by:

$$\frac{\partial \phi}{\partial r} = \frac{\phi_{i+1,j}^{k+1} - \phi_{i-1,j}^{k+1}}{2h_r} \tag{3.19}$$

$$\frac{\partial^2 \phi}{\partial r^2} = \frac{\phi_{i+1,j}^{k+1} - 2\phi_{i,j}^{k+1} + \phi_{i-1,j}^{k+1}}{h_r^2} \tag{3.20}$$

$$\frac{\partial^2 \phi}{\partial z^2} = \frac{\phi_{i,j+1}^{k+1} - 2\phi_{i,j}^{k+1} + \phi_{i,j-1}^{k+1}}{h_z^2} \tag{3.21}$$

$$\frac{\partial \phi}{\partial t} = \frac{\phi_{i,j}^{k+1} - \phi_{i,j}^{k}}{\Delta t} \tag{3.22}$$

$$\frac{\partial^2 \phi}{\partial t^2} = \frac{\phi_{i,j}^{k+1} - 2\phi_{i,j}^{k} + \phi_{i,j}^{k-1}}{\Delta t^2} \tag{3.23}$$

where i and j stand for the node number in the mesh grids, k-1 represents the current time step, k represents the immediate time step, k+1 represents the future time step, h_r and h_z represent the mesh size in the radial and axial directions, respectively, and Δt is the time step size.

It is seen from Eq. (3.23) that the current and immediate time steps are needed to advance the computation at the future time step. Based on Eq. (3.5) the initial pressure can be written as the time derivative of velocity potential ϕ as follows:

$$p_{i,j}^{1} = -\rho \frac{\phi_{i,j}^{2} - \phi_{i,j}^{1}}{\Delta t} \tag{3.24}$$

$$\phi_{i,j}^{1} = 0 \tag{3.25}$$

and $\phi_{i,j}^2$ can be calculated as follows using Eq. (3.24):

$$\phi_{i,j}^2 = -\frac{1}{\rho}(p_{i,j}^1 \Delta t) \tag{3.26}$$

The Crank-Nicolson method, which has a second-order time accuracy, has been used to solve the 2D stress wave governing equation (Eq. (3.18)) using the boundary and initial conditions as stated in Eqs. (3.13-3.17). As the Crank-Nicolson method is sensitive to the time step, here the time step was selected based on sensitive studies to guarantee computational convergence.

3.2.3 Numerical Validation

Before studying the thermoelastic stress generation in cell direct writing, the proposed computational procedure is first validated with the documented results in modeling the pressure profile near a water-glass interface under laser radiation (Paltauf et al. 1998). Figure 3.4 illustrates the modeling domain for this experimental setup.

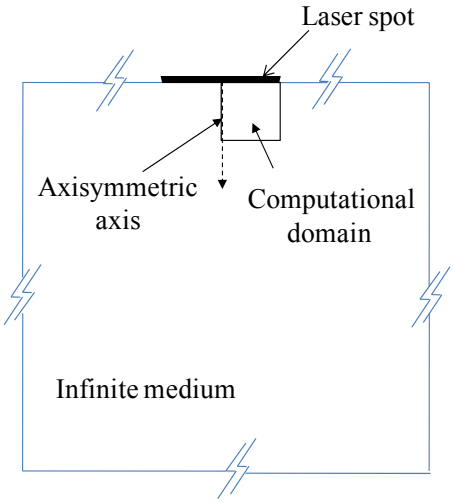

Figure 3.4: Modeling domain schematic for an infinite medium

For this experimental setup (Paltauf et al. 1998), the medium was considered infinite, and the beam profile was described by Eqs. (3.9) and (3.10). For a Dirac delta laser pulse, the pressure profile p_δ for any location along the axisymmetric axis can be analytically determined, and this analytical approach has been successfully validated with experimental measurements (Paltauf et al. 1998). For a laser pulse with a finite pulse duration, the pressure can be estimated as a convolution of the delta-pulse solution with the temporal profile of laser pulse (Paltauf et al. 1998).

The proposed numerical approach has been implemented to simulate the pressure profile with this infinite medium. The laser spot had a radius of 200 μm and its optical penetration depth was determined as $1/\mu_a$, where μ_a is the laser energy absorbing coefficient of the medium. The computational domain was 200 μm×200 μm as part of an infinite domain as shown in Figure 3.5 to save computational time. The laser output Dirac delta laser pulses, and the other related material properties are listed as follows: c = 1500 m/s (Paltauf et al. 1998), the absorbing coefficient μ_a = 840/cm (Paltauf et al. 1998), Γ = 0.11 (Paltauf et al. 2003), the medium density ρ = 1,000 kg/m^3 (Paltauf et al. 1998), $\beta = 2.07\times10^{-4}$/K, C_p = 4190 J/kg·K, and the laser fluence was taken as 5.25×10^4 J/m^2 (Paltauf et al. 1998). The grid size used was 0.5 μm and the time step size 0.01 ns. The time step size here and in the following sections was selected based on a sensitivity study to guarantee convergence.

Figure 3.5 shows the comparison among the numerical and analytical solutions of the pressure history at a fixed location located at 100 μm below the laser spot center along the axisymmetric axis laser. A good agreement in modeling accuracy is observed

among them; however, the validated analytical approach (Paltauf et al. 1998) cannot be extended to modeling the wave propagation inside a finite thin coating domain as experienced in cell direct writing, so the proposed numerical approach is further used to model the thermoelastic stress generation process.

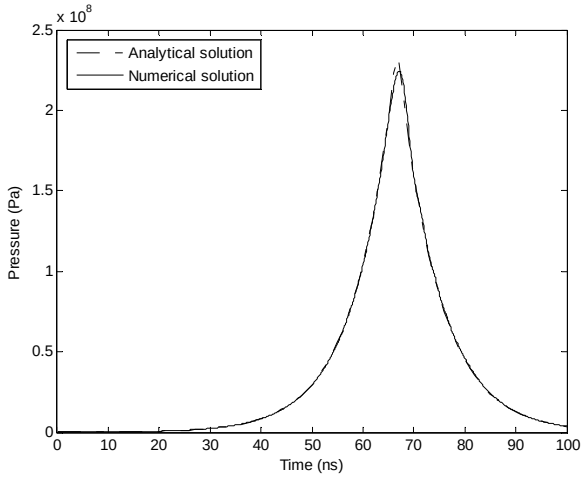

Figure 3.5: Numerical and analytical solutions of the pressure history at a fix location 100 μm below the laser spot center along the axisymmetric axis (Delta pulse with a = 200 μm)

3.3 Results and Discussion

As shown in Fig. 3.2, a Gaussian laser pulse (as defined in Eq. (3.7)) with a trapezoidal profile (a = 22 μm and d = 2 μm) was used in this study. The laser fluence was taken as 50 mJ/cm^2 and had a spot radius of 24 μm and a pulse duration of 0.1 ns. The coating had a thickness of 100 μm as in most laser-assisted direct writing processes, and the axisymmetric computational domain was taken as 100 × 100 μm. For modeling of cell direct writing, the coating was modeled as a pure water layer without any other biomaterials inside for simplicity. The point of interest was 50 μm under the laser spot

along the axisymmetric axis. The related material properties are listed as follows: the speed of sound in water c = 1500 m/s (Paltauf et al. 1998), μ_a = 10^4/cm (Vogel et al. 2003), Γ = 0.11 (Paltauf et al. 2003), A = 0.80 for the 0.1 ns laser pulse (Paltauf et al. 2003), the medium density ρ = 1000 kg/m^3 (Paltauf et al. 1998), β = 2.07×10^{-4}/K, and C_p = 4190 J/kg·K. The grid size used was 0.25 μm and the time step size 0.005 ns. If not specified, the above conditions and parameters were used as default.

3.3.1 Representative Pressure Profile

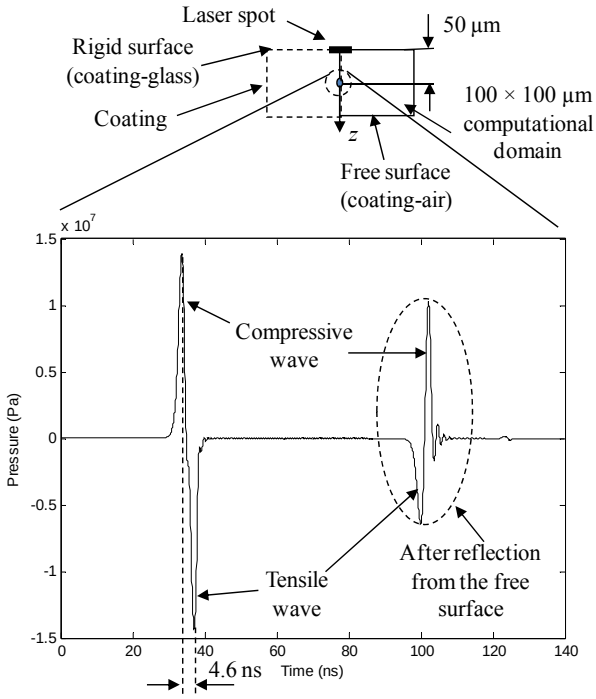

Figure 3.6: A representative pressure profile below the laser spot center (z = 50 μm)

For a finite thickness coating, the pressure wave reflection at the coating-air and the coating-glass interfaces has to be considered. Pressure reflection occurs at the coating-air and the coating-glass interface due to their acoustic impedances. The interface

reflectivity is equal to -1 for a free surface and 1 for a rigid surface. Thus the reflected stress at the rigid transparent support does not change the stress sign due to the very high acoustic impedance in the rigid support while it changes its sign when reflected at the free surface. The stress wave may be canceled by the reflected opposite stress wave near the vicinity of the coating-air free interface due to the reflected wave with a different sign.

Figure 3.6 shows the pressure profile of a fixed location located at 50 μm below the laser spot center, and only the first 140 ns information is presented. It is found that a bipolar pressure pulse was developed and such a bipolar pulse was also observed in studying the acoustic wave field generated in front of a submerged fiber tip (Paltauf et al. 1998). At about 33 ns after laser radiation in this study, a positive compressive pressure arrived at the fixed location which was followed immediately by a negative tensile pressure, which was a result of the momentum conservation. The first pressure peak (13.9 MPa peak magnitude) originated from the compressive pressure of a plane wave, and the following tensile pressure (-14.4 MPa peak magnitude) emitted from the edge of the laser spot. Both compressive and tensile components existed as determined by the law of momentum conservation (Vogel et al. 2003), and they were experienced 4.6 ns apart on the order of 10 MPa by this 50 μm fixed location. At around 66 ns, the compressive pressure wave reached the free surface and was reflected back into the coating medium as a tensile stress wave. At around 100 ns, the first reflected wave reached the fixed location with a peak magnitude of -6.4 MPa, and another compressive wave was observed with an even higher peak magnitude of 10.3 MPa due to the momentum conservation, that is, a negative tensile pressure was followed by a larger positive compressive pressure. The second pressure pair was formed due to the pressure reflection at the coating-air free

surface which changed the pressure sign when it was reflected. Also as seen from Fig. 3.6, the magnitudes of the second pressure pair both decreased since the wave energy was transmitted into the coating during traveling.

It should be pointed out that in an infinite domain the pressure evolution has only one bipolar pressure pulse pair instead of as seen from Fig. 3.6. In an infinite domain any locations in the medium experience only the original bipolar pressure pulse pair. However, in a finite medium any locations may experience many bipolar pressure pulse pairs due to reflections at the interfaces; of course, their magnitudes gradually decrease due to energy transmission. Also, if the laser spot is infinitely large the following tensile wave may not be observed since it takes infinite time for the tensile wave to travel from the laser spot edge to any locations of interest. Under this circumstance, the problem can be simplified as a 1D computation case.

Figure 3.7 further illustrates the pressure spatial distributions at 20 and 40 ns, respectively. Here the radial direction of laser spot is denoted as x and the direction along the coating thickness is denoted as z. It is found that the positive compressive wave propagated along the axisymmetric axis with a commensurate size of the laser spot since the compressive pressure wave originated from the laser spot as a plane wave. The negative tensile pressure wave lagged behind the compressive wave. The magnitudes were smaller at 40 ns due to the energy transmission within the coating medium.

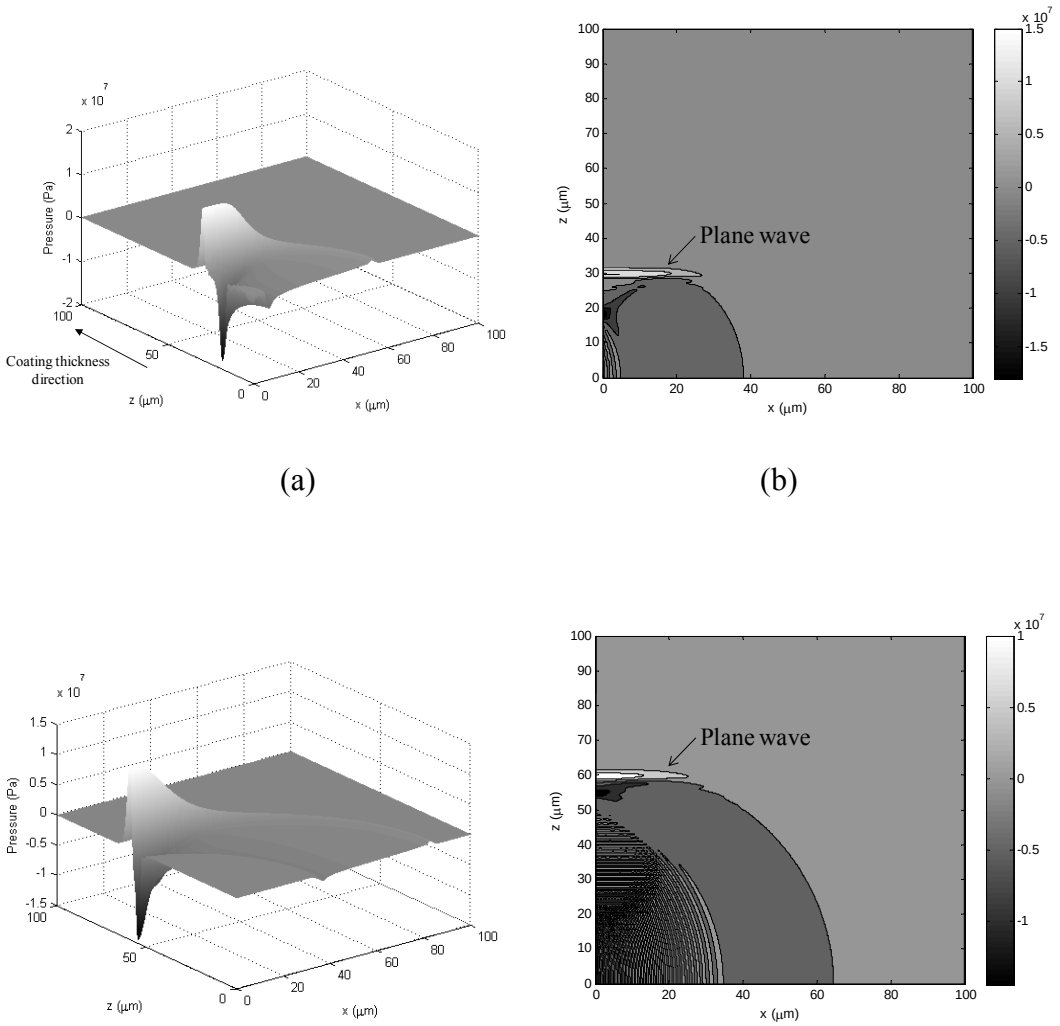

Figure 3.7: Pressure distributions: (a) 3D pressure profile at 20 ns, (b) 2D pressure profile at 20 ns, (c) 3D pressure profile at 40 ns, and (d) 2D pressure profile at 40 ns

3.3.2 Pressure Profile at Different Locations

In addition to the 50 μm location, two locations, 25 μm and 75 μm, were studied in terms of their pressure profiles experienced. Figure 3.8 shows their pressure profiles along the symmetrical axis, which is below the laser spot center. As observed, the higher

magnitudes of original laser radiation-induced pressure pulse pairs are achieved at the locations which are closer to the laser spot. However, their magnitudes of the reflected pressure pairs were smaller since it required a longer distance/time for a pressure pair to travel back, resulting in excessive energy transmission.

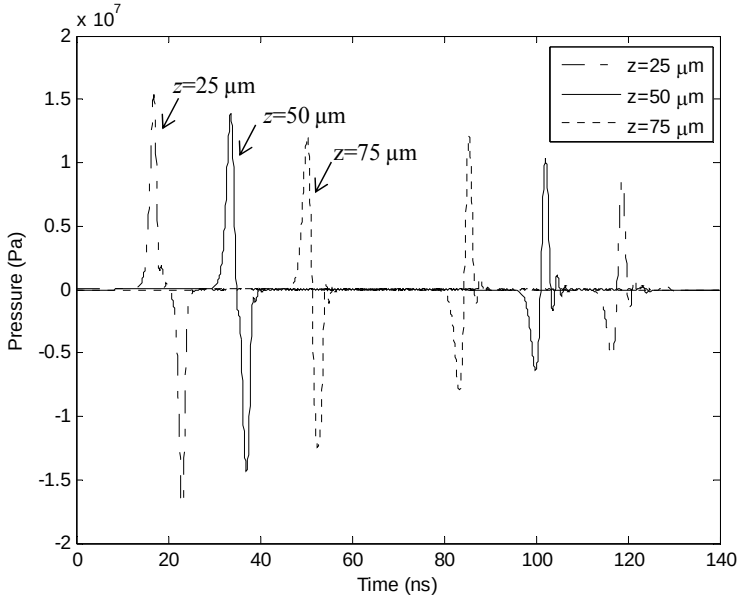

Figure 3.8: Pressure information of some locations along the axisymmetric axis

3.3.3 Pressure Profile under Different Laser Pulse Durations

The laser pulse duration also affects the magnitude of the resulting thermoelastic stresses. As shown in Fig. 3.9, a short duration laser pulse with 0.1 ns with the same laser fluence led to significantly higher thermoelastic stresses than those due to a 1 ns duration laser pulse, where $A = 0.35$ for the 1 ns pulse (Paltauf et al. 2003). It means that shorter duration laser pulses are easy to introduce damage to biomaterials in laser-assisted cell direct writing and the resulting tensile stress may induce cavitation and/or droplet formation under certain conditions.

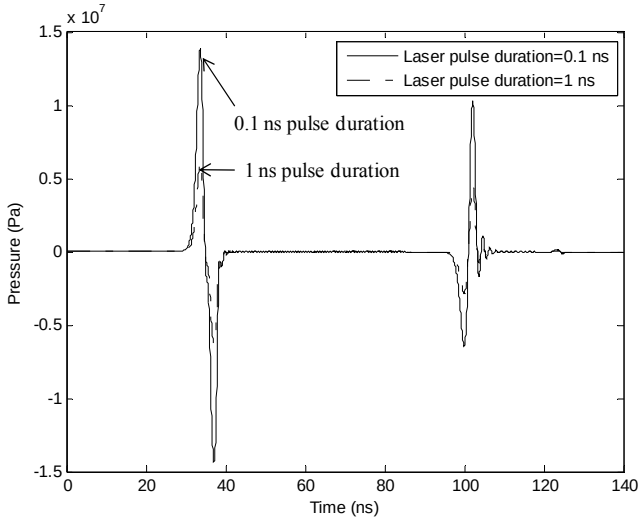

Figure 3.9: Pressure profiles at 50 μm along the axisymmetric axis under different laser pulse durations

From a pure photomechanical viewpoint, a shorter laser pulse duration can significantly increase the stress confinement factor until the laser pulse duration is about one tenth of the characteristic time of acoustic relaxation ($0.1t_{ac}$) (Paltauf et al. 2003). If the laser pulse duration is one percent of the characteristic time of acoustic relaxation, the stress confinement factor is almost 1 and the stress confinement condition is fully satisfied. Any further reduction of laser pulse duration will have no effect on the thermoelastic stress peak amplitude. In this study, the characteristic time of acoustic relaxation is around 0.667 ns, which means that a sub-nanosecond pulsed laser can completely satisfy the stress confinement condition.

3.3.4 Pressure Profile under Different Laser Fluences

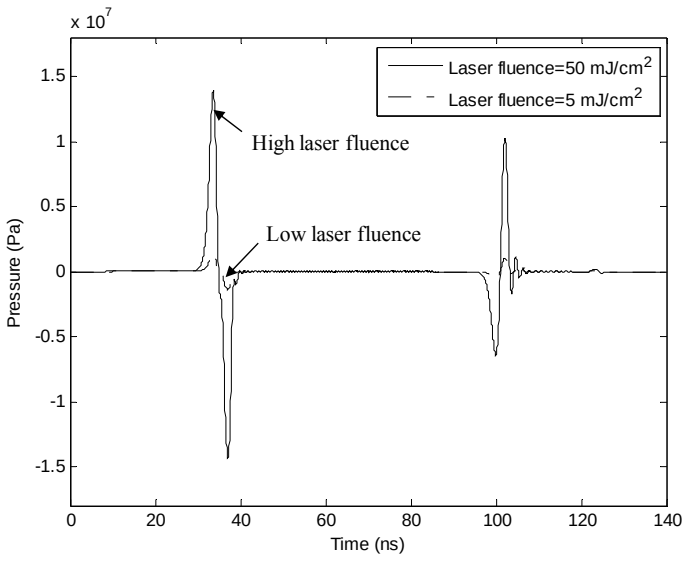

Figure 3.10: Pressure profiles at 50 μm along the axisymmetric axis under different laser pulse fluencies

The laser fluence threshold required to have the thermoelastic stress is typically lower than that required to have vaporization and plasma formation in laser-assisted direct writing. Figure 3.10 shows the resulting pressure profiles under relatively low laser fluences (5 mJ/cm^2 and 50 mJ/cm^2) which favored the generation of thermoelastic stress. As expected, the higher the laser fluence, the higher pressure magnitudes. This observation can be explained by the fact that a higher laser energy pulse results in a larger amount of energy absorbed inside the coating, leading to a higher heat source if no energy is consumed for other photochemical or photothermal processes. As a result, it promotes a higher pressure profile inside the coating. It should be pointed out that the laser fluence in this study should be lower than that required for vaporization and plasma

formation, during which photochemical or photothermal processes may be dominant. Such a laser fluence threshold value mainly depends on the laser energy absorption coefficient of coating and the laser pulse duration.

3.4 Discussion on the Thermoelastic Effect

3.4.1 Pressure Generated by the Thermoelastic Effect

In addition to possible phase explosion, thermoelastic pressure/stress always contributes to the laser-induced pressure generation in laser-assisted cell direct writing including Matrix-Assisted Pulsed-Laser Evaporation Direct-Write (MAPLE DW). The thermoelastic stress exists throughout all the laser-material interaction process; however, this thermal expansion-induced stress is usually about one order of magnitude lower than the pressure generated by other phase change processes such as phase explosion (Sigrist et al. 1978; Park et al. 1996). This thermoelastic effect-induced compressive and tensile thermoelastic stresses were reported as early as in 1964 in irradiating an aqueous liquid using a Q-spoiled ruby laser even below the laser ablation threshold (Carome et al. 1964). Similar thermoelastic stresses were concluded as the dominant pressure generation mechanism when the laser fluence was below the threshold for vaporization (Sigrist et al. 1978; Park et al. 1996). The tensile stress originating from acoustic impedance mismatch at the coating-air interface can lead to the fracture and ejection of the biomaterial coating as a droplet. While the aqueous-like coating in laser-assisted cell direct writing is usually semi-confined by the quartz support, the thermoelastic stress also easily introduces cavitation somewhere along the symmetrical axis of laser pulse direction, possibly resulting in a droplet. Under the droplet formation process, a fraction of absorbed laser

energy becomes the elastic stress energy, and the other becomes the energy to overcome the plastic deformation of the coating and the kinetic energy of the droplet formed.

It should be pointed out again that various terms such as thermoelastic stress (Vogel et al. 2003; Paltauf et al. 2003), photoacoustic pressure (Paltauf et al. 1998), pressure (Vogel et al. 2003; Paltauf et al. 2003) have been adopted in studying the laser-induced thermoelastic effect inside biological materials. Strictly speaking, thermoelastic stress should include both deviatoric stress and hydrostatic pressure. Within a solid medium, a stress tensor should be considered in studying wave propagation since both the longitudinal and transverse waves exist, and the stress components include deviatoric stress and hydrostatic pressure. However, the wave propagation process is different inside an aqueous medium as the transverse sound speed or shear wave speed equals to zero in liquids, and only the longitudinal pressure wave is usually considered in studying generated stress waves. Under such an aqueous circumstance such as the biological coating in this study, the generated thermoelastic stress can be simply referred as the pressure or the acoustic pressure, and the tensile and compressive stresses are equivalent to tensile and compressive pressures.

3.4.2 Phase Explosion Threshold under the Thermoelastic Effect

Thermoelastic stress may affect not only the pressure generation but also the phase explosion threshold during the laser-coating interaction. The onset of a tensile stress-induced phase explosion is determined by the tensile strength of liquid such as water at the room temperature (Vogel et al. 2003). In laser-assisted cell direct writing, the laser focal volume inside the coating is usually heated under the stress confinement condition, which makes it difficult to distinct the pressure contribution from the

thermoelastic effect and phase explosion. The thermodynamic phase diagram between the pressure and temperature (Vogel et al. 2003) shows that the existence of tensile thermoelastic stress can significantly reduce the free energy barrier to homogenous nucleation and the spinodal decomposition temperature. It was experimentally observed in liquid ablation that the tensile thermoelastic stress can accelerate the growth of pre-existing nucleation centers or initiate the nucleation and growth of vapor bubbles (Kim et al. 1998). It was also concluded in a review study (Vogel et al. 2003) that any tensile thermoelastic stress can increase the bubble nucleation rate for biological tissues above their boiling point; furthermore, if the tensile stress/pressure reaches a magnitude of 10 MPa, phase explosion may be initiated directly. In summary, the existence of tensile thermoelastic stress in laser-assisted cell direct writing not only helps increase the nucleation rate but also reduces the spinodal decomposition temperature.

3.5 Conclusions

The laser irradiation-induced thermoelastic stress may introduce damage to biomaterials to be transferred in laser-assisted cell direct writing. This thermoelastic stress wave propagation inside the coating medium is studied using a finite difference method-based numerical approach. Under the presence of thermoelastic stress, some main conclusions are drawn as follows:

1. The compressive pressure wave propagates along the axisymmetric axis with a commensurate size of the laser spot while there may be a following tensile stress wave if the laser spot size is finite. The laser irradiation-induced thermoelastic

stress profiles have bipolar characteristics, and their peak magnitudes are on the order of 1 MPa or higher;

2. The stress waves reflected from the coating-air free surface change its sign and have decreasing magnitude when traveling inside the coating;
3. The higher magnitudes of original laser radiation-induced pressure pulse pairs are achieved at the locations which are closer to the laser spot;
4. Shorter duration laser pulses lead to higher thermoelastic stresses; and
5. Higher laser fluence leads to higher thermoelastic stresses.

CHAPTER 4

STUDY OF IMPACT-INDUCED MECHANICAL EFFECTS IN CELL DIRECT WRITING USING SMOOTH PARTICLE HYDRODYNAMICS METHOD

4.1 Introduction

As introduced in Chapter 1, cell direct writing process can be divided into two main stages: 1) the cell droplets are ejected due to the laser energy converted momentum and 2) the cell droplets land onto a receiving substrate after traveling through a writing height (Wang et al. 2008). In the second stage of laser-assisted cell direct writing, the cell droplet reaches a receiving coated substrate. Cell damage may occur during the subsequent impact/collision with the receiving surface in landing, mainly due to mechanical effects during cell direct writing. It was found that the transferred cell viability depended on the cell droplet ejection speed and the thickness of substrate culture coating (typically hydrogel-based and used for dual-purpose as cell culture medium and impact cushion) in MAPLE DW, in which cell droplet was ejected from a quartz carrier to a receiving substrate due to the pulsed laser generated evaporation pressure (Ringeisen et al. 2004). High-speed imaging discovered that the velocities of MAPLE DW-ejected material can range from 50 to 1000 m/s (Young et al. 2001). The transferred cells are sometimes damaged if the impact between the cell and the receiving culture coating/substrate during the cell landing leads to cell shear damage including membrane rupture. By assuming the ejection-induced cell damage is negligible, the receiving coating, if necessary, is typically selected based on a trial-and-error approach to avoid the

mechanical impact-induced damage. For safe and reproducible cell direct writing, the impact-induced cell damage must be understood.

This chapter studies the cell-substrate hydrogel coating impact-induced mechanical effects in order to better understand the cell mechanical damage during cell direct writing. A previous study has been performed to understand such impact-induced mechanical effects using an auto-adaptive remeshing arbitrary Lagrangian-Eulerian finite element method (FEM) (Wang et al. 2007); however, the mesh-based FEM has some difficulties in capturing element distortion due to possible extremely large deformation of hydrogel, which is typically used as the substrate coating material. To solve the large element distortion challenge in modeling of cell printing process, the smooth particle hydrodynamic (SPH) method, which is meshfree-based, has been used in this study to model large deformations during the cell-hydrogel coating impact process.

This chapter is organized as follows. Firstly, the SPH computational procedure is introduced. Hydrogel and cell material models are also discussed. Then, the representative simulation results are presented and further discussed to appreciate the mechanical effect of process variables on the cell von Mises stress, vertical acceleration, and maximum shear strain component. Finally, the important conclusions from this study are summarized.

4.2 Computational Procedure

4.2.1 Process Governing Equations

The proposed problem is formulated for a generic cell printing process, which can be inkjet-based, laser-assisted, or EHDJ-based. The coating material is assumed as a

generic hydrogel (Wang et al. 2007). Figure 4.1 depicts a classical print setup and landing process schematic using MAPLE DW. Once a cell droplet, typically enclosed by a hydrogel, is ejected from a supporting media with an initial velocity, it travels through the air first. Eventually, the cell droplet reaches a receiving substrate, typically a glass slide coated with the hydrogel that allows for cell adhesion and growth and cell impact reduction during landing. This study assumes the cell is uniformly enclosed by the hydrogel to form a droplet, and the receiving substrate coating is also hydrogel-based.

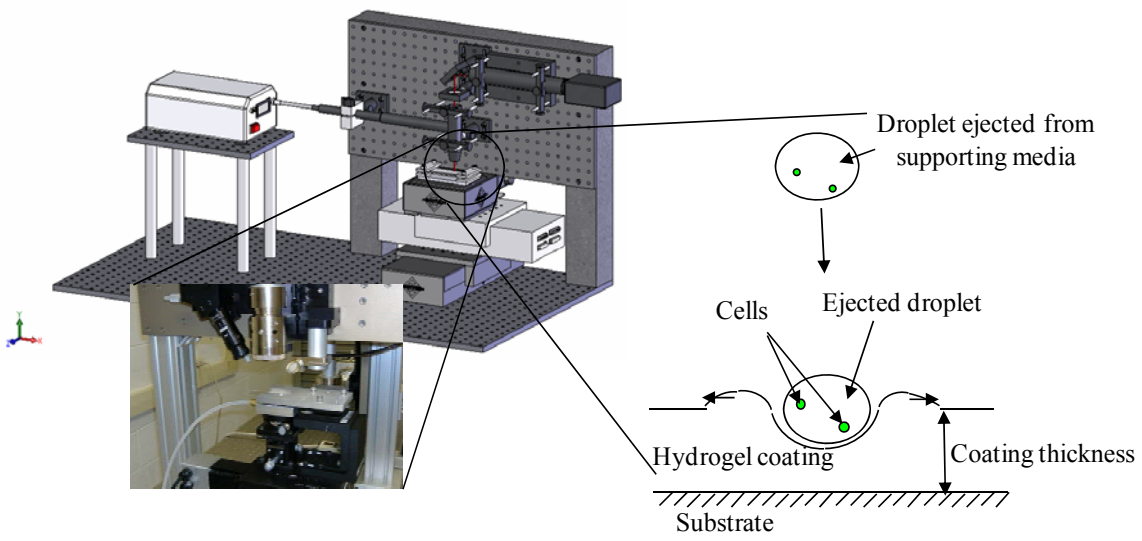

Figure 4.1: Schematic of laser-assisted direct writing

During landing, cells undergo significant deceleration and impact(s) and survive a much higher external force than they are capable of under steady state conditions. This landing process and its induced impact can be modeled using the mass, momentum and energy conservation equations, respectively, as follows:

$$\frac{d\rho}{dt} = -\rho \frac{\partial v_\alpha}{\partial x_\alpha} \tag{4.1}$$

$$\rho \frac{dv_\alpha}{dt} = \frac{\partial \sigma_{\alpha\beta}}{\partial x_\beta} \tag{4.2}$$

$$\rho \frac{dE}{dt} = \sigma_{\alpha\beta} \frac{\partial v_\alpha}{\partial x_\beta} \tag{4.3}$$

where t denotes the time, x is the spatial coordinate, ρ is the density, v_α is the velocity component, $\sigma_{\alpha\beta}$ is the stress tensor component, E is the specific internal energy, and the subscripts α (α = 1, 2, 3) and β (β = 1, 2, 3) are the component indices. The above equations hold true for cells and both hydrogels of the droplet and the substrate coating. Besides boundary and initial conditions, proper material models, which include equation of state, constitutive model, and failure criteria, are also indispensable in solving Eqs. (4.1-4.3). The equation of state is used to define the corresponding functional relationship between pressure, density, and internal energy. The constitutive model defines the stress dependence of related strain, stain rate and temperature. In addition, a material model also generally includes a failure criterion to determine whether the material fails and loses its ability to support stress/strain.

4.2.2 SPH Method

Smoothed particle hydrodynamics (SPH) method is a Lagrangian formulation-based computational method (where the coordinates move with the object), which was originally developed for astrophysics and shock simulations (Gingold et al. 1977; Lucy 1977). After that, it has been applied to various fields such as hyper-velocity deformation Johnson et al. 1996), detonation (Liu et al. 2003), and fluid dynamics (Ellero et al. 2005), to name a few.

Using the SPH method, the whole computational domain is divided into a set of discrete particles or nodes. These particles have a spatial distance, known the smoothing

length, over which their properties are smoothed by a kernel function. Different from standard FEM methods, SPH approximates physical quantities of each particle using a kernel function. Smoothing length usually varies in both time and space, and the common kernel functions include the Gaussian function and the cubic spline function. Because it is Lagrangian in nature, SPH is limited to refining based on the particle density alone.

The most attractive feature of this meshfree SPH method is that it gets rid of the computation termination due to possible large element distortion inherent in other Lagrangian formulation-based finite element methods. It is expected that SPH can capture the cell-hydrogel coating impact process better.

4.2.2.1 SPH Approximation

In SPH, the computational domain is first discretized into a finite number of particles. The particle approximation ($< f(x) >$) of a function at any spatial coordinate x ($f(x)$) can be represented as follows (Monaghan et al. 1983; Ellero et al. 2005):

$$< f(x) >= \int f(x')W(x - x', h)dx' \tag{4.4}$$

where W is a kernel function, the angle bracket < > denotes a kernel approximation, h is the smoothing length which varies in both time and space, x' is new independent variable, and "'" here and in the following denotes new dummy independent variables.

By introducing a volume weight m_j/ρ_j for each particle, the particle approximation of a function can now be defined by:

$$< f(x) >= \sum_{j=1}^{N} \frac{m_j}{\rho_j} f(x_j)W(| x - x_j |, h) \tag{4.5}$$

where m_j and ρ_j are the mass and density associated with the jth particle, respectively, N is the number of particles, and "| |" denotes the absolute operator. Thus, the particle

approximation for each particle *i* can be approximated by summing the contributions of neighboring particles *j* as follows:

$$< f(x_i) >= \sum_{j=1}^{N} \frac{m_j}{\rho_j} f(x_j) W(| x_i - x_j |, h) \tag{4.6}$$

4.2.2.2 SPH Formulation

Equations for SPH numerical implementation are constructed by multiplying each term of the exact governing equations (Eqs. (4.1-4.3)) by the kernel and integrating over the domain where a solution is required. Using the kernel interpolation, the basic SPH mass, momentum and energy governing equations can be written as follows, respectively:

$$\left\langle \frac{d\rho}{dt} \right\rangle = -\int W \rho' \frac{\partial v'_\alpha}{\partial x'_\alpha} dx' \tag{4.7}$$

$$\left\langle \frac{dv_\alpha}{dt} \right\rangle = \int W \frac{\partial}{\partial x'_\beta} \left(\frac{\sigma'_{\alpha\beta}}{\rho'} \right) dx' + \int W \frac{\sigma'_{\alpha\beta}}{\rho'^2} \frac{\partial \rho'}{\partial x'_\beta} dx' \tag{4.8}$$

$$\left\langle \frac{dE}{dt} \right\rangle = \int W \frac{\sigma'_{\alpha\beta}}{\rho'^2} \frac{\partial (\rho' v'_\alpha)}{\partial x'_\beta} dx' - \int W \frac{\sigma'_{\alpha\beta} v'_\alpha}{\rho'^2} \frac{\partial \rho'}{\partial x'_\beta} dx' \tag{4.9}$$

Then, the finial discrete forms of governing equations can be expressed as follows (Monaghan et al. 1983):

$$\frac{d\rho^i}{dt} = \rho^i \sum_{j=1}^{N} \frac{m^j}{\rho^j} (v_\beta^j - v_\beta^i) \frac{\partial W^{ij}}{\partial x_\beta^i} \tag{4.10}$$

$$\frac{dv_\alpha^i}{dt} = -\sum_{j=1}^{N} m^j (v_\beta^j - v_\beta^j) \frac{\partial W^{ij}}{\partial x_\beta^i} \tag{4.11}$$

$$\frac{dE^i}{dt} = -\frac{\sigma_{\alpha\beta}^i}{\rho^{i2}} \sum_{j=1}^{N} m^j (v_\alpha^j - v_\alpha^i) \frac{\partial W^{ij}}{\partial x_\beta^i} \tag{4.12}$$

where $W^{ij} = W(x^i - x^j, h)$.

Simulation solutions are obtained by solving Eqs. (4.10-4.12) in conjunction with material models and initial and boundary conditions.

4.2.3 Material Models

The complete definition of a transient non-linear dynamics problem requires the material models that define the relationships among the flow variables (pressure, mass density, energy density, temperature, etc.). These relations typically involve an equation of state, a constitutive equation, and a failure equation for each constituent material. In the present study, the following two materials are utilized within the computational domain: hydrogel (of either the droplet or the substrate coating) and cell. In the following sections, a brief description is given of the models used for hydrogel and cell.

4.2.3.1 Hydrogel

Natural and synthetic hydrogels contain water within a three-dimensional network of polymer chains (Stammen et al. 2001). By their nature, hydrogels are highly fluid-like solids which are water swollen, cross-linked, and hydrophilic polymers. Due to their biocompatibility and the ease of their synthesis, the gels have been extensively used as cell culture and proposed for a wide range of biomedical applications (Vijayasekaran et al. 1998; Young et al. 1998). The physical and biochemical properties of a particular hydrogel are highly dependent on its local structure characteristics, constituents and chemical environment, etc. (Wang et al. 2004; Nam et al. 2005). Hydrogel mechanical properties have been of interest for a long time (Roeder et al. 2002; Drury et al. 2004), and some hydrogel mechanical property characterization studies have been reported (Roeder et al. 2002; Drury et al. 2004; Lin et al. 2004). However, a complete understanding of hydrogel mechanical properties is still lacking.

The equation of state of hydrogel is expected to provide a hydrodynamic material model by which the hydrogel volumetric strength can be determined. The Mie-Grüneisen equation of state as shown in Eq. (4.13) (LS-DYNA 2006) provides the shock velocity-particle velocity Hugoniot form and was used to define the equation of state of hydrogel:

$$P = \frac{\rho_0 C^2 \mu \left[1 + \left(1 - \frac{\gamma_0}{2}\right)\mu - \frac{a}{2}\mu^2\right]}{\left[1 - (S_1 - 1)\mu - S_2 \frac{\mu^2}{\mu + 1} - S_3 \frac{\mu^3}{(\mu + 1)^2}\right]} + E_i(\gamma_0 + au) \tag{4.13}$$

where P is the hydrogel pressure, C is the intercept of the U_s-U_p curve (sound velocity), U_s is the speed of a shockwave through the material, U_p is the speed of the shocked material, S_1, S_2, and S_3 are the coefficients of the slope of the U_s-U_p curve, γ_0 is the Grüneisen gamma, E_i is the initial internal energy, a is the first order volume correction to γ_0, the compression μ is defined as $\mu=\rho/\rho_0$-1, and ρ and ρ_0 are the density and initial density. The Mie-Grüneisen equation is typically determined based on the material parameters C, S_1, S_2, S_3 and γ_0 as specified by LS-DYNA (LS-DYNA 2006). In this study, since water is the dominant component of hydrogel, the parameters for water were used to define the hydrogel equation of state to simplify the problem.

Null material model has been adopted by LS-DYNA to model the fluid-like materials (LS-DYNA 2006). Since the hydrogel demonstrates fluid-like behavior during large deformation, for simplicity, the null material model provided by the LS-DYNA material library was used as the hydrogel constitutive model. When using the null material model, pressure and deviatoric stress are decoupled in SPH simulation. The pressure is determined by the equation of state as Eq. (4.13), and the deviatoric stress is calculated based on the strain rate and viscosity as follows:

$$\sigma_{\alpha\beta}^{D} = 2\mu_h \dot{\varepsilon}_{\alpha\beta}^{D} \tag{4.14}$$

where $\sigma_{\alpha\beta}^{D}$ is the deviatoric stress, μ_h is the hydrogel viscosity, and $\dot{\varepsilon}_{\alpha\beta}^{D}$ is the deviatoric strain rate.

Hydrogel loses its mechanical loading bearing capacities under certain stress/strain conditions. As a result, the cell droplet may penetrate into the hydrogel coating during the subsequent processes. Cutoff pressure is used to control the hydrogel failure by allowing the hydrogel to numerically cavitate when the hydrogel undergoes dilatation above a certain magnitude. The pressure information of the landing process can be determined using the hydrogel equation of state.

4.2.3.2 Cell

During the cell printing process, the cells which are enclosed by the hydrogel, also undergo complexly dynamic stress and strain variations. Due to the complexity of cell structure and compositions, numerous constitutive models have been developed to characterize mechanical responses of living cells when subjected to both transient and dynamic loads (Lim et al. 2006). Generally, cell models can be considered on two levels, macroscopic continuum approaches, and microscopic structural approaches. The continuum approach aims to investigate the overall behavior of cells while microscopic structural approaches focus on the effect from the local component deformation of cells.

The linearly elastic solid cell model was selected in this study due to its simplicity and adequateness. The whole cell is assumed as homogeneous without considering the distinct cortical layer. The linearly elastic solid model is a simplification of the viscoelastic model when the time factor is neglected.

A linearly elastic material can be described as follows by defining $T^D_{\alpha\beta} = T_{\alpha\beta} + p\delta_{\alpha\beta}$ and $\varepsilon^D_{\alpha\beta} = \varepsilon_{\alpha\beta} - \frac{1}{3}e\delta_{\alpha\beta}$ (Malvern 1969):

$$T^D_{\alpha\beta} = 2G\varepsilon^D_{\alpha\beta} \text{ and } p = -Ke \tag{4.15}$$

where $T^D_{\alpha\beta}$ is the deviatoric components of stress components $T_{\alpha\beta}$, $\varepsilon^D_{\alpha\beta}$ is the deviatoric components of the strain components $\varepsilon_{\alpha\beta}$, G is the shear modulus, p is the cell mean normal pressure (hydrostatic pressure), $e = \varepsilon_{11} + \varepsilon_{22} + \varepsilon_{33}$ is the volume strain, $\delta_{\alpha\beta}$ is the Kronecker delta, and K is the bulk modulus.

An equation of state is not necessarily required for pressure calculation when using an elastic constitutive model for cell as specified by LS-DYNA. If the pressure information is of interest, the pressure can be computed using the resultant stress tensor information from the constitutive model.

Since the goal of this study is to study the companying cell stress and strain distribution during the dynamic landing process, the cell failure is not of interest here and the predicted stress and strain values are not compared with the failure threshold values of any cells. This study serves as a foundation for future cell damage/failure modeling during cell direct writing.

4.3 Simulation Setup and Results

4.3.1 Meshfree Model Setup

As the first step toward cell damage modeling during cell direct writing, this study has only considered the case that there was one cell inside a droplet and the cell was in

the middle of the droplet. Once the cell droplet left from the ejecting device, the cell droplet was assumed to impact the hydrogel coating in a normal direction. The initial droplet velocity was the impact velocity when the cell droplet first reached the coating, and the positive velocity direction was defined vertically downward as shown in Fig. 4.2.

In a meshfree method, the particle grid density is crucial for computation implementation. Uniform grid distribution was used in this study. The hydrogel coating bottom was supported by a rigid substrate and modeled as a rigid boundary condition, and the rigid wall model in LS-DYNA was used to model the rigid impact between the particle flow and the rigid substrate body. The rigid wall model was applied to other coating surrounding boundaries in order to limit the particles to flow through since the coating size along the X and Y dimensions (both 100 μm) was considered infinite than that of the cell droplet in this study, and there was negligible differences in simulations when even larger XY dimensions were tested. The coating surface was modeled as a free surface. To reduce the computational cost, a symmetrical plane was used so that a half model was applicable (Fig. 4.2).

The schematic of the grids implemented is shown in Fig. 4.2. Totally 20692 particles are used, in which 456 for the cell, 1486 for the droplet hydrogel, and 18750 for the hydrogel coating, respectively. The particle numbers were selected based on a modeling accuracy sensitivity study. The smoothing length was selected from 0.8 to 1.0. The hydrogel droplet diameter was assumed 18 μm, and the cell diameter 6 μm (Lanero et al. 2006). Fig. 4.3 shows the positions of selected particles, which are of interest in the following discussion.

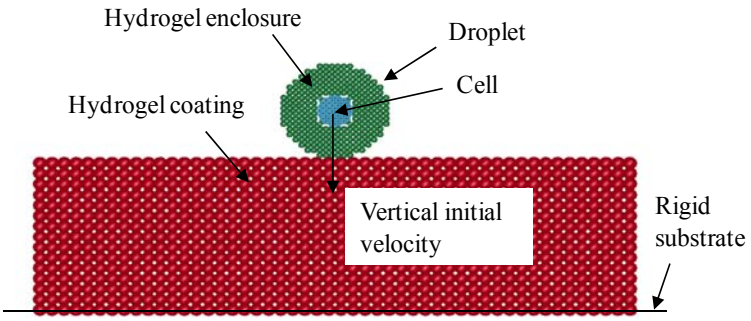

Figure 4.2: Illustration of SPH computational modeling domain

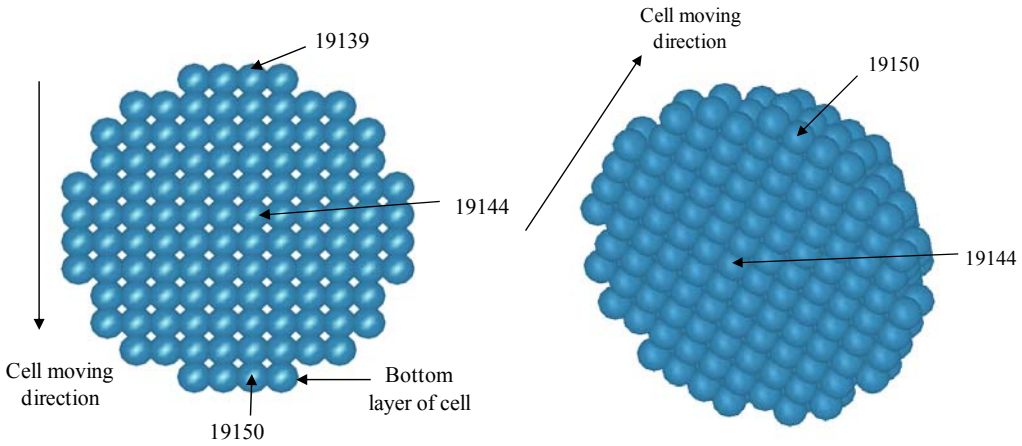

Figure 4.3: Distribution of the selected particles in the cell and its 3D visualization

As discussed, the null material model was implemented as the hydrogel constitutive model to model the fluid-like material behavior of hydrogel. The equation of state parameters of water were adopted for hydrogel as C = 1500 m/s, S_1 = 2.56, S_2 = -1.986, S_3 = 0.2268 and γ_0 = 0.5 (Lysne 1970; Liu et al. 2002). The hydrogel initial density was taken as 1000 kg/m^3 and viscosity as 12 centipoises (Nam et al. 2005). The failure

cutoff pressure of hydrogel was set as 25 kPa (Wang et al. 2007). The density of cell was also assumed 1000 kg/m^3; the Young's modulus 1.79 MPa (Lanero et al. 2006), and Poisson' ratio 0.475 for simplicity (Wang et al. 2007).

4.3.2 Representative Simulation Results

4.3.2.1 Evolution of a Landing Process

Some representative simulation results of landing are presented when a 50 m/s (V_0) cell droplet hit a rigid substrate coated with a 30 μm thick hydrogel. Figure 4.4 shows the evolution of the whole landing process. It can be seen that there were two different impacts during the whole process under the specified conditions. The first impact was between the cell droplet and the hydrogel coating, and the second impact was between the cell and the rigid substrate after the cell passed through the coating after the first impact.

As the landing process went on, the hydrogel-enclosed cell droplet gradually merged into the substrate coating. Before the cell immersed into the coating (Figs. 4.4(a-b)), it was the outside hydrogel enclosure that was mainly subject to the impact-induced stress. It shows that the outside hydrogel enclosure of the cell played an important role in alleviating the impact-induced stress to the cell by absorbing the strain energy. Around 0.1600 μs later, the impact between the cell and the hydrogel coating occurred. After the cell immersed into the coating (Figs. 4.4(c-d)), the outside hydrogel enclosure and the coating bore relatively lower stresses although the cell experienced higher stresses.

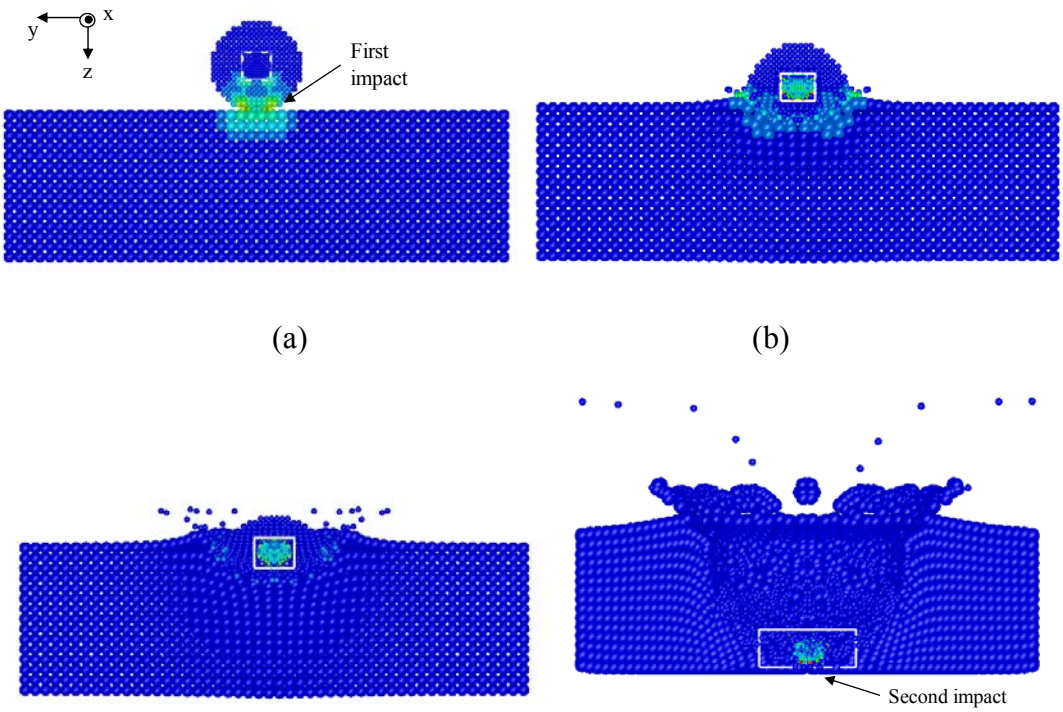

Figure 4.4: Landing process at (*a*) 5.9322 ns, (b) 0.1359 μs, (c) 0.2725 μs, and (d) 2.4865 μs

4.3.2.2 Von Mises Stress and Shear Strain

To study the von Mises stress and shear strain information during the landing process, three particles, the top particle 19139, the inner particle 19144 (one of the four center particles), and the bottom particle 19150, were selected as the representative positions to better understand the overall cell responses during the landing process. The simulation was performed under the condition of coating thickness = 30 μm and V_0 = 50 m/s.

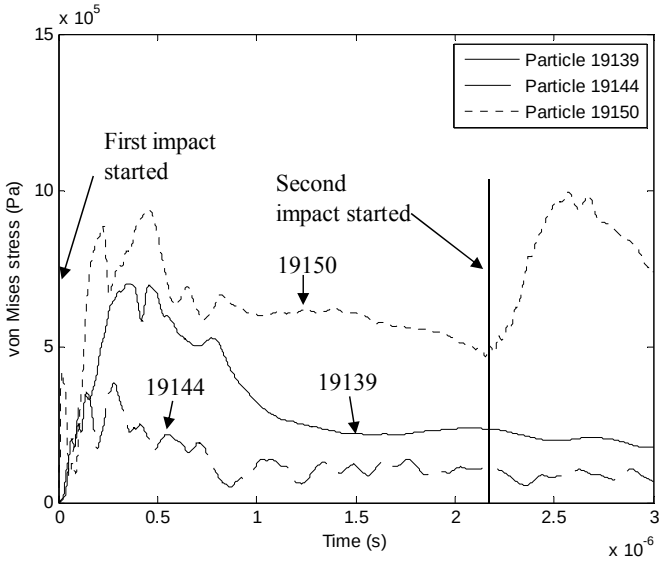

Figure 4.5: Particle von Mises stress information (coating thickness = 30 μm and V_0 = 50 m/s)

The particle von Mises stress responses are shown in Fig. 4.5. It can be seen from the stress profiles that there were two different impacts during the whole process under the specified conditions. The first impact happened at the computation starting time, and the second impact happened around 2.2 μs. The von Mises stress level was comparable with that of a previous study using the arbitrary Lagrangian-Eulerian FEM (Wang et al. 2007), and both were at the order of 10^5 Pa. During the whole process, the peripheral particles 19139 (top) and 19150 (bottom) were subject to a higher stress level than that of the inner particle 19144, which indicates that the cell membrane had a higher impact-induced mechanical stress during cell direct writing. Also, the bottom particle 19150 underwent a higher stress than that of the top particle 19139. Figure 4.5 also shows that the second impact had a negligible effect to the particles 19139 (top) and 19144 (inner);

however, the bottom particle 19150 had an even higher stresses during the second impact than that during the first impact (1.33 MPa vs. 0.96 MPa), which means that it is of importance to study the stress information of the bottom particles during the both impacts.

In this simulation, the bottom particle 19150 experienced the first impact-induced stress peak at 0.2 μs and the second peak around 2.6 μs. It is found that the bottom peripheral particles were easy to have a second impact, followed by the top peripheral particles, then the inner particles.

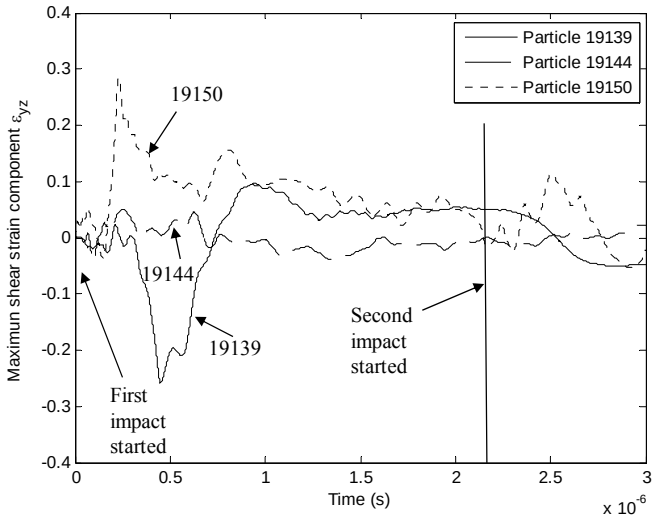

Figure 4.6: Particle maximum shear strain component information (coating thickness = 30 μm and V_0 = 50 m/s)

Figure 4.6 shows the maximum shear strain information of the three particles of interest. The maximum shear strain component was found along the YZ direction (ε_{yz}) as shown in Fig. 4.4(a). It can be seen that the peripheral particles (19139 and 19150) had

a larger shear deformation, which indicates a good chance of cell membrane to be ruptured during the impact process if the shear strain is the cell failure criterion.

4.3.2.3 Velocity and Acceleration

The same particles 19139 (top), 19144 (inner), and 19150 (bottom) were selected to study their velocity and acceleration responses during the landing process (coating thickness = 30 μm and V_0=50 m/s). All velocity and acceleration information here was about their vertical components along the Z direction since the velocity and acceleration at the other directions were relatively small as observed.

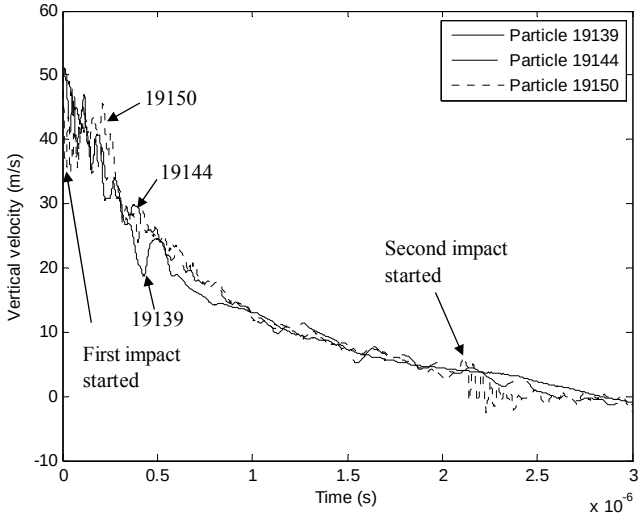

Figure 4.7: Particle vertical velocity information (coating thickness = 30 μm and V_0 = 50 m/s)

Figure 4.7 shows the velocity history of the three particles until they settled down on the rigid substrate. After the first impact, the bottom particle (19150) first experienced a velocity decrease, followed by the inner and top particles (19144 and 19139). The velocity decrease observed from Fig. 4.7 was oscillatory because of the material models

used (the elasticity of cell and the fluid-type property of hydrogel). It can be seen that the velocity differences at the different positions was relatively larger at the beginning of the landing process, and then the difference smoothed out. The second impact caused an additional velocity oscillation around 2.2 μs, especially to the bottom particle (19150), which can be further seen from the acceleration profile in Fig. 4.8. Finally, all particles were still at end of the landing process.

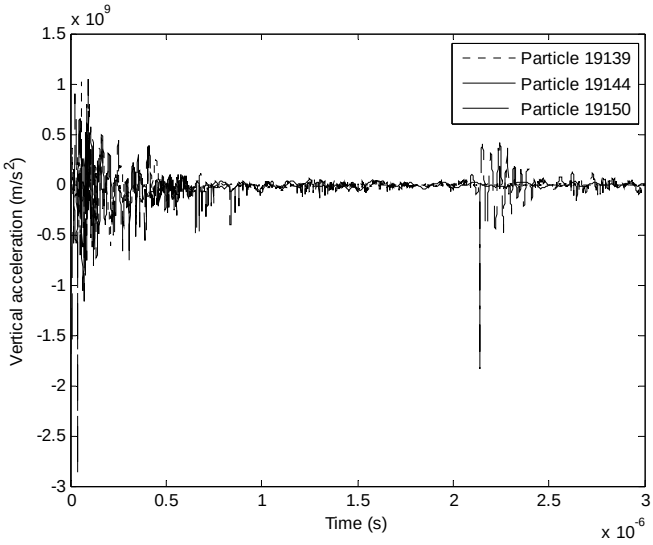

Figure 4.8: Particle vertical acceleration information (coating thickness = 30 μm and V_0 = 50 m/s)

As seen from Fig. 4.8, the particle decelerated as high as 10^8 -10^9 m/s^2 during cell direct writing, which is consistent with a previous FEM study (Wang et al. 2007) and comparable with other simple estimations (at the order of 10^7 m/s^2) (Ringeisen et al. 2004). Generally, the absolute acceleration magnitude became smaller and smaller and eventually approached zero in an oscillation manner. Absolute magnitudes of acceleration depend on the material properties of the hydrogel and the cell, coating

thickness and droplet initial velocity. As discussed before, the bottom particle 19150 experienced another negative peak of acceleration (deceleration) due to the second impact, which indicates that the bottom particles are easily subject to the second impact than particles at other positions.

Two conclusions can be drawn based on the above velocity and acceleration simulation. Firstly, relatively larger oscillations of velocity and acceleration are expected at the beginning of the first impact, and the velocity and acceleration differences between different particles smooth out as the landing process goes on. Secondly, the bottom peripheral cell membrane experiences a higher impact effect than other locations.

4.3.3 Effect of Process Variables and Discussion

If cell damage during cell direct writing is of interest, the effect of typical process variables such as the droplet initial velocity and the coating thickness needs to be carefully studied. For example, the receiving coating, if necessary, has been typically selected based on a trial-and-error approach to avoid mechanical stress-induced damage/necrosis. In this section, the effect of droplet initial velocity and coating thickness on cell stress, acceleration, and shear strain component is investigated and further discussed. Since the bottom particle 19150 usually underwent relatively severe mechanical loadings compared with particles at other positions as discussed in the above section, it was selected as the representative particle/cell membrane position to be studied.

4.3.3.1 Effect of Initial Velocity

To study the effect of droplet initial velocity, some typical speed values such as 50 m/s, 100 m/s and 300 m/s were selected. Figure 4.9 presents the comparisons of von

Mises stress, vertical acceleration, and maximum shear strain component of the bottom particle 19150 under the three different initial velocities. As expected, the absolute magnitudes of effective stress, vertical acceleration, and maximum shear strain showed a close relationship with the initial velocity. A higher initial velocity led to a higher stress level, larger acceleration, and larger maximum shear strain component. If mechanical damage is of concern, lowering the magnitude of cell droplet ejecting velocity can effectively reduce the mechanical impact on cells, protecting cells from the mechanically induced damage. Therefore, it is important to control the initial velocity within a certain range such that the excessive stress level, large acceleration, and/or large shear strain can be avoided.

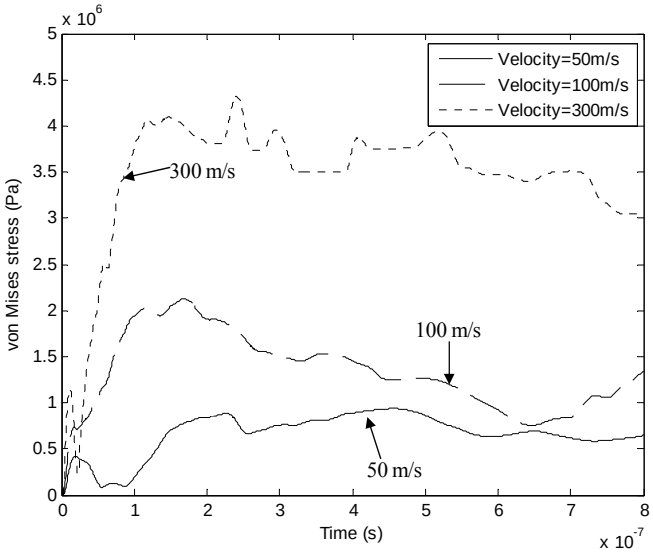

(a)

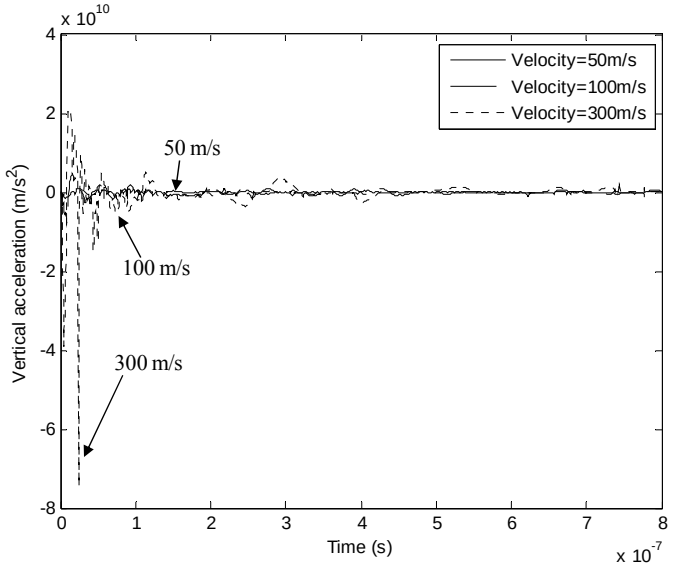

(b)

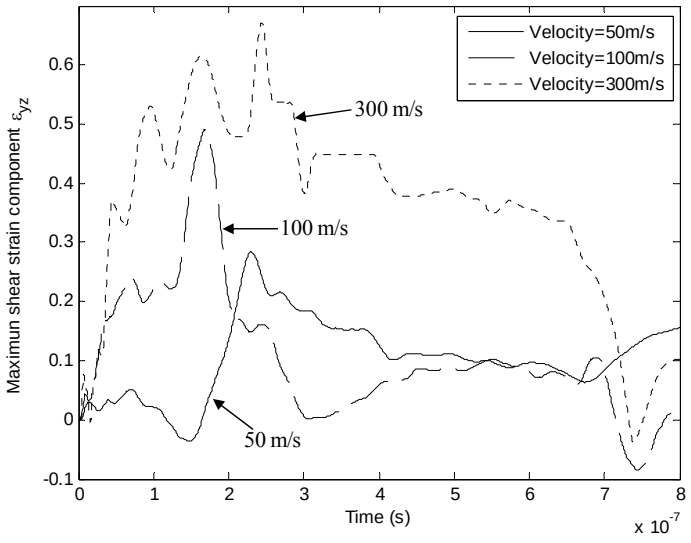

(c)

Figure 4.9: von Mises Stress, vertical acceleration, and maximum shear strain component information of the bottom particle 19150 at different velocities (coating thickness = 30 μm)

4.3.3.2 Effect of Coating Thickness

To fully understand the effect of coating thickness, some typical coating thickness values such as 0 μm (uncoated), 20 μm and 40 μm were selected for simulation. Figure 4.10 presents the comparisons of von Mises stress, vertical acceleration, and maximum shear strain component of the bottom particle 19150 using the different coating thicknesses.

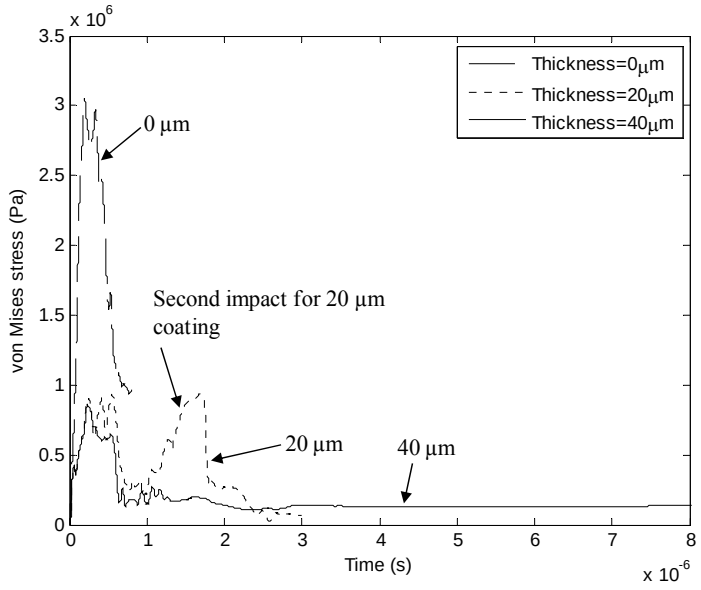

(a)

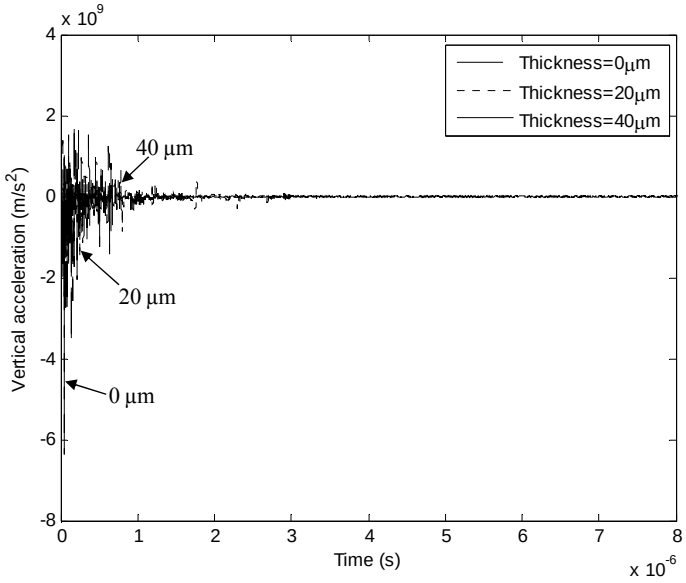

(b)

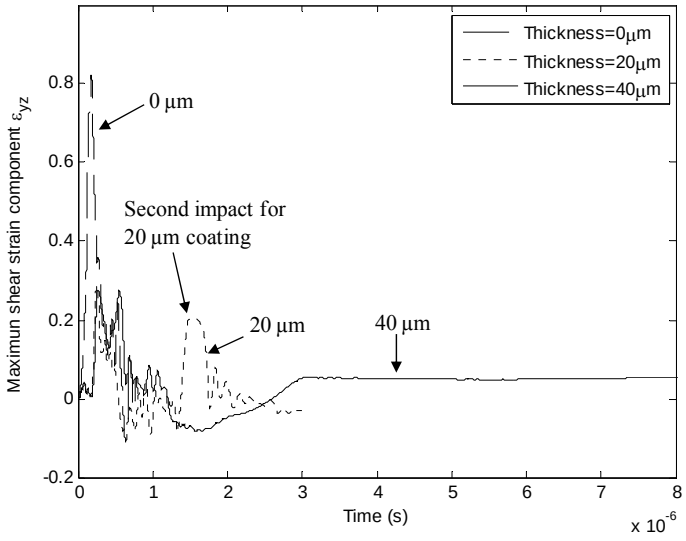

(c)

Figure 4.10: von Mises Stress, vertical acceleration, and maximum shear strain component information of the bottom particle 19150 at different thicknesses (initial velocity = 50 m/s)

As expected, cell experienced significantly higher von Mises stress, vertical acceleration, and maximum shear strain using the uncoated substrate (thickness = 0 μm) than those using the coated substrates. Even a thin coating such as a 20 μm thick hydrogel coating helped to reduce the possible mechanical damage by several times. It is seen that the maximum von Mises stress using the uncoated substrate was reduced from 3 MPa to be around 1 MPa using a 20 or 40 μm thick coating. Similar protective effect of a coating can also be observed in terms of the vertical acceleration and maximum shear strain component as seen from Fig. 4.10. Generally, the mechanical damage to cell can be evaluated based on the criteria of von Mises stress, acceleration, and/or shear strain. Whichever the criterion is to be used, the cell mechanical damage can be reduced and the cell viability can be improved using a proper coating as reviewed from Fig. 4-10.

The protective effect of coating has also been experimentally verified during laser printing of pluripotent embryonal carcinoma cells (Ringeisen et al. 2004). Based on that study, 5% cell viability after printing was achieved using an uncoated quartz receiving substrate; however, roughly 50% of the cells transferred onto a thinner hydrogel coating (20 μm) appeared to remain viable posttransfer, whereas viability reached 95% for cells transferred onto a thicker coating (40 μm). However, by reviewing Fig. 4.10, it is found that there were no pronounced differences between the maximum von Mises stresses or the maximum shear strain components when using the 20 μm or 40 μm thick coating. If the cell viability is just evaluated based on the maximum von Mises stress or the maximum shear strain component, it is difficult to explain why the 40 μm coating helped achieve almost a doubled cell viability compared with that using the 20 μm coating. The reason that the cell viability was lower using the 20 μm coating is attributed to the second

impact between the cell and the rigid substrate around 1.7 μs while there was no pronounced second impact using the 40 μm coating.

4.4 Discussion

Table 4.1: Maximum von Mises stress and shear strain component information during impacts of the bottom particle 19150 (N.A.: not applicable)

Velocity (m/s)	Coating thickness (μm)	Maximum von Mises stress (MPa)		Maximum shear strain component (ε_{yz})	
		During 1st impact	During 2nd impact	During 1st impact	During 2nd impact
50	0	3.05	N.A.	0.8225	N.A.
	20	0.92	0.94	0.2884	0.2067
	40	0.86	N.A.	0.2771	N.A.
100	0	6.04	N.A.	0.8401	N.A.
	20	1.90	2.72	0.5214	0.3886
	40	1.95	1.30	0.5181	0.2646

To further appreciate the effect of droplet initial velocity and coating thickness on maximum von Mises stress and shear strain component during impact, a comparison study has been performed for the bottom particle 19150 under the different combinations of velocity and coating thickness, and the results are shown in Table 4.1.

Generally, cell mechanical damage mechanisms can be mitochondria swelling, cell membrane rupture, endoplasmic reticulum dilation, and vacuole formation, which

make cells die during cell direct writing. Regarding the maximum von Mises stress, it can be found from Table 1 that:

1. While there was no pronounced difference when using a 20 or 40 μm thick coating, there was a three times difference between the coated and uncoated cases during the first impact under the investigated velocities;

2. If a thin coating did not provide enough damping during the interaction between the cell droplet and the coating, the second impact might cause an even higher effective stress to the cell especially as seen from the scenario using a 100 m/s velocity and 20 μm coating since the second impact was between the cell and the rigid substrate. Even the cell velocity was lower during the second impact as seen from Fig. 4.7, and the impact between the cell and the rigid substrate might lead to a higher impact force as a result of the combined effect of velocity and nature of the second impact (the impact with a rigid surface);

3. Although the stress levels were comparable during the first impact for both coated cases, the mechanical damage to cells might be different depending on the following second impact. As discussed in the previous section, when a 20 or 40 μm thick coating was used, the first impact-induced stress was found comparable as 0.92 MPa vs. 0.86 MPa and 1.90 MPa vs. 1.95 MPa; however, the cell viability was 50% vs. 95%. It indicates that the stress profile after the first impact and/or the second impact-induced stress peak should also be included to determine the cell posttransfer viability. It is known that the cellular response to mechanical injuries is adaptive to restore a normal homeostasis and protect the cell from progressive damage (Barbee 2005; Serbest et al. 2006). Cell injury by mechanical trauma is closely related with the mechanical loading

method since the cellular response varies according to the method used to induce the mechanical injury (Geddes-Klein et al. 2006). It is assumed that the second impact-induced stress peak may happen before a cell has time to restore homeostasis, which leads to a lower cell posttransfer viability during cell direct writing. The loading history experienced by cells is also critical in determining cell damage. It should be pointed out that the simulation results should adequately represent a general cell droplet landing process for us to draw the above conclusion although the material properties of cell and hydrogel are not exactly the same as in (Wang et al. 2007); and

4. Typically, cells such as yeast cells fail mechanically around 70±4 MPa (Smith et al. 2000) which is one order higher than those predicted in this study. It looks like that fragile mammalian cells die at much lower stress levels during cell direct writing as seen from Table 1. There are two possible reasons for this discrepancy: the pluripotent embryonal carcinoma cell (Ringeisen et al. 2004) is fragile while the yeast cell is relatively tough; and the dynamic mechanical loading makes cells difficult to restore their normal homeostasis (Barbee 2005; Serbest et al. 2006; Geddes-Klein et al. 2006) as discussed before.

Similar magnitude observations/tendencies of the maximum shear strain component have been found while comparing with those of the von Mises stress except that the maximum shear strain component of the second impact (if have) was always smaller than that of the first impact. It should be noted that since the cell failure is not considered here and the predicted stress and strain values were not compared with any failure criteria, some unrealistic shear strains were predicted such as 0.8225 and 0.8401

for uncoated cases. It is expected that more realistic strain values can be predicted if a cell failure criterion for a certain type cell is implemented in future studies.

It should be pointed that this simple elastic model is not adequate to study the mechanical response of the different components of the cell. The assumption that the cell is homogenous and behaves in a linear elastic manner ignores a number of potential important features of real cells. Since the general stress and strain information is of interest, this elastic model is sufficient for this preliminary study. A more realistic inhomogeneous, nonlinear cell constitutive model should be considered for landing modeling and cell damage and failure modeling.

In summary, it is assumed that the impact-induced cell damage depends on not only the magnitudes of stress, acceleration, and/or shear strain but also the loading history that a cell experiences. In fact, the collective cell momentum change over the whole impact duration instead of peak values of stress, acceleration and/or strain looks critical in determining the cell viability during cell direct writing. This loading history-based damage prediction approach should be further carefully addressed in future investigations. It should be noted that once the coating thickness reaches a certain value, there is no extra benefit for mechanical damage-induced cell viability improvement. This critical thickness value depends on the cell droplet initial velocity and the material properties of the cell and the hydrogel.

4.5 Conclusions

The impact between the cell droplet and the substrate coating and the impact between the cell and the substrate have been carefully studied using a meshfree SPH

method in this study. The effects of cell droplet velocity and coating thickness on the cell stress, acceleration and shear strain during landing have been carefully investigated and discussed. Some conclusions can be drawn as follows:

1. The cell peripheral regions, especially the bottom peripheral region, usually experience a higher stress level than that of the inner regions. It indicates that the cell membrane is easy to be adversely affected by the impact-induced mechanical damage during cell direct writing.
2. The cell mechanical loading profile and the cell posttransfer viability depend on the cell droplet initial velocity and the substrate coating thickness. Generally, a larger initial velocity poses a higher probability of cell damage, and a substrate coating can significantly reduce the cell mechanical damage severity.
3. Two important impact processes may occur during the cell droplet landing process after ejection: the first impact between the cell droplet and the substrate coating and the second impact between the cell and the substrate. It is assumed that the impact-induced cell damage depends on not only the magnitudes of stress, acceleration, and/or shear strain but also the cell loading history. In fact, the collective cell momentum change over the whole impact duration instead of peak values of stress, acceleration and/or strain looks critical in determining the cell viability during cell direct writing.
4. For better understanding of cell damage during direct writing, future studies should apply realistic cell and hydrogel constitutive models, consider the mechanical damage during the cell droplet formation process (ejection), and

include the possible process-induced thermal damage. Also, how to quantify the cell damage degree should be carefully addressed, validated and interpreted.

CHAPTER 5

MOLECULE SIGALING PATHYWAY-BASED CELL DAMAGE MODEL IN LASER-ASSISTED CELL DIRECT WRITING

5.1 Introduction

For the need of living cell-based patterning and construct fabrication, numerous cell-based tissue biofabrication technologies have been intensively studied recently. Such technologies include laser guidance direct writing (Odde et al. 2000), modified laser-induced forward transfer (LIFT) (including matrix-assisted pulsed-laser evaporation direct-write (MAPLE DW) (Ringeisen et al. 2004; Lin et al. 2009a) and its modifications (Barron et al. 2004b; Hopp et al. 2005); ink-jetting (Wilson et al. 2003), and electro-hydrodynamic jetting (Jayasinghe et al. 2006).

During any of above tissue biofabrication processes, which may use biological materials to fabricate cell and/or biomaterial-based products, there might be excessive thermal and/or mechanical stresses introduced to biological materials including living cells. If this process-induced stress exceeds the adaptive capacity of a cell, irreversible injury may occur, leading to unexpected apoptosis. Cell injury/damage can be simply classified as thermal and/or mechanical cell injury and biochemical injury (Mardikar et al. 2000). Generally, cell injury is reversible up to a certain point; however, exposure of a cell to a high magnitude and/or lasting external stress may cause irreversible cell injury even cell death. Indeed, cell death due to process-induced cell injury is common in biofabrication processes (Ringeisen et al. 2004; Ringeisen et al. 2006; Chang et al. 2008;

Lin et al. 2009a; Lin et al. 2010a; Lin et al. 2010b), and the post-transfer cell viability is a key index to evaluate the feasibility and efficiency of a biofabrication technique.

Some studies (Ringeisen et al. 2004; Ringeisen et al. 2006; Chang et al. 2008; Lin et al. 2009a; Lin et al. 2010a; Lin et al. 2010b) have been conducted to investigate biofabrication process-induced cell injury. For example, for MAPLE DW-based cell direct writing, there have been many interesting contributions, which include the experimental work on the effect of matrigel coating thickness of the receiving substrate on the post-transfer mammalian cell viability (Ringeisen et al. 2004) and the effect of laser fluence (laser pulse energy / area of laser spot size) on the post-transfer yeast cell viability (Lin et al. 2009a) and colon cell viability (Lin et al. 2010a; Lin et al. 2010b) as well as some modeling attempts regarding the MAPLE DW process-induced mechanical stress profile during bubble expansion and cell droplet landing (Wang et al. 2008; Wang et al. 2009a).

Thus far, there is no available systematic study to understand and model cell damage using a combined biological and engineering approach. As so, many available cell damage models (Blackshear et al. 1965; Born et al. 1992; Sundaram et al. 2003; Breuls et al. 2003b; Grigioni et al. 2005) have helped to estimate the cell damage degree but failed to capture the biophysics behind the process-induced cell damage mechanisms. The objective of this study is to propose a new mathematical approach to biophysically predict the biofabrication-induced cell damage based on the triggered molecular signaling pathway in the cellular network. The key contribution is to elucidate and model how an external stress signal leads to cell death through a dynamic process. More importantly, the proposed methodology provides a biophysics-based approach to investigate cell

damage under influences of a variety of mechanical, chemical and biological environments by considering specific molecular networks in a cell.

Among various biofabrication technologies, MAPLE DW, a non-contact laser-based direct-write technique, has emerged as one of the most promising surface deposition and additive manufacturing techniques because of its flexibility and applicability to disparate material systems. As shown in Fig. 1.1, a typical MAPLE DW setup includes three basic components: an ultraviolet (UV) pulsed laser source and beam delivery optics; a laser transparent quartz disk coated with materials to be transferred, known as a ribbon; and a computer-controlled receiving substrate for the transferred material. Due to its flexibility and applicability in biofabrication, this modeling study also uses MAPLE DW as a representative process to predict the post-transfer cell viability. It should be noted that the proposed methodology is also applicable to other biofabrication processes.

5.2 Background

The effects of different process-induced external loadings on biological materials, ranging from macromolecules to tissues, have been extensively investigated. Such loadings include laser-generated stress wave (Lee et al. 1997), ultrasound-induced shock wave (Sundaram et al. 2003), high pressure (Yamaguchi et al. 2008), UV irradiation (Kulms et al. 1999), and shear stress (Tzima et al. 2005; Fitzgerald et al. 2008). As recognized, cells may be injured as a result of the mechanical and irradiation stimuli, and the damage degree depends on different factors, such as heat shock (Rylander et al. 2005), mechanical stress (Bilek et al. 2003; Ringeisen et al. 2004; Wang et al. 2008), UV

radiation (Scoltock et al. 2004), and loading duration (Leverett et al. 1972), to name a few. As in MAPLE DW, UV radiation may damage cell DNA and further triggers cell apoptosis through mitochondrial cytochrome c release; during the cell landing process, the impact-induced deceleration and large mechanical stress (Ringeisen et al. 2004; Wang et al. 2008) may also trigger cell apoptosis through cell death receptor and/or intracellular DNA damage; and during the cell droplet formation and ejection process, the laser-induced bubble expansion process may also introduce a large acceleration and stress wave to cells (Wang et al. 2009a; Wang et al. 2009b).

Process dependent cell damage or cell viability has also been studied and modeled using various approaches. Born et al. (Born et al. 1992) modeled cell damage based on the duration-independent laminar shear stress-induced cell membrane tension. Sundaram et al. (Sundaram et al. 2003) used the area strain to determine the cell membrane disruption status and cell viability in the presence of ultrasound-induced shock wave or bubble wall motion. Fife et al. (Fife et al. 2006) applied the logistic and Gompertz models to estimate the damage percentage of a biological pesticide using the energy dissipation rate of the complex flow as a damage index. While the above approaches have modeled cell damage as duration independent, some other studies have also considered the effect of loading duration on cell damage. The power law was applied to study red blood cell damage by considering both the shear stress and exposure duration effects (Blackshear et al. 1965; Grigioni et al. 2005). A strain energy density-based cumulative damage law also included the time accumulative effect on cell damage (Breuls et al. 2003b).

However, biological materials such as living cells are much more complex than any other engineering materials in terms of their failure criteria. Good understanding of

cell damage should be developed based on biological damage pathways involved in the cell damage process instead of purely using some engineering criteria such as von Mises stresses and strain energies. Fortunately, knowledge of the complex network of interacting genes and proteins makes it necessary to study the dynamic feature of the cell injury based on the molecular signaling pathways (Hengartner 2000; Zhang et al. 2009). It has been found that the mechanical signal may induce the regulation of pathways through transforming itself into a biological signal, leading to the activation of effector caspases, which are cysteine proteases with specificity for aspartic acid residue (Apenberg et al. 2003; Sahoo et al. 2006; Yamaguchi et al. 2008). Caspase-dependent cell death is usually represented by apoptosis in an all-or-none (live or dead) manner (Albeck et al. 2008) and characterized by cell shrinkage, condensation of nuclei, loss of microvilli, etc (Yamaguchi et al. 2008). That is, once a cell reaches a critical status under external loadings, it commits to undergo apoptosis, which is initiated and executed by caspases (Albeck et al. 2008; Zhang et al. 2009), which are present in normal cells in inactive forms called procaspases. In response to appropriate stress signals, procaspases are cleaved to active forms and proceed to disassemble the cell from inside through the intrinsic and extrinsic pathways (Hengartner 2000; Rice et al. 2003; Eissing et al. 2004; Zhang et al. 2009). In addition to degrading cellular proteins, caspases activate DNases that destroy the cell's genome.

Among different cell damage-related effector caspases, caspase 3 is the most important one and has obtained intensive attention in the study of shear stress-induced neutrophil apoptosis (Shive et al. 2002), shear stress-induced vascular smooth muscle cell (VSMC) apoptosis via an autocrine Fas/FasL pathway in addition to the mitochondria-

associated pathway (Apenberg et al. 2003), shear stress-dependent cell death in *Bacillus subtilis* (Sahoo et al. 2006), pressure-induced apoptosis of murine erythroleukemia (MEL) cells through both intrinsic and extrinsic pathways (Yamaguchi et al. 2008), and laminar shear stress-stimulated VSMC apoptosis via the intrinsic pathway (Fitzgerald et al. 2008), to name a few. While the molecular signaling pathways have been intensively investigated in understanding cell damage (Apenberg et al. 2003; Eissing et al. 2004; Tzima et al. 2005; Legewie et al. 2006; Zhang et al. 2009), mathematical understanding and modeling of cell damage based on the molecular signaling pathways is still not explored. Such a mathematical understanding may have great application potential for development and optimization of tissue biofabrication processes. Such a modeling approach should include the effect of the external stresses such as mechanical stresses in MAPLE DW and/or biochemical stimuli.

5.3 Molecular Signaling Pathway-Based Cell Damage Modeling

Cells usually trigger apoptosis through two pathways: intrinsic pathway and extrinsic pathway. Both pathways can be triggered either separately (Zhang et al. 2009; Eissing et al. 2004) or independently in an additive manner (Kulms et al. 1999). The intrinsic pathway, also referred as stress-induced caspase activation (Fussenegger et al. 2000), responds to intracellular stresses (hypoxia, DNA damage, etc.) by activating BH3 proteins and finally the downstream effector caspase, caspase 3. The extrinsic pathway, also referred as receptor-mediated caspase activation (Fussenegger et al. 2000), responds to extracellular death ligands by activating caspases 8 and 10, which in turn activate executioner caspases 3, 6, and 7 (Albeck et al. 2008).

Since external mechanical stresses may induce cell death via either the intrinsic pathway or the extrinsic pathway (Hengartner 2000; Fitzgerald et al. 2008), both the intrinsic and extrinsic pathways are analyzed and modeled to capture the cell damage degree in the following sections. Previous studies have found that there is a distinct time lag before caspase 3 is activated in response to stress signals (Eissing et al. 2004; Zhang et al. 2009). As a stress increases, the time lag decreases. The cell damage model proposed herein mathematically captures the duration effect on cell death in addition to the stress magnitude effect. In laser-assisted cell direct writing such as MAPLE DW, the bubble expansion-induced cell droplet formation and subsequent cell droplet landing-induced impact processes may introduce severe mechanical stresses, such as shear and normal stresses, to cells being transferred. During these processes, the resulting mechanical stress may induce cell apoptosis, leading to cell death (Apenberg et al. 2003; Fitzgerald et al. 2008; Yamaguchi et al. 2008) as summarized in Fig. 5.1. Definitions or explanations of some molecules involved in the both pathways can be found in Appendix A.

To capture the cell death-related events in biofabrication, while a general cell damage modeling methodology is proposed to be flexible for any cell types and experimental circumstances, some general assumptions are made as follows. First, the external stress cannot be too high to make the cell membrane permeable or broken; second, cells may be killed by other causes, such as inflammation (Rock 2008) and infection (O'Sullivan et al. 2007), in addition to the caspase-dependent signaling pathway. However, these other causes are not considered in this study; third, cells can also enhance their viability by triggering heat shock proteins (HSPs) induced by stimuli

from environmental stresses such as ischemia, hypoxia, heavy metals, free oxygen radicals, and elevated temperature (Rylander et al. 2005), which are not of interest here either; fourth, some cells have been observed to be able to recover from some biofabrication-induced damage (Lin et al. 2009a; Lin et al. 2010a), and this possible reversible cell injury is not considered here. Once apoptosis is triggered, cells should commit to finishing the whole process (Zhang et al. 2009).

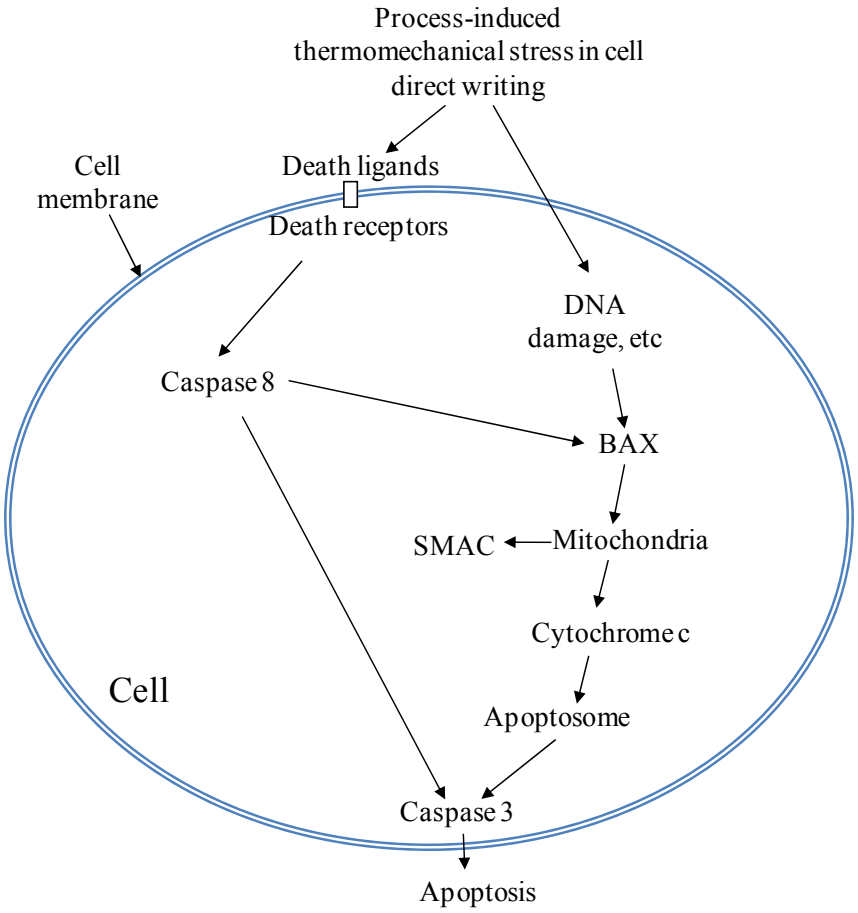

Figure 5.1: Schematic representation of process-induced cell apoptosis in biofabrication

5.3.1 Modeling of Damage Lag Time in the Intrinsic Pathway

5.3.1.1 Intrinsic Pathway Introduction

The working mechanism of the intrinsic pathway model is assumed as follows (Zhang et al. 2009). BH3 proteins, which possess only one BCL2-homology structural domain, are considered as a general class of proapoptotic proteins which activate BAX and a mechanical stress signal triggers the production of active BH3 proteins. The production and elevation of BH3 proteins promotes the activation of the proapoptotic proteins, BAX, by causing conformational changes of BAX. Activated BAX translocates to the mitochondrial membrane by forming oligomers in the mitochondrial outer membrane, resulting in the release of cytochrome c (CytoC) and the second-mitochondria-driven activator of caspase (SMAC) to the cytoplasm from the mitochondrial intermembrane space. In the cytoplasm, cytochrome c binds to APAF-1 to form an apoptosome, which activates caspase 9 and the downstream effector caspase, caspase 3, causing cell apoptosis.

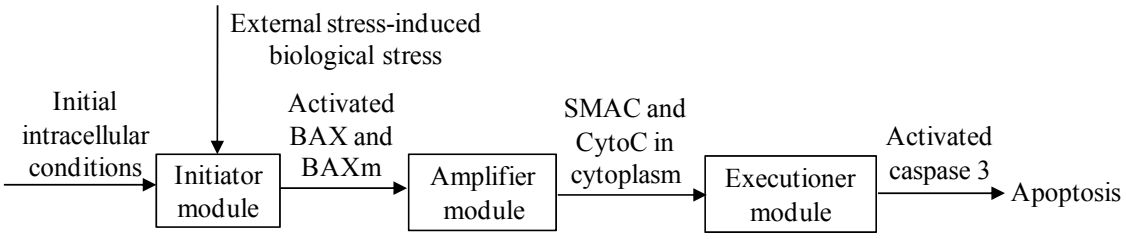

Figure 5.2: Intrinsic pathway flowchart

Three modules have been used to illustrate the intrinsic pathway (Zhang et al. 2009), which is summarized in Fig. 5.2. The initiator module describes the mitochondrial BAX generation due to a stress signal. The amplifier module describes how the

membrane-localized form of BAX (BAXm) causes the release of cytochrome c and SMAC, and the executioner module describes how cytochrome c and SMAC cooperate to activate caspase 3. The molecule components in the intrinsic pathway model and the system equations (Zhang et al. 2009) are listed in Appendix A and B, and the three modules are briefly described as follows.

The initiator module describes BAX activation by BH3 proteins. When a stress signal is applied, the amount of BH3 increases. The BH3 molecules are initially inactivated by binding to inhibitory proteins (BCL2). Due to the stress signal, free BH3 accumulates and activates BAX by altering its conformation. The activated BAX moves to the mitochondrial outer membrane, forming BAXm (Desagher et al. 1999; Eskes et al. 2000). BAXm can also bind to BCL2, releasing additional free BH3 to facilitate the conversion of BAX to BAXm. As a result, in the initiator module, BAXm proteins are produced due to the stress signals.

The amplifier module describes BAXm-induced release of cytochrome c and SMAC. When BAXm proteins are produced in the initiator module, they may form oligomers that increase the permeability of the mitochondrial membrane (Albeck et al. 2008). As a result, the formed tetramers open the channels in the mitochondrial outer membrane to allow many proteins, including cytochrome c and SMAC, to release into the cytoplasm.

The executioner module describes caspase activation by cytochrome c and SMAC. Once the cytochrome c and SMAC are released into the cytoplasm in the amplifier module, they further cooperate to activate caspase 3. The cytochrome c first binds to Apaf-1 to form an active apoptosome. The apoptosome activates caspase 9 and

further activates caspase 3. Active caspase 3 may be inhibited by X-linked inhibitor of apoptosis protein (XIAP), which blocks the activity of caspase 3 by binding to its active site (Zhang et al. 2009). However, this inhibition can be overcome by the release of SMAC from mitochondria.

5.3.1.2 Time Lag and Damage Function in the Intrinsic Pathway

The intrinsic pathway can be described by four ordinary differential equations (ODEs) for the initiator module, five ODEs for the amplifier module and eight ODEs for the executioner module (Zhang et al. 2009) as shown in Appendix B. Among them, the initiator module was found to be responsible for the time-delay properties of apoptosis (Zhang et al. 2009) as follows:

$$\frac{d[BH3]_F}{dt} = k'_{sBH3} + k''_{sBH3} \times stress - k_{dBH3} \times [BH3]_F - k_{asBH3BCL2} \times [BH3]_F \times [BCL2]_F + k_{dsBH3BCL2} \times [BH3/BCL2] \tag{5.1}$$

$$\frac{d[BH3/BCL2]}{dt} = k_{asBH3BCL2} \times [BH3]_F \times [BCL2]_F - k_{dsBH3BCL2} \times [BH3/BCL2] - k_{dBH3} \times [BH3/BCL2] \tag{5.2}$$

where t is the time, k'_{sBH3}, k''_{sBH3}, $k_{asBH3BCL2}$, $k_{dsBH3BCL2}$ and k_{dBH3} are the coefficient parameters in the system equations as defined in (Zhang et al. 2009), $[BH3]_F$ is the concentration of free $BH3$, $[BH3/BCL2]$ is the concentration of $BH3$ which binds to $BCL2$, and $[BCL2]_F$ is the concentration of free $BCL2$. Since $[BH3] = [BH3]_F + [BH3/BCL2]$, adding Eqs. (5.1) and (5.2) leads to:

$$\frac{d[BH3]}{dt} = (k'_{sBH3} + k''_{sBH3} \times stress) - k_{dBH3} \times [BH3] \tag{5.3}$$

By dividing k_{dBH3} on the both sides, and denoting the final concentration at a given biological stress state $[BH3]_s$ as $\frac{k'_{sBH3} + k''_{sBH3} \times stress}{k_{dBH3}}$, Eq. (5.3) can be written as follows:

$$\frac{1}{k_{dBH3}} \frac{d([BH3]-[BH3]_s)}{([BH3]_s-[BH3])} = dt \tag{5.4}$$

By integrating the left side of Eq. (5.4) from the initial concentration at the resting state ($[BH3]_0$) to the threshold concentration ($[BH3]_c$) and the right side from 0 to the time lag subject to $[BH3]_s$ (T_L), T_L can be obtained as follows:

$$T_L = \frac{1}{k_{dBH3}} \ln\left(\frac{[BH3]_s-[BH3]_0}{[BH3]_s-[BH3]_c}\right) \tag{5.5}$$

At T_L, caspase 3 begins to increase significantly. The state of a cell at a given stress state can be defined as (Zhang et al. 2009):

$$Cell\ state = \begin{cases} alive, & T < T_L \\ dead, & T \geq T_L \end{cases} \tag{5.6}$$

where T is the time duration of the cell exposure to a stress.

If the time duration that the cell experiences exceeds the time lag for a given stress level, the cell commits to death (Zhang et al. 2009). In contrast, if the stress is removed before the time lag is reached, the cell is still alive without any injury. Here the cell damage degree is modeled as all-or-none for simplicity. Figure 5.3 shows a critical line in the two-dimensional (2D) phase space defined by any given stress level and the corresponding time lag, T_L. This critical line divides the whole space into a living zone

(for living cells) and a damage zone (for dead cells) for any given stress and stress duration pair.

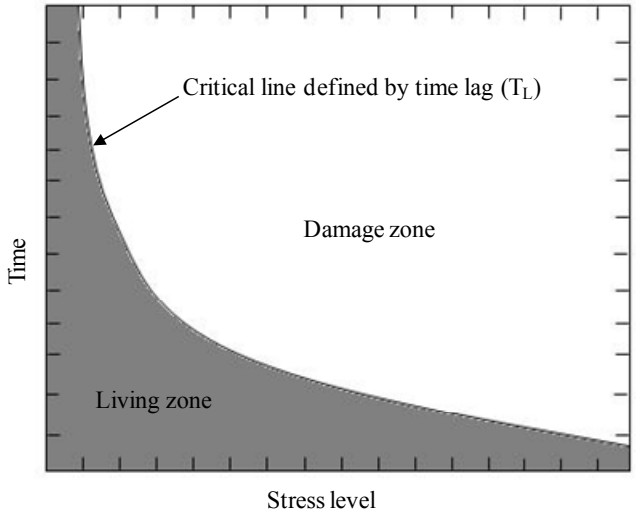

Figure 5.3: Phase diagram of cell damage zones where the stress is proportional to $[BH3]_s$ and the grey area is the cell living zone

To characterize the cell damage degree, a damage function F_I can be built to quantify cell damage. At the initial state $t = 0$, $F_I = 0$. The exposure to the stress leads to the increase of the damage function, and the cell is damaged and killed when $F_I = 1$ at time $t = T_L$ for a given stress level. Under a constant $[BH3]_s$ level, the time lag for cell damage can be determined using Eq. (5.5). If damage occurs at a constant rate, the rate of damage is as follows:

$$\frac{dF_I}{dt} = \frac{1}{T_L} = \frac{k_{dBH3}}{\ln\left(\frac{[BH3]_s - [BH3]_0}{[BH3]_s - [BH3]_c}\right)} \tag{5.7}$$

Using the initial condition, the damage function for constant stress can be obtained as:

$$F_I = \frac{k_{dBH3}}{\ln\left(\frac{[BH3]_s - [BH3]_0}{[BH3]_s - [BH3]_c}\right)} t \tag{5.8}$$

Obviously, at the time lag T_L, $F_I = 1$, which indicates the cell is dead. If $F_I \geq 1$, the cell is dead; otherwise, if $F_I < 1$, the cell is alive.

For the given system of 17 equations, initial conditions and coefficient parameters (Zhang et al. 2009) as shown in Appendix A, the ODEs can be solved numerically using COMSOL 3.5a. Since the activated caspase 3 is the effector caspase, the variation of the activated caspase 3 is of interest herein. For a 0.5 stress threshold value (Zhang et al. 2009), the stress range was chosen as [0.6, 2.6] with an increment of 0.1. For each stress level, the time evolution of caspase 3 was numerically solved from the system of ODEs. Under different stress signal strengths, which determine the final concentration of BH3, the variations of the activated caspase 3 are shown in Fig. 5.4. Here the time lag was defined at the moment at which the activated caspase 3 concentration began to rise significantly and reached 2 percent of its corresponding peak value. As the input signal strength increases, the time lag decreases. The bold line in Fig. 5.4 depicts the variation of time lag with respect to the input signal strength. For any given stress level, caspase 3 activity remains low for a certain time starting from the beginning state; then a steep rise in caspase 3 concentration occurs right after the time lag if the input signal exceeds the threshold value, $[BH3]_c$. It should be noted that neither the amplitude nor the duration of caspase 3 activity is sensitive to the level of stress above the $[BH3]_c$ threshold.

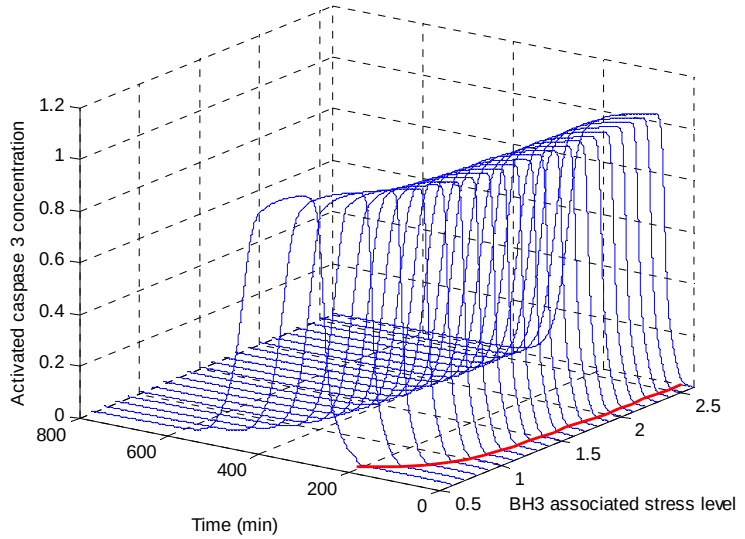

Figure 5.4: Activated caspase 3 level as a function of time and stress level

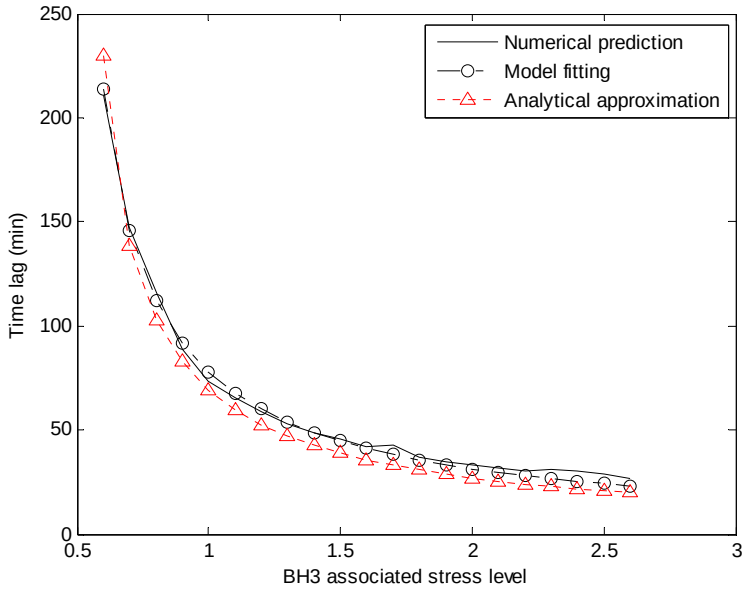

Figure 5.5: Variation of time lag for different stress levels

The numerical predictions from Fig. 5.4 are compared with those computed using Eq. (5.5), and the comparison is shown in Fig. 5.5. The numerical predictions were further fitted using a logarithmic function to better compare the modeling performance with that of Eq. (5.5) since Eq. (5.5) is also a logarithmic function. It can be seen that there is a good agreement between the numerical simulation and the analytical approximation, showing the validity of Eq. (5.5) as a good analytical approximation.

5.3.2 Modeling of Cell Lag Time in the Extrinsic Pathway

5.3.2.1 Extrinsic Pathway Introduction

As aforementioned, extrinsic pathway signaling is mediated by the activation of death receptors, which includes Fas (CD95) or the members of tumor necrosis factor receptor (TNF-R) superfamily. Binding of death ligands and their death receptors usually induce the oligomerization of the associated death receptors, followed by recruitment of adaptor proteins Fas-associated death domain proteins (FADD) to the cytoplasmic portions of the receptor (Bagci et al. 2006). FADD then recruits procaspase 8, resulting in the formation of death-inducing signaling complex (DISC) and ultimately provokes caspase 8 activation.

Two types of cells have been recognized in the extrinsic pathway based on their sensitivity to Fas-induced apoptosis (Jost et al. 2009). For type I cells, such as lymphocytes and thymocytes (Jost et al. 2009), the death-inducing signaling complex is easily formed. At the beginning, the death-inducing signaling complex forms at the membrane after death receptor stimulation activates caspases 8. Procaspase 3 is cleaved and activated by activated caspase 8. Activated caspase 3 acts in terms of a positive feedback loop onto procaspase 8. Activated caspase 3 can be inhibited by XIAP. The

cleavage products of XIAP have been described to have minor effects on caspase 3, so it can be neglected (Deveraux et al. 1999). The molecule BAR is introduced to bind to activated caspase 8 with an affinity similar to XIAP binding to caspase 3 (Eissing et al. 2004). The activated effector caspase, caspase 3, ultimately results in cell apoptosis. This direct and main caspase-dependent apoptosis pathway usually occurs when the amount of activation of caspase 8 is large.

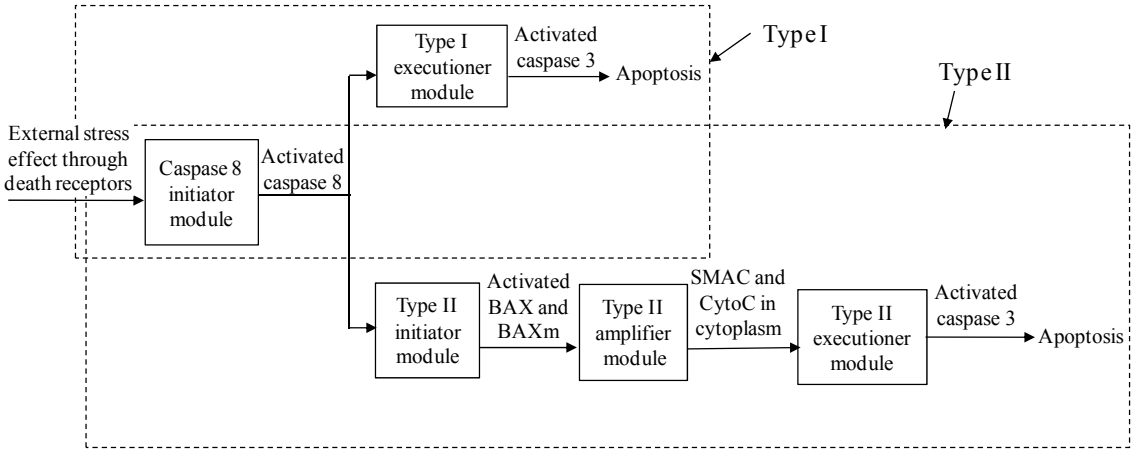

Figure 5.6: Extrinsic pathway flowchart

On the other side, small amount of caspase 8 requires signaling amplification via the mitochondria-dependent apoptosis for type II cells (Bagci et al. 2006) such as hepatocytes and pancreatic β cells (Jost et al. 2009). This process is usually initiated by the cleavage of Bid. The truncated BID (tBid) translocates to the mitochondria, where it acts with the Bcl-2 family members BAX and BAK. Cytochrome c and SMAC are then released to the cytoplasm. Cytochrome c can bind to Apaf-1 to activate caspase 9 molecules, which in turn activate caspase 3, ultimately resulting in cell death. The extrinsic pathway signaling for both cell types is shown in Fig. 5.6.

The behavior of type I cell has been mainly modeled in this study since it is the main extrinsic pathway route when cells are subject to external process-induced stresses, especially when the death-inducing signaling complex (DISC) formation is strong (Scaffidi et al. 1998).

5.3.2.2 Time Lag and Damage Function in the Extrinsic Pathway

The system equations in the type I cell extrinsic pathway include the following eight ODEs (Eissing et al. 2004) to describe the basic reactions. This model is able to describe key characteristics like a fast execution phase and bistability and contains several assumptions (Eissing et al. 2004): 1) several types of initiator and effector caspases are combined in one species and the same applies to several types of inhibitors of the effector caspases; 2) the external stimuli are not explicitly included in the model. The initial amount of activated initiator caspase 8 resulting from the stimulation is considered as an input in the model; and 3) other effector caspases such as caspase 6 are neglected in this model.

$$\frac{d[\mathrm{Pro}C8]}{dt} = -k_2 \times [C3] \times [\mathrm{Pro}C8] - k_9 \times [\mathrm{Pro}C8] + k_{-9} \tag{5.9}$$

$$\frac{d[C8]}{dt} = k_2 \times [C3] \times [\mathrm{Pro}C8] - k_5 \times [C8] - k_{11} \times [C8] \times [BAR] + k_{-11} \times [C8/BAR] \tag{5.10}$$

$$\frac{d[\mathrm{Pro}C3]}{dt} = -k_1 \times [C8] \times [\mathrm{Pro}C3] - k_{10} \times [\mathrm{Pro}C3] + k_{-10} \tag{5.11}$$

$$\frac{d[C3]}{dt} = k_1 \times [C8] \times [\mathrm{Pro}C3] - k_3 \times [C3] \times [XIAP] + k_{-3} \times [C3/XIAP] - k_6 \times [C3] \tag{5.12}$$

$$\begin{aligned} \frac{d[XIAP]}{dt} &= -k_3 \times [C3] \times [XIAP] + k_{-3} \times [C3/XIAP] \\ &- k_4 \times [C3] \times [XIAP] - k_8 \times [XIAP] + k_{-8} \end{aligned} \tag{5.13}$$

$$\frac{d[C3/XIAP]}{dt} = k_3 \times [C3] \times [XIAP] - k_{-3}[C3/XIAP] - k_7[C3/XIAP] \quad (5.14)$$

$$\frac{d[BAR]}{dt} = -k_{11} \times [C8] \times [BAR] + k_{-11} \times [C8/BAR] - k_{12} \times [BAR] + k_{-12} \quad (5.15)$$

$$\frac{d[C8/BAR]}{dt} = k_{11} \times [C8] \times [BAR] - k_{-11} \times [C8/BAR] - k_{13} \times [C8/BAR] \quad (5.16)$$

where $[\mathrm{Pro}C8]$, $[C8]$, $[\mathrm{Pro}C3]$, $[C3]$, $[BAR]$, $[C8/BAR]$, $[XIAP]$, and $[C3/XIAP]$ are the concentrations of procaspase 8, activated caspase 8, procaspase 3, activated caspase 3, BAR, dimer C8/BAR, XIAP, and dimer C3/XIAP, respectively, where the molecule concentration is given in terms of molecules per cell, and Table 5.1 (Eissing et al. 2004) lists all the coefficients for typical simulations.

Some related initial conditions for a HeLa cell (Eissing et al. 2004) are also listed as follows: the average concentrations of caspase 8 and caspase 3 in an unstimulated HeLa cell were quantified to be 130,000 and 21,000 molecules/cell, respectively; the average concentration of XIAP was estimated to be 40,000 molecules/cell; the concentration of BAR was assumed to be 40,000 molecules/cell; and the other molecules were considered not to be present in the absence of a stimulus.

Table 5.1: Coefficient parameter values in the extrinsic pathway model

	Values	Unit		Values	Unit
k_1	5.8×10^{-5}	Cell·min^{-1} mol^{-1}	k_{-1}	0	
k_2	10^{-5}	Cell·min^{-1} mol^{-1}	k_{-2}	0	
k_3	5×10^{-4}	Cell·min^{-1} mol^{-1}	k_{-3}	0.21	min^{-1}
k_4	3×10^{-4}	Cell·min^{-1} mol^{-1}	k_{-4}	0	

k_5	5.8×10^{-3}	min^{-1}	k_{-5}	0	
k_6	5.8×10^{-3}	min^{-1}	k_{-6}	0	
k_7	1.73×10^{-2}	min^{-1}	k_{-7}	0	
k_8	1.16×10^{-2}	min^{-1}	k_{-8}	464	$Cell\cdot min^{-1}\ mol^{-1}$
k_9	3.9×10^{-3}	min^{-1}	k_{-9}	507	$Cell\cdot min^{-1}\ mol^{-1}$
k_{10}	3.9×10^{-3}	min^{-1}	k_{-10}	81.9	$Cell\cdot min^{-1}\ mol^{-1}$
k_{11}	5×10^{-4}	$Cell\cdot min^{-1}\ mol^{-1}$	k_{-11}	0.21	min^{-1}
k_{12}	10^{-3}	min^{-1}	k_{-12}	40	$Cell\cdot min^{-1}\ mol^{-1}$
k_{13}	1.16×10^{-2}	min^{-1}	k_{-13}	0	

Eqs. (5.9-5.16) were solved numerically using COMSOL 3.5a. The initial activated caspase 8 concentration range was taken from [600, 3000] molecules/cell with an increment of 100 molecules/cell. For each stress level, the time evolution of caspase 3 was numerically solved from the system of ODE equations. The caspase 3 concentration is numerically found increasing sharply at a certain moment, so the time lag is determined as the moment at which the activated caspase 3 concentration reaches its peak value. There is a steep rise in caspase 3 concentration after the time lag if the input signal exceeds the threshold value (~75 molecules of caspase 8 per cell (Eissing et al. 2004)). The simulation results under different signal strengths are shown in Fig. 5.7 and the bold line in Fig. 5.7 depicts the variation of time lag with respect to the input signal strength. It

can be seen that the amplitude of the caspase 3 activity is not sensitive to the signal strength and increasing the input signal strength shortens the time lag.

The numerically predicted time lags have been further fitted using a logarithmic function as shown in Fig. 5.8, and the line with circles is a fitting of the numerical predictions. It can be seen that this logarithmic function can capture this time lag and concentration relationship very satisfactorily. Since there is no closed-form analytical approximation available to describe the relationship between the time lag and the activated caspase 8 concentration, a logarithmic relationship as in the intrinsic pathway is proposed to capture this relationship:

$$T_L = \frac{1}{k_{c8}} \ln\left(\frac{[C8]_s - [C8]_0}{[C8]_s - [C8]_c}\right) \tag{5.17}$$

where k_{c8} is the coefficient parameter which can be determined from the numerical solution, $[C8]_s$ is the initial activated C8 concentration at a given stress state, $[C8]_0$ is the initial concentration of C8 at the resting state, and $[C8]_c$ is the threshold concentration of C8. The comparison shown in Fig. 5.8 demonstrates that Eq. (5.17) is a good prediction of the time lag as a function of $[C8]_s$.

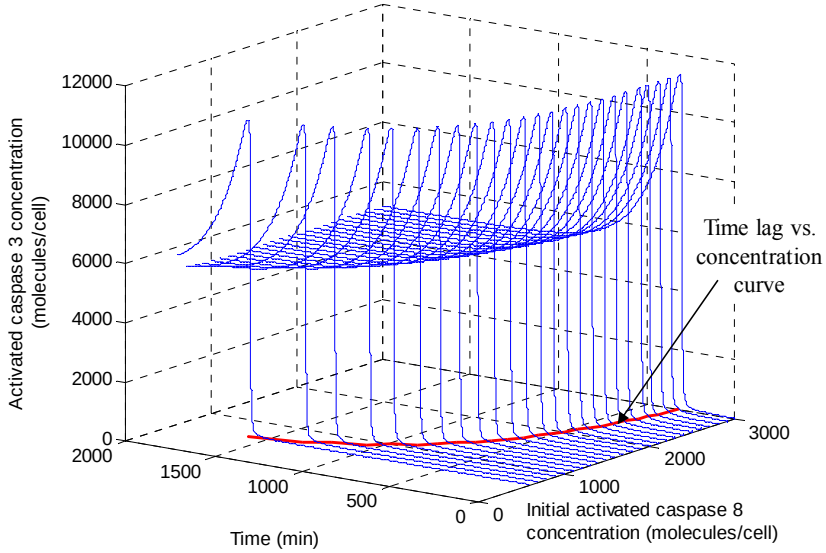

Figure 5.7: Activated caspase 3 level as a function of time and initial activated caspase 8 concentration

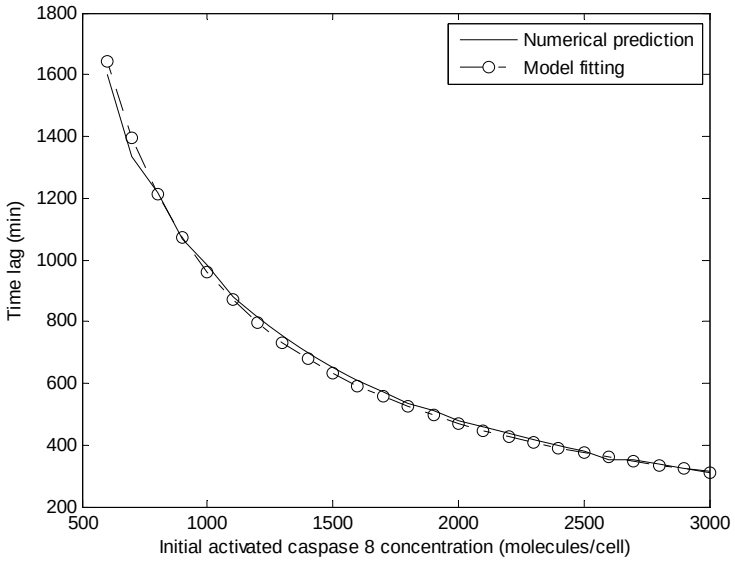

Figure 5.8: Variation of time lag with different inputs (initial activated caspase 8 concentration)

Similar to Eq. (5.8), a damage function F_E for the extrinsic pathway under a given constant stress state is proposed as follows:

$$F_E = \frac{k_{c8}}{\ln\left(\frac{[C8]_s - [C8]_0}{[C8]_s - [C8]_c}\right)} t \tag{5.18}$$

Obviously, at the time lag T_L, $F_E = 1$, which indicates the cell is dead. If $F_E \geq 1$, the cell is dead; otherwise, if $F_E < 1$, the cell is alive.

5.3.3 General Cell Damage Function

While some additive effects of both signaling pathways have been reported (Kulms et al. 1999), most cell apoptosis is initiated and executed by either the intrinsic pathway or the extrinsic pathway (Hengartner 2000). For either pathway, the damage function F can be written in a general cell damage form:

$$F(C, t^*) = \frac{k^* t^*}{\ln\left(\frac{C - C_0}{C - C_c}\right)} \tag{5.19}$$

where C is $[BH3]_s$ in the intrinsic pathway model or $[C8]_s$ in the extrinsic pathway model due to the activation of the external stress, $k^* = T_{L0}\hat{k}$ is a dimensionless number where T_{L0} is the time lag for given $[BH3]_s$ or $[C8]_s$ and $\hat{k}$ represents k_{dBH3} in the intrinsic pathway model or k_{c8} in the extrinsic pathway model, C_0 and C_c define the concentration values at the resting state and the threshold, respectively, and $t^* = t / T_{L0}$ is a dimensionless time.

If both the intrinsic pathway and extrinsic pathway are triggered in cell apoptosis, they usually activate caspase 3 independently (Kulms et al. 1999). In this study, it is

assumed that if one of the two pathways first leads to cell apoptosis, the effect of the other pathway is limited and will not be further analyzed. Therefore, only the pathway which leads to cell apoptosis is considered. Under this assumption, Eq. (5.19) is still applicable in generalizing the analysis procedure. Actually, the cross-talk of these two pathways is minimal under most conditions (Hengartner 2000). If either the intrinsic pathway or extrinsic pathway plays a role in cell death, Eq. (5.19) is the general form of the cell damage function.

If damage occurs at a constant rate, this rate can be determined using Eq. (5.19):

$$\frac{dF(C,t')}{dt'} = \frac{k^*}{\ln\left(\frac{C-C_0}{C-C_c}\right)} \tag{5.20}$$

where t' is the time ($t' \in [0 \quad t^*]$).

For a time-dependent stress history, the linear cumulative damage model, defined as Miner's law, is usually applied to consider the damage accumulation effect (Carter et al. 1985; Christensen 2002). The underlying hypothesis is that the damage degree during each time interval can be added as follows:

$$\sum_{i=1}^{M} \frac{\Delta t_i' k^*}{\ln\left(\frac{C(t_i')-C_0}{C(t_i')-C_c}\right)} = 1 \tag{5.21}$$

where M is the number of time steps before the time lag is reached, i ($i \in [1, \mathrm{M}]$) represent the ith step, $\Delta t_i'$ is the duration of the ith step, and $C(t_i')$ is the concentration at the moment t_i'.

The cumulative damage function $F'(C(t'),t^*)$ for the time duration ($[0,t^*]$) can be determined as follows:

$$F'(C(t'),t^*) = \int_0^{t^*} \frac{k^*}{\ln\left(\frac{C(t')-C_0}{C(t')-C_c}\right)} dt' \tag{5.22}$$

If the damage function $F'(C(t'),t^*)=1$, the corresponding time t^* defines the time lag for a given time-dependent stress history.

In fact, when a time-dependent stress history is applied, the time lag defined by Eq. (5.5) is not valid any more. Generally, *stress* in Eq. (5.5) is a function of time *t* as defined as follows:

$$stress = k'_1 + k'_2 f(t) \tag{5.23}$$

where k'_1 and k'_2 are the coefficients, and $f(t)$ is any time-dependent stress history function. Substituting Eq. (5.23) in Eq. (5.3), it becomes

$$\frac{d[BH3]}{dt} = k''_1 + k''_2 f(t) - k[BH3] \tag{5.24}$$

where $k''_1 = k'_{sBH3} + k''_{sBH3} \times k'_1$, $k''_2 = k''_{sBH3} k'_2$, and $k = k_{dBH3}$. Taking the Laplace transform of both sides of Eq. (5.24), it leads to:

$$s\overline{[BH3]} - [BH3]_0 + k\overline{[BH3]} = \frac{k''_1}{s} + k''_2 \overline{f(s)} \tag{5.25}$$

where the bar symbol "$\overline{\ }$" denotes the Laplace transform, and s denotes the variable in the Laplace transform. Eq. (5.25) can be further organized and solved for $\overline{[BH3]}$:

$$\overline{[BH3]} = \frac{[BH3]_0}{(s+k)} + \frac{k''_1}{s(s+k)} + \frac{k''_2 \overline{f(s)}}{s+k} \tag{5.26}$$

The inverse Laplace transform of $\overline{[BH3]}$ reads

$$[BH3] = \left([BH3]_0 - \frac{k_1^{"}}{k} \right) \exp(-kt) + \frac{k_1^{"}}{k} + k_2^{"} \int_0^t \exp(-k(t-\xi)) f(\xi) d\xi \tag{5.27}$$

At time $t = T_L$,

$$[BH3]_c = \left([BH3]_0 - \frac{k_1^{"}}{k} \right) \exp(-kT_L) + \frac{k_1^{"}}{k} + k_2^{"} \int_0^{T_L} \exp(-k(t-\xi)) f(\xi) d\xi \tag{5.28}$$

Eq. (5.28) gives a general equation to solve for the time lag in the case of any arbitrary time-dependent stress history in the intrinsic pathway. For most cases, it is difficult to solve for T_L from Eq. (5.28) for an arbitrary temporal stress function $f(t)$. Considering a simple case where $stress = k'_1 + k'_2 t$, Eq. (5.28) leads to:

$$\left([BH3]_c - \frac{k_1^{"}}{k} + \frac{k_2^{"}}{k^2} \right) = \left([BH3]_0 - \frac{k_1^{"}}{k} + \frac{k_2^{"}}{k^2} \right) \exp(-kT_L) + \frac{k_2^{"}}{k} T_L \tag{5.29}$$

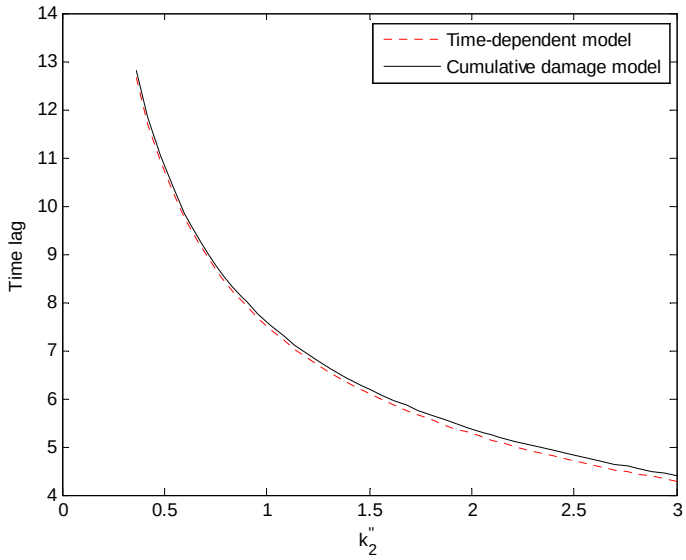

Figure 5.9: Time lag as a function of $k_2^{"}$ using the cumulative damage function and time-dependent model

Figure 5.9 shows the comparison between the time lag predictions given by the cumulative damage function ($F' = 1$ using Eq. (5.22)) and the time-dependent model (Eq. (5.29)) when $k_1'' = 0.1$. Here the coefficient parameters were taken from Appendix A, and the time lag was measured in minutes. The dimensionless BH3 threshold concentration was set as 46 and its initial concentration was 16 (Zhang et al. 2009). It shows that the cumulative model gives satisfactory time lag predictions while a small difference is observed only if the stress changing rate is high, proving that the proposed cumulative damage model works with a satisfactory accuracy.

5.4 External Stress-Induced Cell Damage Model

5.4.1 Cell Damage Model Development

The process-induced external stress including the mechanical stress may activate a signaling pathway (Apenberg et al. 2003; Sahoo et al. 2006; Yamaguchi et al. 2008; Fitzgerald et al. 2008). For example, the laminar shear stress may induce cell damage of the vascular smooth muscle cell via the intrinsic pathway (Fitzgerald et al. 2008). Usually the concentration *C* of the activated BH3 or caspase 8 depends on the mechanical stress, that is,

$$C = g(\tau) \tag{5.30}$$

where τ is the external or mechanical stress, and $g(\tau)$ is a function relating *C* and τ. The relationship between the external or mechanical stress and its resulting biological stress which induces BH3 or caspase 8 is not well understood thus far. For simplicity, it is assumed that the concentration C is proportional to the external or mechanical stress herein. It should be pointed out that if a more complex relationship can be defined for

certain applications, the following proposed cell damage model can be extended to include any different relationship of the external or mechanical stress and the concentration C. By assuming a linear relationship of C and τ, it gets:

$$C = P + Q\tau \tag{5.31}$$

where P is the concentration C at the resting state and Q is the linear coefficient. Substituting Eq. (5.31) into Eq. (5.19) leads to the cell damage degree K as a function of constant stress and time duration as follows:

$$K(\tau, t^*) = \frac{k^* t^*}{\ln\left(\frac{\tau - \tau_0}{\tau - \tau_c}\right)} \tag{5.32}$$

where τ_c and τ_0 is the external or mechanical stress threshold value and the external or mechanical stress at the resting state, respectively. It should be pointed out that if the external or mechanical stress is lower than τ_c, the resulting damage contribution is neglected here.

From Eq. (5.22), the cumulative damage degree $K'(\tau(t'), t^*)$ for time duration ($[0, t^*]$) can be written as follows:

$$K'(\tau(t'), t^*) = \int_0^{t^*} \frac{k^*}{\ln\left(\frac{\tau(t') - \tau_0}{\tau(t') - \tau_c}\right)} dt' \tag{5.33}$$

where t' is the time and $t' \in [0, t^*]$. The cell state P_j of a cell N_j (j=1, 2, …, N, and N is the total number of cells being modeled) is defined based on the $K'(\tau(t'), t^*)$ level by:

$$P_j = \begin{cases} 1 & (\textit{living cell}), \quad K'(\tau(t'), t^*) < 1 \\ 0 & (\textit{damaged / dead cell}), \quad K'(\tau(t'), t^*) \geq 1 \end{cases} \tag{5.34}$$

The cell viability is then further estimated by dividing the number of living cells by the total cell number as follows:

$$\textit{Cell viability} = \frac{\sum_{j=1}^{N} P_j}{N} \tag{5.35}$$

The proposed cell damage model includes Eqs. (5.33) and (5.34), and Fig. 5.10 shows the flowchart for the external stress-induced cell death and the resulting cell viability prediction. The external stress may induce either the intrinsic pathway or extrinsic pathway. The time lag is determined based on the external stress, and the cumulative cell damage degree, $K'(\tau(t'), t^*)$, is calculated using Eq. (5.33). Finally, the cell viability can be estimated for the cell population using Eqs. (5.34) and (5.35).

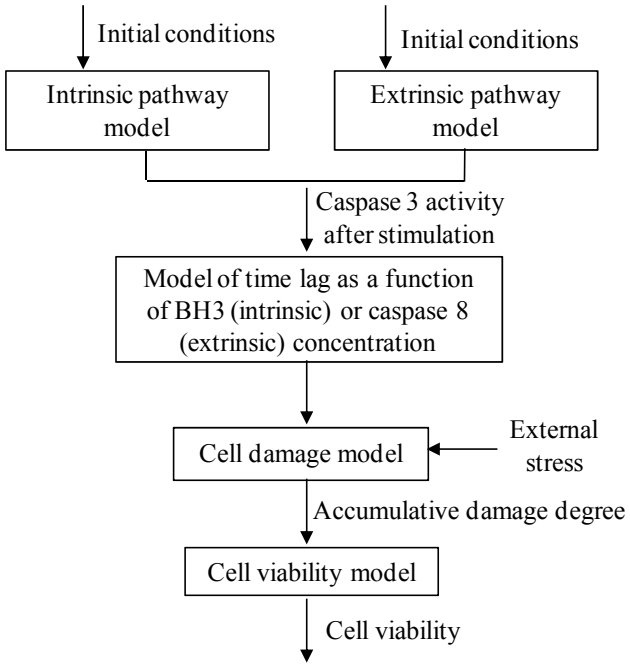

Figure 5.10: Flow chart for cell viability prediction

If the cell damage degree K or the cumulative cell damage degree K' becomes 1, the cell is killed. When $K=1$, the damage initiation time t_D under a constant external or mechanical stress τ is determined as follows using Eq. (5.32):

$$t_D = \frac{1}{k^*}\ln\left(\frac{\tau-\tau_0}{\tau-\tau_c}\right) \tag{5.36}$$

where the time t_D is the damage initiation time corresponding to the external or mechanical stress τ. If $\left|\frac{\tau-\tau_c}{\tau_c-\tau_0}\right| >> 1$, the Taylor expansion of the right-hand side of Eq. (5.36) leads to:

$$\begin{aligned} t_D &= \frac{1}{k^*}\ln\left(\frac{\tau-\tau_0}{\tau-\tau_c}\right) = \frac{1}{k^*}\ln\left(1+\frac{\tau_c-\tau_0}{\tau-\tau_c}\right) \\ &= \frac{1}{k^*}\frac{\tau_c-\tau_0}{\tau-\tau_c} + o\left(\left(\frac{\tau_c-\tau_0}{\tau-\tau_c}\right)^2\right) \end{aligned}, \quad \left|\frac{\tau-\tau_c}{\tau_c-\tau_0}\right| >> 1 \tag{5.37}$$

When the external or mechanical stress level is much higher than the threshold stress, the damage initiation time can be approximated by the first order term. For simplicity, the stress at the resting state (τ_0) was taken as zero herein.

For biofabrication processes, the external or mechanical stress is mainly taken as the von Mises stress, which is defined as follows:

$$\sigma_{VM} = \sqrt{\frac{3}{2}s_{hk}s_{kh}} \tag{5.38}$$

where s_{hk} $(h,k=1,2,3)$ are the components of the stress deviator tensor $\overline{\overline{\sigma}}_{dev}$, which is defined as

$$\overline{\overline{\sigma}}_{dev} = \overline{\overline{\sigma}} - \frac{1}{3}\left(\overline{\overline{\sigma}} : \overline{\overline{I}}\right)\overline{\overline{I}} \tag{5.39}$$

where $\overline{\overline{\sigma}}$ is the stress tensor, and $\overline{\overline{I}}$ is the unit tensor.

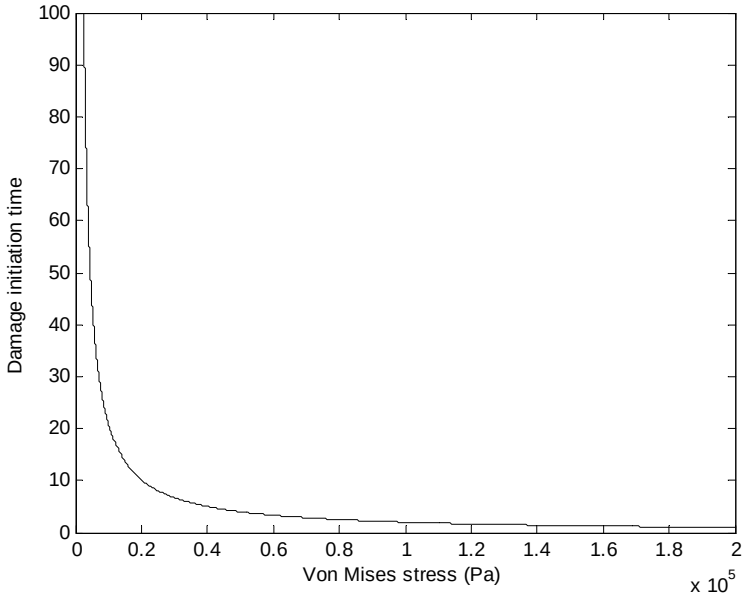

Figure 5.11: Damage initiation time as a function of effective von Mises stress with a 1 kPa stress threshold using the proposed approach and the Breuls model (two curves overlap with each other)

The relation between the dimensionless damage initiation time or time lag and the von Mises stress is obtained as shown in Fig. 5.11. Here the time lag was taken as 10 μs corresponding to an effective von Mises stress of 200 kPa, which are of the order of some proposed time lag and corresponding stress (Leverett et al. 1972), and the stress threshold (τ_c) was taken as 1 kPa below which the cell was not affected at all. Unless stated otherwise, these parameters were applied in the following sections. Figure 5.11 shows a

typical relationship between the damage initiation time and the effective von Mises stress using Eq. (5.36), which matches very well with that derived in modeling the accumulative skeletal muscle tissue damage using the strain energy density (Breuls et al. 2003b). In applying the Breuls model (Breuls et al. 2003b), the damage effective von Mises stress was also 200 kPa for a dimensionless time 1, and the corresponding time duration of exposure to the effective von Mises stress was taken as the time scale in the dimensionless time. As so, the critical damage parameter D_{cell} of the Breuls model (Breuls et al. 2003b) was 200 kPa. Actually, the damage initiation time proposed by Breuls et al. (Breuls et al. 2003b) happens to be a first-order approximation of Eq. (5.37) while the aforementioned two damage initiation times have been derived based on two different mechanisms: strain energy density (Breuls et al. 2003b) vs. singling pathway proposed herein.

5.4.2 Evaluation of the Proposed Cell Damage Model in Damage Modeling of Muscle Tissue

To evaluate the proposed cell damage methodology, the proposed cell damage model is first evaluated by comparing the damage predictions with the experimental results in the compression of an engineered muscle-skin layer tissue (Breuls et al. 2003a). During the evaluation process, the necessary model inputs for the proposed model were estimated using a finite element method (FEM) (ABAQUS 6.9-1). The construct of interest was under a constant compression force, which was applied on the skin surface with a displacement of 12 mm in the compression direction. For simplification, the FEM model only modeled the macrostructure of the muscle tissue with a skin layer. The material properties, boundary conditions, and model geometry were adopted as

introduced by Breuls et al. (Breuls et al. 2003b). The mesh included 74 quadratic, plane strain elements for the muscle and 9 additional same type elements on the top layer representing the skin layer. For the muscle tissue, the compression modulus and the shear modulus were 38.9 kPa and 10.1 kPa, respectively (Breuls et al. 2003b); for the skin layer, the compression modulus and the shear modulus were 19.5 kPa and 50.5 kPa, respectively (Breuls et al. 2003b). The Neo-Hookean hyperelastic model was used to model both the muscle tissue and the skin layer.

In the application of the cell damage model, it is assumed that the cell is damaged if the effective von Mises stress was 40 kPa with a time lag of 1 hour (Bosboom 2001) and the von Mises stress threshold was 4 kPa. The cell damage percentage was evaluated for the whole muscle tissue for a duration of 8 hours. For each time increment (0.5 hour), a damage degree was computed at each element integration point inside a mesh, which can represent cells in that local muscle region, and then the cell damage state was determined using Eq. (5.34). The cell damage percentage was then computed by dividing the number of damaged regions with respect to each integration point over the total number of integration points.

Figure 5.12 shows the damage evolutions of the model predictions and the *in vitro* experimental results (with the control effect included) (Breuls et al. 2003a), which shows a satisfactory modeling performance. The observed discrepancies between the model prediction and the experiment may be due to the following reasons: 1) the finite element model used is a simplified model which does not exactly reflect the stress field in the tissue construct; 2) the damage-related parameters of the cells are not well defined and known yet; and 3) other factors such as the cell concentration and distribution may also

influence the predicted cell damage percentage. Nevertheless, the overall damage evolution tendency can be well captured by the proposed cell damage model.

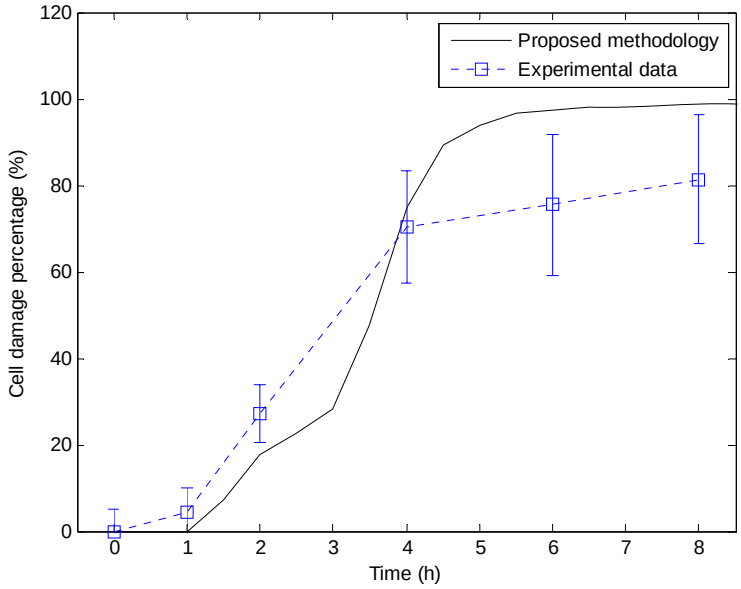

Figure 5.12: Comparison of cell damage percentage predictions and experimental results

5.5 Computational Analysis of Cell Damage in Laser-Assisted Cell Direct Writing

5.5.1 Cell Viability Modeling in MAPLE DW

The proposed cell damage model is further used to quantify the cell viability in a laser-assisted cell direct writing process, MAPLE DW. The schematic presentation of MAPLE DW is shown in Fig. 5.13, and its working mechanism is introduced briefly as follows. Focused highly energetic laser pulses are directed through the backside of the quartz support, over which the cell-based biomaterial is coated. These pulses are then absorbed by a laser-absorbing matrix of the biomaterial coating. Once the laser-absorbing material absorbs most of the laser pulse energy, it evaporates and forms a bubble due to

localized heating. Finally, this sublimation releases the remaining coating and a droplet is ejected from the interface to the movable receiving substrate underneath. Typical coating materials on the receiving substrate are hydrogel (Ringeisen et al. 2004) and cell culture (Lin et al. 2010). As mentioned, this MAPLE DW laser-assisted cell direct-write process can be divided into two main working stages: 1) the cell droplets are formed and ejected due to the laser energy-induced momentum, and 2) the cell droplets land onto a receiving substrate after traveling through a writing height.

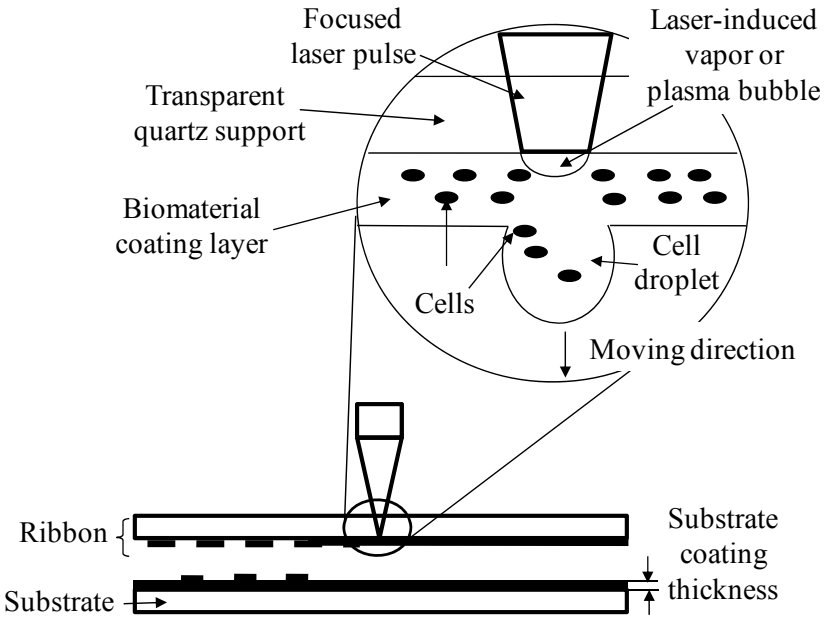

Figure 5.13: Schematic of a typical laser-assisted cell direct writing

It was observed that the landing process may lead to an undesirable post-transfer cell viability, and the cell viability can be controlled by adjusting the thickness of the receiving substrate coating (Ringeisen et al. 2004). In this study, the effect of cell landing process on the post-transfer cell viability is of modeling interest. Some assumptions are

introduced as follows: 1) only impact-induced cell damage is analyzed by neglecting possible cell damage due to the bubble-expansion and thermoelastic stresses during MAPLE DW; 2) the cell droplet has a spherical shape and is composed of uniformly distributed cells, which have the same mechanical properties; and 3) the cell droplet and coating are modeled as a uniform material without taking into account of their heterogeneity.

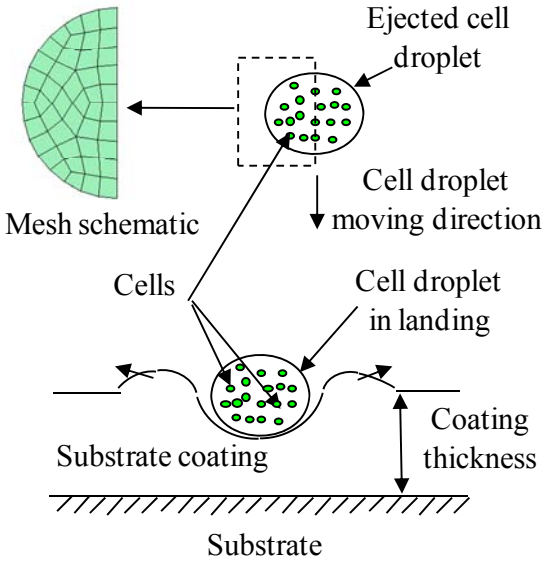

Figure 5.14: Schematic of a typical cell landing process

Mechanical stress should be first predicted in order to use the proposed cell damage model to estimate the cell viability in MAPLE DW. For the cell landing process shown in Fig. 5.14, an explicit arbitrary-Lagrangian-Eulerian (ALE) finite element method was used to model this landing-induced impact using LS-DYNA 971 (LS-DYNA 2007). Specifically, the cell droplet domain was modeled using the Lagrangain mesh which can capture the deformation history of the cell droplet; and the substrate coating

domain was modeled using the Eulerian mesh to avoid the extreme material deformation during impact.

The whole landing process and the involved material system were approximated axisymmetrical, so only one fourth of the three-dimensional (3D) computational model was implemented to capture this landing process. The cell droplet of interest had a diameter of 90 μm which was of the order of a typical laser spot size (Ringeisen et al. 2004) and was meshed by rotating a 45 elements cross section, resulting in 6 slices and total 270 solid elements inside a one-quarter cell droplet.

The cell droplet was modeled as a hyperelastic homogenous material using a Neo-Hookean model with a density of 1000 kg/m^3, shear modulus 15.6 kPa (Breuls et al. 03b), and Poisson's ratio 0.49 (Ohashi et al. 2005). The substrate coating was modeled with a Newtonian fluid, and the properties of water were used (Wang et al. 2008) since water is the dominant component of most hydrogel-based coating. The pressure of the coating was determined from the Mie-Grüneisen equation of state (Wang et al. 2008), and the coating material failure was controlled using a cutoff pressure, which was zero in this study (Wang et al. 2008).

The initial condition was applied by setting the cell droplet initial velocity as the landing velocity. This landing velocity was assumed the same as the droplet ejection velocity for a small writing height typically used in MAPLE DW. It was found that the bubble front velocity, which determines the cell droplet ejection velocity, can be approximated linearly with the laser fluence in laser-assisted direct writing (Duocasterlla et al. 2009), so the following linear function is proposed to correlate the applied laser fluence and the droplet ejection velocity as follows:

$$V_{ejection} = aI + b \tag{5.40}$$

where a and b are the coefficients, I is the laser fluence (mJ/cm^2), and $V_{ejection}$ is the ejection velocity of cell droplet (m/s). The coefficients a and b have been least-squares-fitted as 0.0296 and -0.8879, respectively, using the experimental data (Duocasterlla et al. 2009). As so, the ejection/landing velocity was estimated based on the linear approximation of the laser fluence.

The damage parameter k^* of Eq. (5.33) is a prerequisite for the proposed cell damage model, and k^* can be determined using Eq. (5.32) based on three parameters: the mechanical stress threshold (τ_c), a damage mechanical stress, and the corresponding time lag under that damage stress. Based on a previous study on the stress magnitude and the corresponding time lag for certain cell damage (Leverett et al. 1972), the time lag was taken as 10 μs under a 200 kPa von Mises stress. The cell damage threshold stress was assumed 1 kPa. It should be pointed out that these three values can be experimentally quantified for certain cells under specified external loadings for better prediction accuracy in the future.

For this landing process, the cell viability is finally determined as follows:

$$Cell\ viability = \frac{\sum_{i=1}^{N} P_i}{N} = \frac{\sum_{i=1}^{N} \varphi V_{di} P_i}{\varphi V_d} \approx \frac{\sum_{i=1}^{N} x_i A_i P_i}{\sum_{i=1}^{N} x_i A_i} \tag{5.41}$$

where φ is the number of cells per unit volume, V_d is the volume of the droplet, V_{di} is the volume of element i ($i = 1, 2, \ldots, 45$) in each slice, P_i is the living state of element i with one or more cells inside, A_i denotes the element area on the droplet

cross-section, which is the average element area on the droplet cross-section, and x_i is the average distance of the element i to the axisymmetric axis of the cell droplet, which is defined as the average distance of nodes of element i.

In summary, the cell viability is determined based on the following procedure. First, the von Mises stress is calculated for each element in the slice; second, for each cell element, the accumulative K' is obtained using Eq. (33); then the state of each element is determined using Eq. (5.34); and finally, the final cell viability is determined from Eq. (5.41).

For MAPLE DW simulations, the cell viability was studied as a function of the laser fluence, ranging from 367 mJ/cm^2 to 1718 mJ/cm^2, which was equivalent to a landing velocity from 10 m/s to 50 m/s. The substrate coating was taken as 100 μm, and the cell viability was estimated at 20 μs after landing since the effect of impact was negligible after 20 μs in this study. The cell viability as a function of laser fluence is shown in Fig. 5.15. It can be seen that the cell viability increases with the laser fluence since a higher laser fluence leads a higher impact force, resulting in a lower cell viability. Such a tendency also matches that of the viability in printing the human colon cancer cell using MAPLE DW (Lin et al. 2010a). The discrepancy between the prediction and the experimental measurement may be due to: 1) the simulated cell landing velocity using Eq. (5.40) may be not accurate enough for this MAPLE DW setup; 2) the simulation results here are for a general cell damage study without specifying the actual cell type and the cell damage properties such as the time lag for a given stress and the stress threshold; and 3) the material properties and geometries of cell droplet and coating material used in the simulation may be different from those of the experiments (Lin et al.

2010a). These reasons may also lead to the discrepancies observed in the following parametric study.

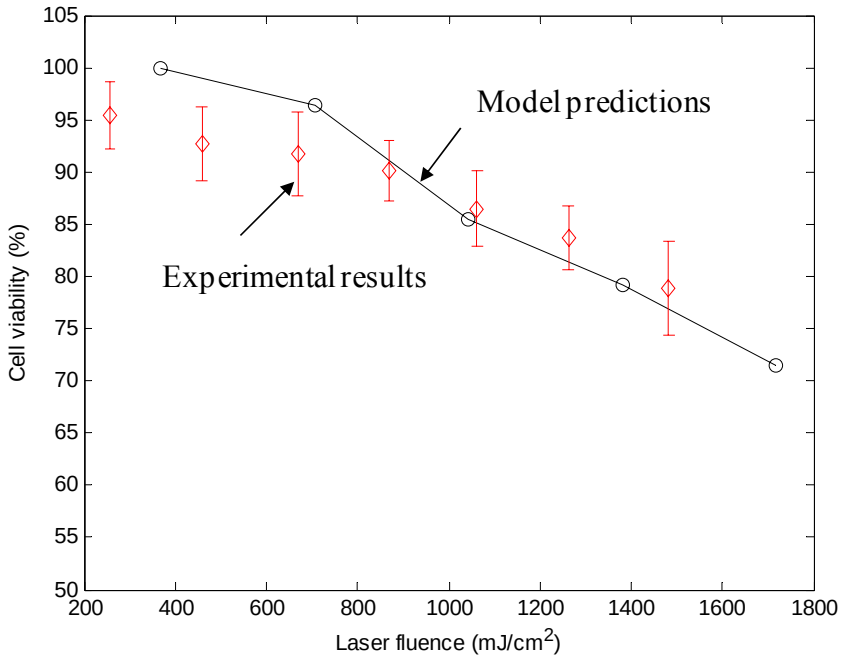

Figure 5.15: Cell viability as a function of laser fluence

5.5.2 Parametric Study

5.5.2.1 Effect of Landing Velocity

The effect of landing velocity in MAPLE DW on the post-transfer cell viability is further studied and shown in Fig. 5.16. For a given 100 μm coating, the landing velocity was changed from 10 m/s to 50 m/s with an increment of 10 m/s, which was of the order of the ejection velocity estimated using Eq. (5.40) based on the laser fluence setup in typical laser-assisted cell direct writing (Lin et al. 2010a).

The impact-induced mechanical stress may trigger the cell apoptosis pathway during MAPLE DW. Under large landing velocities, the impact-induced cell deformation

becomes more severe. As expected, under large landing velocities which can be controlled by laser fluencies in MAPLE DW, the post-transfer cell viability decreases.

The proposed cell damage model considers the time accumulative effect in addition to the amplitude of mechanical stress. In fact, the peak stress which a cell may experience during MAPLE DW, especially during landing, is usually much higher (Wang et al. 2008) than that a living cell may endure. It should be pointed out that if only a stress threshold value is used as a cell damage criterion without considering the time accumulative effect (Sundaram et al. 2003), the cell viability would become zero for some simulations, which do not match with those observed (Breuls et al. 2003a).

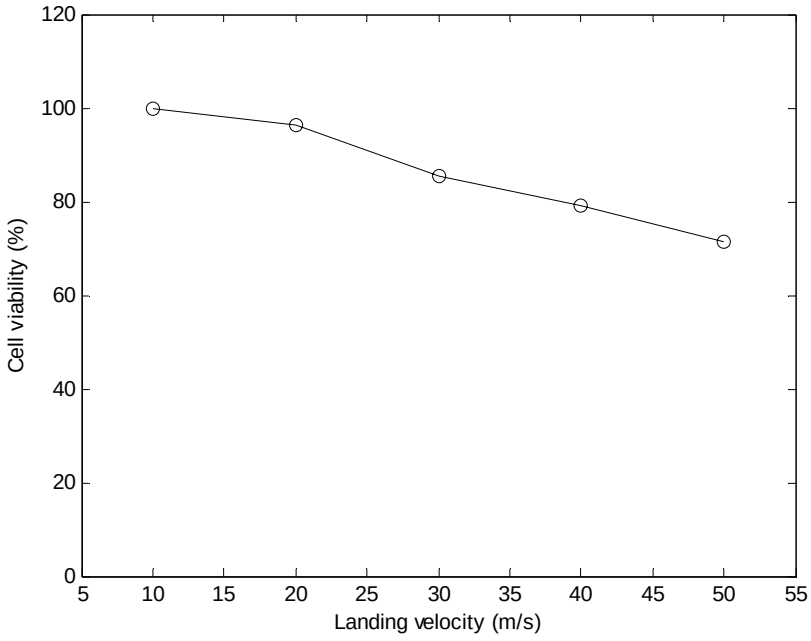

Figure 5.16: Cell viability as a function of landing velocity (with a 100 μm coating)

5.5.2.2 Effect of Substrate Coating Thickness

The effect of coating thickness in MAPLE DW on the post-transfer cell viability is shown in Fig. 5.17. For a given 30 m/s landing velocity, the cell viability was estimated under a coating thickness of 20 μm, 40 μm, and 100 μm, which was of the order of the typical coating thickness in laser-assisted cell printing (Ringeisen et al. 2004).

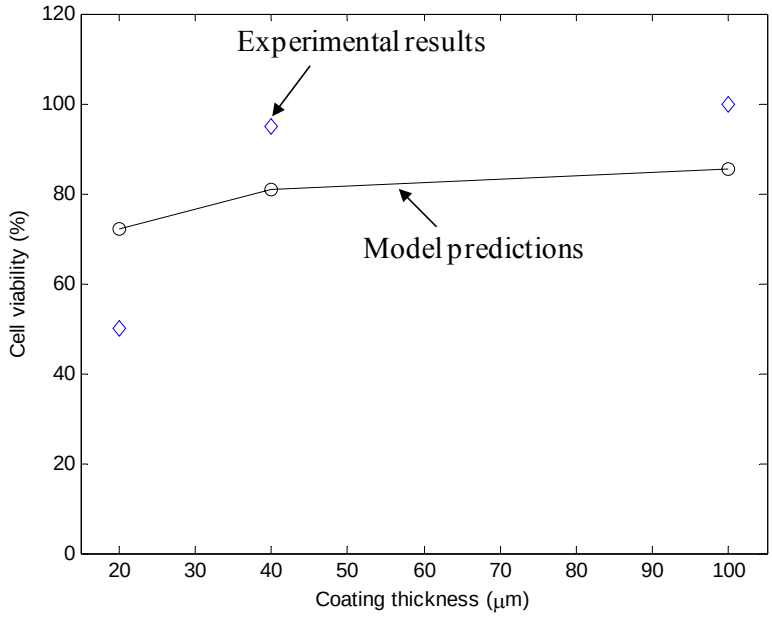

Figure 5.17: Cell viability as a function of coating thickness (with a 30 m/s landing velocity)

The protective effect of substrate coating has also been experimentally studied during laser printing of pluripotent embryonal carcinoma cells by Ringeisen et al. (Ringeisen et al. 2004). In that study, a 5% post-transfer cell viability was achieved using an uncoated quartz receiving substrate; however, roughly 50% of the cells transferred onto a thinner hydrogel coating (20 μm) appeared viable after printing (Ringeisen et al.

2004). Furthermore, the viability reached 95% for cells transferred onto a thicker coating (40 μm) and almost 100% if the coating was even much thicker. The model predictions also present a similar relationship between the cell viability and the coating thickness and show the protective effect of coating, and this effect becomes less significant if the coating thickness is larger than a certain value. It should be noted that the predicted cell viability for the 20 μm coating case will be lower than that shown in Fig. 5.17 as the simulation stopped at 16 μs after encountering extreme element distortion, which means a more accurate prediction might be reached.

5.6 Conclusions and Future Work

As widely recognized, tissue biofabrication processes might introduce excessive thermal and/or mechanical stresses to biological materials including living cells. If this process-induced stress exceeds the adaptive capacity of a cell and irreversible injury may occur, leading to unexpected necrosis. Thus far, there is no available systematic study to understand and model cell damage using a combined biological and engineering approach. This study has proposed a new mathematical approach to biophysically predict the biofabrication-induced cell damage based on the triggered molecular signaling pathway in the cellular network. The key contribution is to elucidate and model how an external stress signal leads to cell death through a dynamic duration-dependent process.

The proposed cell damage model includes two characteristics: 1) the cell may be dead only when the external stress exceeds a certain threshold value. Below this value, the cell does not commit any fate decision; and 2) if the external stress is higher than the threshold stress, the signaling pathway is triggered and may cause cell death depending

on the time accumulative effect of external stress. That is, cell damage depends on the stress threshold, the external stress magnitude and its duration.

This cell damage model is validated in damage modeling of a muscle-skin tissue and further applied to investigate the post-transfer cell viability in a laser-assisted cell direct writing process, MAPLE DW. The predicted effects of laser fluence, cell droplet landing velocity, and substrate coating thickness on the post-transfer cell viability match the experimental results reasonably well.

More importantly, the proposed methodology provides a biophysics-based approach as a starting point to investigate cell damage under influences of a variety of mechanical, chemical and biological environments by considering specific molecular networks in a cell. While the present model provides a mathematical modeling approach of cell damage under the combined effect of stress and its duration, some important future work is listed as follows:

(1) In the application of the proposed cell damage model, the experimental quantification of cell damage parameters for a specific cell is indispensable;

(2) A definite relationship between the mechanical stress and its resulting biological stress which induces BH3 or caspase 8 needs to be found; and

(3) The additive effect of both two pathways should be considered and modeled based on the progress in cell apoptosis.

CHAPTER 6

CONCLUDING REMARKS AND FUTURE WORK

6.1 Conclusions

The objective of this dissertation is to model the laser-assisted cell direct writing processes and further model the cell damage based on the process modeling. The major conclusions from this thesis are summarized in the following discussions.

6.1.1 Modeling of Bubble Expansion-Induced Cell Mechanical Profile

The bubble expansion due to vaporization and/or optical breakdown is the main mechanism for material ejection in laser-assisted cell direct writing. The bubble expansion leads to the generation of stress wave which is exerted on the embedded cells in the coating. Some conclusions of the cell mechanical profile are summarized as follows.

The cell velocity oscillates initially and then smoothes out gradually with a constant ejection velocity. The cell can first accelerate as high as 10^9 m/s^2 at the beginning period of bubble expansion and then quickly approaches zero in an oscillation manner; fortunately, this high acceleration period only lasts a very short period (about 0.1 μs). The cell pressure can be very high at the beginning period of bubble expansion and quickly decreases to zero in an oscillation manner as seen from the cell acceleration evolution. The cell top surface region usually experiences the highest pressure level, followed by the bottom surface and the middle regions. A high viscosity can lead to an observable velocity increment at the initial stage due to the pronounced viscous friction effect, but the ejection velocity decreases because of the excessive viscous energy

dissipation. The pressure magnitude decreases when the cell-bubble distance is large. It is generally expected that for the coating embedded with multiple cells, the cells close to the bubble are more susceptible to mechanical damage. A larger initial pressure induces a larger cell pressure as expected. As a result, the cell viability is adversely affected by large initial pressures.

6.1.2 Modeling of Thermoelastic Stress Wave

When the laser pulse is very short (usually on the order of submicrosecond), the prominent thermoelastic stress is generated. In comparison with a purely thermal vaporization and optical breakdown, the generation of thermoelastic stress needs less energy per unit volume. Some conclusions are given as follows.

Under the presence of thermoelastic stress, the compressive pressure wave propagates along the axisymmetric axis with a commensurate size of the laser spot while there may be a following tensile stress wave if the laser spot size is finite. The laser irradiation-induced thermoelastic stress profiles have bipolar characteristics, and their peak magnitudes are on the order of 1 MPa or higher. The stress waves reflected from the coating-air free surface change its sign and have decreasing magnitude when traveling inside the coating. The higher magnitudes of original laser radiation-induced pressure pulse pairs are achieved at the locations which are closer to the laser spot. Shorter duration laser pulses lead to higher thermoelastic stresses and higher laser fluence leads to higher thermoelastic stresses.

6.1.3 Modeling of Cell Landing

After the cell droplets are ejected from the biomaterial coating on the quartz support, they land onto the movable receiving substrate underneath. Impact between the

cell droplets and the receiving substrate was modeled to understand the cell damage. Some conclusions are given as follows:

The cell peripheral regions, especially the bottom peripheral region, usually experience a higher stress level than that of the inner regions. It indicates that the cell membrane is easy to be adversely affected by the impact-induced mechanical damage during cell direct writing. The cell mechanical loading profile and the cell posttransfer viability depend on the cell droplet initial velocity and the substrate coating thickness. Generally, a larger initial velocity poses a higher probability of cell damage, and a substrate coating can significantly reduce the cell mechanical damage severity. Two important impact processes may occur during the cell droplet landing process after ejection: the first impact between the cell droplet and the substrate coating and the second impact between the cell and the substrate. It is assumed that the impact-induced cell damage depends on not only the magnitudes of stress, acceleration, and/or shear strain but also the cell loading history. In fact, the collective cell momentum change over the whole impact duration instead of peak values of stress, acceleration and/or strain looks critical in determining the cell viability during cell direct writing. For better understanding of cell damage during direct writing, future studies should apply realistic cell and hydrogel constitutive models, consider the mechanical damage during the cell droplet formation process (ejection), and include the possible process-induced thermal damage. Also, how to quantify the cell damage degree should be carefully addressed, validated and interpreted.

6.1.4 Cell Damage Model

This work gave a systematic study to understand and model cell damage using a combined biological and engineering approach. A new mathematical approach was proposed to biophysically predict the biofabrication-induced cell damage based on the triggered molecular signaling pathway in the cellular network. Some conclusions can be drawn for the present cell damage model: 1) the cell damage model was proposed based on the molecular signaling pathways in cell death. This model considers the effect of the loading strength and the time duration on cell death. Specifically, if the cell damage degree is equal to or larger than 1, the cell is dead. If the cell damage degree is smaller than 1, the cell is alive; 2) for dynamic processes, the cell damage model considers the time accumulative effect of the external stress on cell death.

In the study of cell damage of the laser assisted cell direct writing, it concludes that 1) for large laser fluencies, the cell viability decreases; 2) the coating shows a protective effect on the cell viability and this protective effect becomes less significant if the coating thickness is larger than a certain value.

6.2 Contributions

Previous experimental work has been done to study the cell viability under different operating conditions in cell printing. Thus far, there is no theoretical or computational modeling of these processes and the study of the process-induced cell damage is still lacking. The research in this dissertation fills in this gap, which helps to facilitate the optimization and wide application of laser-assisted cell direct writing in tissue regeneration research.

The research in this thesis has contributions which are listed as follows:

(1) The bubble expansion-induced cell mechanical profile during the droplet formation process was modeled. The numerical modeling predicated the droplet ejection velocity, acceleration and pressure, which helped to investigate the cell damage. The effect of viscosity of the coating material, the initial bubble pressure, and cell-bubble distance were studied.

(2) Thermoelastic stress wave propagation was modeled by considering the unique boundary conditions during the droplet formation process. The finite difference method was applied to solve the equation by considering the appropriate boundary conditions. The effects of laser pulse and laser fluence on the thermoelastic stress wave were studied.

(3) Cell mechanical profile during the cell-hydrogel coating impact process was modeled. The impact-induced cell mechanical loading profile, including the velocity, acceleration, and shear stress, during the cell landing was studied. The effect of typical process variables such as the droplet initial velocity and the coating thickness on the cell loading profile during the cell landing was carefully studied to understand the cell damage.

(4) A new mathematical approach was proposed based on the triggered molecular signaling pathway in the cellular network. The key contribution was to elucidate and model how an external stress signal leads to cell death through a dynamic process. More importantly, the proposed methodology provided a biophysics-based approach to investigate cell damage under influences of a variety of mechanical, chemical and biological environments by considering specific molecular networks in a cell.

6.3 Future Work

This dissertation studied the cell mechanical profile due to bubble expansion, thermoelastic stress wave generation and cell mechanical profile during cell landing. A systematic study of cell damage was also given based on the triggered molecular signaling pathway in the cellular network. Some future work can be summarized as follows:

6.3.1 Modeling of Bubble Expansion-Induced Cell Mechanical Profile

In laser-assisted cell direct writing, direct modeling of the temporal evolution and spatial distribution of the energy absorption during vaporization and optical breakdown is very complicated, and the processes depend strongly on the laser pulse characteristics and material optical properties. In this study, the simulation started with an initial formed bubble. In the future, physical understanding and modeling of the bubble formation and the subsequent bubble expansion should be further investigated.

The stress wave propagation depends on the medium properties such as surface tension and viscosity. For biological materials, elastic properties also play a role. To fully model the stress wave generated in the biological coating, a more realistic model which includes all these effects should be further investigated.

In addition, modeling of the cell mechanical profile during bubble expansion should include the effect of cell biological structure in the future since the cell membrane, and internal structure of a cell may play an important role in determining the cell mechanical profile. A more realistic computational model, taking into account the microstructural properties of the cell droplet and coating materials, needs to be further incorporated.

Future experimental investigation should also be performed to directly validate the bubble expansion-induced cell mechanical profile during ejection.

6.3.2 Modeling of Thermoelastic Stress Wave

The generation of thermoelastic stress by the absorption of laser radiation in a liquid medium becomes prominent if the thermal confinement and stress confinement conditions are satisfied. The thermoelastic effect is associated with the thermal expansion of a rapidly heated volume of the medium. Specifically, the thermoelastic stress generation depends on the laser pulse characteristics as well as the physical properties of the medium. In the present work, the effects of the laser pulse characteristics, including laser fluence and laser pulse duration, on the thermoelastic stress wave were studied. In fact, optical absorption coefficient of the medium also influences the stress wave generation. In the future, the effect of coating absorbing coefficient on the thermoelastic stress wave generation and the resulting pressure profiles should be further modeled.

Thermoelastic stress may affect the phase explosion threshold during the laser-coating interaction. The onset of a tensile stress-induced phase explosion is determined by the tensile strength of liquid such as water at the room temperature. The thermodynamic phase diagram between the pressure and temperature shows that the existence of tensile thermoelastic stress can significantly reduce the free energy barrier to homogenous nucleation and the spinodal decomposition temperature. In the future, the stress wave-induced cavitation bubble formation should be further addressed.

6.3.3 Modeling of Cell Landing

In laser-assisted cell direct writing, multiple droplets with different cell distribution are ejected from the quartz support. The cell distribution and cell-cell

interaction within the cell droplets influence the cell mechanical profile in the cell landing. A more realistic computational model which considers these influences should be further considered to give a full understanding of the cell landing process.

During the impact process, the interaction between the cell and the surrounding medium depends strongly on the properties of the medium. In the future study, a more realistic model should be addressed considering the effect of the microstructural properties of the coating materials on the deformation of cells.

In addition, a cellular structure is not homogenous. To better model the biophysical response of cells, a microstructural model of cells needs to be further incorporated.

6.3.4 Cell Damage Model

Cell damage is a very complex biophysical and/or biochemical process. For the present cell damage model, a caspase-dependent signaling pathway was considered based on a general intrinsic pathway and extrinsic pathway modeling. For certain cell types under certain conditions, specific molecule reactions and parameters should be considered in the future.

The proposed cell damage model is characterized by three parameters: the threshold value of cell damage, the damage stress magnitude and the corresponding time duration. As a starting point, the model parameters were chosen based on precious studies for certain cell damage. The experimental quantification of the damage parameters for specific cell types needs to be carefully considered in the future.

In addition, thus far, a clear relationship between the external stress and the biological signal transduction is not well understood. The present study gave a liner

approximation between the external stress and its resulting biological stress. Future work can be directed to a more clear relationship of the mechanical stress and its resulting biological stress.

Finally, in this work, only either intrinsic pathway or extrinsic pathway was considered to trigger the cell death by ignoring their cooccurrence. Some studies demonstrated that the two pathways can be triggered together and contributed to cell apoptosis in an additive manner. In the future, the additive effect of both pathways should be considered and modeled based on the progress in cell apoptosis.

APPENDICES

Appendix A

Table A-1: Model components and explanations in the pathway modeling

Notation	Explanation
aC9	Active caspase 9
BAR	Bifunctional apoptosis regulator
BAX	BCL2-associated X protein
BAXm	Active BAX, inserted in mitochondrial outer membrane
BAXm/BCL2	Complex of BAXm and BCL2
BCL2	Class of antiapoptotic BCL subfamily proteins
BH3	Class of proapoptotic BH3-only subfamily proteins
BH3/BCL2	Complex of BH3 and BCL2
BID	BH3-interacting domain death agonist
BIM	Bcl-2 interacting mediator of cell death
CC,CO	Closed and open states of mitochondrial channels
C3	Caspase 3
C8	Caspase 8
C9	Caspase 9
CytoC	Cytochrome c in cytoplasm
CytoCmito	Cytochrome c in mitochondria
ProC3	Inactive procaspase 3
ProC8	Inactive procaspase 8
ProC9	Inactive procaspase 9

SMAC	Second mitochondria-driven activation of caspase
SMACcyto	Second mitochondria-driven activation of caspase, in cytoplasm
SMACmito	SMAC in mitochondria
SMAC/XIAP	Dimer of SMAC and XIAP
XIAP	X-linked inhibitor of apoptosis protein

"[ ]" denotes the concentration of the component.

Appendix B

Equations, Parameters and Initial Conditions of the Intrinsic Pathway Model

The following part lists the ODE equations, parameters, and initial conditions of the intrinsic pathway model (Zhang et al. 2009) adopted in this study. The molecule concentrations and stress are dimensionless quantities, and the rate constants have units of $\min^{-1}$.

B.1 Initiator module system equations

$$\frac{d[BAX]}{dt} = (k_{f1} + k_{f2} \times [BH3]) \times [BAX] + k_b \times [BAXm]_F + k_b \times [BAXm/BCL2] \tag{B-1}$$

$$\frac{d[BAXm/BCL2]}{dt} = k_{asBAXmBCL2} \times [BAXm]_F \times [BCL2]_F - k_{dsBAXmBCL2} \times [BAXm/BCL2] - k_b \times [BAXm/BCL2] \tag{B-2}$$

$$\frac{d[BH3]_F}{dt} = k'_{sBH3} + k''_{sBH3} \times stress - k_{dBH3} \times [BH3]_F - k_{asBH3BCL2} \times [BH3]_F \times [BCL2]_F + k_{dsBH3BCL2} \times [BH3/BCL2] \tag{B-3}$$

$$\frac{d[BH3/BCL2]}{dt} = k_{asBH3BCL2} \times [BH3]_F \times [BCL2]_F - k_{dsBH3BCL2} \times [BH3/BCL2] - k_{dBH3} \times [BH3/BCL2] \tag{B-4}$$

$$[BAXm]_F = [BAX]_T - [BAX] - [BAXm/BCL2]$$

$$[BCL2]_F = [BCL2]_T - [BH3/BCL2] - [BAXm/BCL2]$$

Related parameters:

$[BCL2]_T = 80$, $[BAX]_T = 100$, Stress=0.1, $k_{f1} = 1$, $k_{f2} = 3$, $k_b = 3$, $k_{asBAXmBCL2} = 90$, $k_{dsBAXmBCL2} = 0.05$, $k_{asBH3BCL2} = 10$, $k_{dsBH3BCL2} = 0.01$, $k'_{sBH3} = 0.1$, $k''_{sBH3} = 0.6$, and $k_{dBH3} = 0.01$

Initial conditions:

$[BAX] = 66.6$, $[BAXm/BCL2] = 33.4$, $[BH3]_F = 0$, and $[BH3/BCL2] = 16$

B.2 Amplifier module system equations

$$\frac{d[CO]}{dt} = k_{open} \times [BAXm]_F^m \times ([C]_T - [CO]) - k_{close} \times [CO] \quad \text{(B-5)}$$

$$\frac{d[SMAC_{mito}]}{dt} = -[CO] \times [SMAC_{mito}] \quad \text{(B-6)}$$

$$\frac{d[CytoC_{mito}]}{dt} = -[CO] \times [CytoC_{mito}] \quad \text{(B-7)}$$

$$\frac{d[SMAC_{cyto}]}{dt} = \varepsilon \times [CO] \times [SMAC_{mito}] - k_{dSMACcyto} \times [SMAC]_F - k_{dsx} \times [SMAC/XIAP] \quad \text{(B-8)}$$

$$\frac{d[CytoC]}{dt} = \varepsilon \times [CO] \times [CytoC_{mito}] - k_{dCYTOC} \times [CytoC] \quad \text{(B-9)}$$

Related parameters:

$k_{open} = 10$, $m = 4$, $k_{close} = 10000$, $k_{close} = 10000$, $k_{dSMACcyto} = 0.0001$, $k_{dCYTOC} = 0.005$, $\varepsilon = 0.01$, and $[C]_T = 1$

Initial conditions:

$[SMAC_{mito}] = 1600$, $[CytoC_{mito}] = 800$, $[CytoC] = 0.1$, $[SMAC_{cyto}]_T = 0$, and $[CO] = 0$

B.3 Executioner module system equations

$$\frac{d[\mathrm{Pr}\,oC9]}{dt} = k_{sproc9} - k_{dproc9}[\mathrm{Pr}\,oC9] - k_{sc9} \times [\mathrm{Pr}\,oC9] \times [CytoC]^n \tag{B-10}$$

$$\frac{d[\mathrm{Pr}\,oC3]}{dt} = k_{sproc3} - k_{dproc3} \times [\mathrm{Pr}\,oC3] - (k'_{ac3} + k''_{ac3} \times [C9]^n + k'''_{ac3} \times [aC9]^n) \times [\mathrm{Pr}\,oC3] \tag{B-11}$$

$$\frac{d[C9]}{dt} = k_{sC9} \times [CytoC]^n \times [\mathrm{Pr}\,oC9] - k_{dc9} \times [C9] - (k'_{aC9} + k''_{aC9} \times [C3]^n) \times [C9] - k_{as9x} \times [C9] \times [XIAP]_F + k_{ds9x} \times [XIAP/C9] \tag{B-12}$$

$$\frac{d[aC9]}{dt} = (k'_{aC9} + k''_{aC9} \times [C3]^n) \times [C9] - k_{dac9} \times [aC9] \tag{B-13}$$

$$\frac{d[C3]}{dt} = (k'_{aC3} + k''_{aC3} \times [C9]^n + k''_{aC3} \times [aC9]^n) \times ([\mathrm{Pr}\,oC3]) - k_{dC3} \times [C3] - k_{as3x} \times [C3] \times [XIAP]_F + k_{ds3x} \times [XIAP/C3] \tag{B-14}$$

$$\frac{d[XIAP/C9]}{dt} = k_{as9x} \times [C9] \times [XIAP]_F - k_{ds9x} \times [XIAP/C9] - k_{d9x} \times [XIAP/C9] \tag{B-15}$$

$$\frac{d[XIAP/C3]}{dt} = k_{as3x} \times [C3] \times [XIAP]_F - k_{ds3x} \times [XIAP/C3] - k_{d3x} \times [XIAP/C3] \tag{B-16}$$

$$\frac{d[SMAC/XIAP]}{dt} = k_{assx} \times [SMAC]_F \times [XIAP]_F - k_{dssx} \times [SMAC/XIAP] - k_{dsx} \times [SMAC/XIAP] \tag{B-17}$$

$$[SMAC]_F = [SMAC_{cyto}]_T - [SMAC/XIAP]$$

$$[XIAP]_F = [XIAP]_T - [SMAC/XIAP] - [XIAP/C3] - [XIAP/C9]$$

Related parameters:

$k_{sproc3} = 0.002$, $k_{dproc3} = 0.001$, $k_{sproc9} = 0.001$, $k_{dproc9} = 0.001$, $k'_{ac9} = 0.001$, $k''_{aC9} = 0.5$

$k_{sC9} = 0.001$, $k_{dC9} = 0.002$, $k_{daC9} = 0.003$, $k'_{aC3} = 0.001$, $k''_{aC3} = 0.02$, $k'''_{aC3} = 0.5$,

$n = 2$, $k_{dc3} = 0.002$, $k_{as9x} = 0.1$, $k_{ds9x} = 0.6$, $k_{d9x} = 0.2$, $k_{as3x} = 0.2$, $k_{ds3x} = 0.5$,

$k_{d3x} = 0.1$, $k_{assx} = 2$, $k_{dssx} = 0.01$, $k_{dsx} = 0.007$, and $[XIAP]_T = 6$

Initial conditions:

$[\mathrm{Pr}oC3] = 1$, $[\mathrm{Pr}oC9] = 1$, and other variables are zero.

REFERENCES

Albeck, J. G., Burke, J. M., Aldridge, B. B., Zhang, M., Lauffenburger, D. A. and Sorger, P. K., 2008, "Quantitative Analysis of Pathways Controlling Extrinsic Apoptosis in Single Cells," Mol. Cell., Vol. 30, pp. 11-25.

Al-Rubeai, M., Oh, S. K. W., Musaheb, R. and Emery, A. N., 1990, "Modified Cellular Metabolism in Hybridomas Subjected to Hydrodynamics and Other Stresses," Biotechnology Letters, Vol. 12, pp. 323-328.

Anderson, R. R., and Parrish, J. A., 1983, "Selective Photothermolysis: Precise Microsurgery by Selective Absorption of Pulsed Radiation," Science, Vol. 220, pp. 524-527.

Apenberg, S., Freyberg, M. A. and Friedl, P., 2003, "Shear Stress Induces Apoptosis in Vascular Smooth Muscle Cells via an Autocrine Fas/FasL Pathway," Biochemical and Biophysical Research Communication, Vol. 310, pp. 355-359.

Arden, N., and Betenbaugh, M. J., 2004, "Life and Death in Mammalian Cell Culture: Strategies for Apoptosis Inhibition," Trends Biotech, Vol. 22, pp. 174-180.

Bagci, E. Z., Vodovotz, Y., Billiar, T. R., Ermentrout, G. B., and Bahar, I., 2006, "Bistability in Apoptosis: Roles of Bax, Bcl-2, and Mitochondrial Permeability Transition Pores," Biophys. J., Vol. 90, pp. 1546-1559.

Barbee, K. A., 2005, "Mechanical Cell Injury," Ann. N.Y. Acad. Sci., Vol. 1066, pp. 67-84.

Barron, J. A., Ringeisen, B. T., Kim, H., Spargo, B. J., and Chrisey, D. B., 2004, "Application of Laser Printing to Mammalian Cells," Thin Solid Films, Vol. 453-454, pp. 383-387.

Barron, J. A., Wu, P., Ladouceur, H. D., and Ringeisen, B. R., 2004, "Biological Laser Printing: a Novel Technique for Creating Heterogeneous 3-Dimensional Cell Patterns," Biomed. Microdevices, Vol. 6(2), pp. 139-147.

Bilek, A. M., Dee, K. C. and Gaver, D. P., 2003, "Mechanisms of Surface-Tension-Induced Epithelial Cell Damage in a Model of Pulmonary Airway Reopening," J. Appl. Physiol., Vol. 94, pp. 770-783.

Blackshear, P. L., Dorman, F. D., and Steinbach, J. H., 1965, "Some Mechanical Effects That Influence Haemolysis," Trans Am Soc Artif Intern Organs, Vol. 11, pp. 112-117.

Born, C., Zhang, Z., Al-Rubeai, M., and Thomas, C. R., 2002, “Estimation of Disruption of Animal Cells by Laminar Shear Stress,” Biotechnology and Bioengineering, Vol. 40, pp. 1004-1010.

Bosboom, E. M. H., 2001, “Deformation as a Trigger for Pressure Sore Related Muscle Damage”, Ph.D. thesis, University of Eindhoven.

Bouten, C. V. C., Knight, M. M., Lee, D. A., and Bader, D. L., 2001, ‘‘Compressive Deformation and Damage of Muscle Cell Subpopulations in a Model System,’’ Ann. Biomed. Eng., Vol. 29, pp.153-163.

Breuls, R. G. M., Bouten, C. V. C., Oomens, C. W. J., Bader, D. L., and Baaijens, F. P. T., 2003a, “Compression Induced Cell Damage in Engineered Muscle Tissue: An In Vitro Model to Study Pressure Ulcer Aetiology,” Annals of Biomedical Engineering, Vol. 31, pp. 1357-1364.

Breuls, R. G. M., Bouten, C. V. C., Oomens, C. W. J., Bader, D. L., and Baaijens, F. P. T., 2003b, “A Theoretical Analysis of Damage Evolution in Skeletal Muscle Tissue with Reference to Pressure Ulcer Development,” Journal of Biomechanical Engineering, Vol. 125, pp. 902-909.

Brujan, E. A. and Vogel, A., 2006, “Stress Wave Emission and Cavitation Bubble Dynamics by Nanosecond Optical Breakdown in a Tissue Phantom,” J. Fluid Mech., Vol. 558, pp. 281-308.

Byun, K. T., and Kwak, H. Y., 2004, “A Model of Laser-Induced Cavitation,” Japanese Journal of Applied Physics, Vol. 43(2), pp. 621-630.

Carome, E. F., Clark, N. A., and Moeller, C. E., 1964, “Generation of Acoustic Signals in Liquids by Ruby Laser-Induced Thermal Stress Transients,” Appl Phys Lett, Vol. 4, pp. 95-97.

Carter, D. R. and Caler, W. E., 1985, “A Cumulative Damage Model for Bone Fracture,” Journal of Orthopaedic Research, Vol. 3, pp. 84-90.

Chan, G., Booth, A. J., Mannweiler, K., and Hoare, M., 2006, "Ultra Scale-down Studies of the Effect of Flow and Impact Conditions During E. coli Cell Processing," Biotechnol Bioeng., Vol. 95(4), pp.671-683.

Chang, R., Nam, J., and Sun, W., 2008, “Effects of Dispensing Pressure and Nozzle Diameter on Cell Survival from Solid Freeform Fabrication-Based Direct Cell Writing,” Tissue Eng. Part A, Vol. 14, pp. 41-48.

Christensen, R., 2002, “An Evaluation of Linear Cumulative Damage (Miner’s Law) Using Kinetic Crack Growth Theory,” Mechanics of Time-Dependent Materials, Vol. 6, pp. 363-377.

Cossali, G. E., Coghe, A., and Marengo, M., 1997, "The Impact of a Single Drop on a Wetted Solid Surface," Exp. Fluids, Vol. 22, pp. 463-472.

Cotter, T. G. and Al-Rubea, M., 1995, "Cell Death (apoptosis) in Cell Culture Systems," Trend in Biotechnology, Vol. 13(4), pp. 150-155.

Dingus, R. S., and Scammon, R. J., 1991, "Grüneisen-Stress-Induced Ablation of Biological Tissue," Proc. SPIE, Vol. 1427, pp. 45-54.

Dingus, R. S., Curran, D. R., Oraevsky, A. A. and Jacques, S. L., 1994, "Microscopic Spallation Process and Its Potential Role in Laser-Tissue Ablation," Proc. SPIE, Vol. 2134A, pp. 434-445.

Desagher, S., Osen-Sand, A., Nichols, A., Eskes, R., Montessuit, S., Lauper, S., Maundrell, K., Antonsson, B. and Martinou, J. C., 1999, "Bid-Induced Conformational Change of Bax is Responsible for Mitochondrial Cytochrome c Release during Apoptosis," J. Cell Biol., Vol. 144, pp. 891-901.

Deveraux, Q. L., Leo, E., Stennicke, H. R., Welsh, K., Salvesen, G. S. and Reed, J. C., 1999, "Cleavage of Human Inhibitor of Apoptosis Protein XIAP Results in Fragments with Distinct Specificities for Caspases," EMBO J., Vol. 18, pp. 5242-5251.

Doukas, A. G., McAuliffe, D. J. and Flotte, T. J., 1993, "Biological Effects of Laser-Induced Shock Waves: Structural and Functional Cell Damage In Vitro," Ultrasound Med. Biol., Vol. 19, pp. 137-146.

Doukas, A. G., McAuliffe, D. J., Lee, S., Venugopalan, V., and Flotte, T. J., 1995, "Physical Factors Involved in Stress-Wave-Induced Cell Injury: The Effect of Stress Gradient," Ultrasound Med. Biol., Vol. 21, pp. 961-967.

Doukas, A. G. and Flotte, T. J., 1996, "Physical Characteristics and Biological Effects of Laser-Induced Stress Wave," Ultrasound in Med. &Biol., Vol. 22(2), pp. 151-164.

Doukas, A. G., 1998, "Laser-Generated Stress Waves in Medicine: from Tissue Injury to Drug Delivery," Biomedical Optical Spectroscopy and Diagnostics/Therapeutic Laser Applications, Vol. 22, pp. 312-316.

Drury, J. L., Dennis, R. G., and Mooney, D. J., 2004, "The Tensile Properties of Alginate Hydrogels," Biomaterials, Vol. 25, pp. 3187-3199.

Duocastella, M., Fernández-Pradas, J. M, Morenza, J. L. and Serra, P., 2009, "Time-Resolved Imaging of the Laser Forward Transfer of Liquids," Journal of Applied Physics, Vol. 106, pp. 084907-1-7.

Eissing, T., Conzelmann, H., Gilles, E.D., Allgöwer, F. and Bullinger, E. and Scheurich, P., 2004, "Bistability Analyses of a Caspase Activation Model for Receptor-Induced Apoptosis," J. Biol. Chem., Vol. 279, pp. 36892-36897.

Ellero, M., and Tanner, R. I., 2005, "SPH Simulations of Transient Viscoelastic Flows at Low Reynolds Number," J. Non-Newtonian Fluid Mech., Vol. 132, pp. 61-72.

Eskes, R., Desagher, S., Antonsson, B., and Martinou, J. C., 2000, "Bid Induces the Oligomerization and Insertion of Bax into the Outer Mitochondrial Membrane," Mol. Cell. Biol., Vol. 20, pp. 929-935.

Fife, J. P., Ozkan, H. E., Derksen, R. C., and Grewal, P. S., 2006, "Using Computational Fluid Dynamics to Predict Damage of a Biological Pesticide during Passage through a Hydraulic Nozzle," Biosystems Engineering, Vol. 94 (3), pp. 387-396.

Fitzgerald, T. N. Shepherd, B. R., Asada, H., Teso, D., Muto, A., Fancher, T., Pimiento, J. M., Maloney, S. P., and Dardik, A., 2008, "Laminar Shear Stress Stimulates Vascular Smooth Muscle Cell Apoptosis via the Akt Pathway," Journal of Cellular Physiology, Vol. 216(2), pp. 389-395.

Frenz, M., Paltauf, G., and Schmidt-Kloiber, H., 1996, "Laser-Generated Cavitation in Absorbing Liquid Induced by Acoustic Diffraction," Phys. Rev. Lett., Vol. 76(19), pp. 3546-3549.

Friedman, M., Strauss, M., Amendt, P., London, R. A., and Glinsky, M. E., 2002, "Two-Dimensional Rayleigh Model for Bubble Evolution in Soft Tissue," Physics of Fluids, Vol. 14(5), pp. 1768-1780.

Fussenegger, M., Bailey, J. E. and Varner, J., 2000, "A Mathematical Model of Caspase Function in Apoptosis," Nature Biotechnology, Vol. 18, 768-774.

Gautam, S. and Sharma, A., 2002, "Involvement of Caspase-3-like Protein in Rapid Cell Death of Xanthomonas," Mol Microbiol, Vol. 44, pp. 393-401.

Geddes-Klein, D. M., Schiffman, K. B., and Meaney, D. F., 2006, "Mechanisms and Consequences of Neuronal Stretch Injury In Vitro Differ with the Model of Trauma," Journal of Neurotrauma, Vol. 23(2), pp. 193-204.

Georgiou, S., and Koubenakis, A., 2003, "Laser-Induced Material Ejection from Model Molecular Solids and Liquids: Mechanisms, Implications, and Applications," Chem. Rev., Vol.103 (2), pp. 349-393.

Gerstman, B. S., Thompson, C. R., Jacques, S. L., and Rogers, M. E., 1996, "Laser Induced Bubble Formation in the Retina," Lasers in Surgery and Medicine, Vol. 18, pp. 10-21.

Gingold, R. A., and Monaghan, J. J., 1977, "Smoothed Particle Hydrodynamics: Theory and Application to Non-Spherical Stars," Monthly Notices Royal Astronomical Society, Vol. 181, pp. 375-389.

Glinsky, M. E., Bailey, D. S., London, R. A., Amendt, P. A., Rubenchik, M. R. and Strauss, M., 2001, "An Extended Rayleigh Model of Bubble Evolution," Phys, Fluids, Vol. 13(20), pp. 20-31.

Grigioni, M., Morbiducci, U., D'Avenio, G., Benedetto, G. D. and Gaudio, C. D., 2005, "A Novel Formulation for Blood Trauma Prediction by a Modified Power-Law Mathematical Model," Biomech Model Mechanbiol, Vol. 4, pp. 249-260.

Gusev, V. E., and Karabutov, A. A., 1993, "Laser Optoacoustics," American Institute of Physics, New York.

Haller, K. K., Ventikos, Y., Poulikakos, D., and Monkewitz, P., 2002, "Computational Study of High-Speed Liquid Droplet Impact," Journal of Applied Physics, Vol. 92(5), pp. 2821-2828.

Hengartner, M. O., 2000, "The Biochemistry of Apoptosis," Nature, Vol. 407, pp. 770-776.

Hopp, B., Smausz, T., Kresz, N., Barna, N., Bor, Z., Kolozsvari, L., Chrisey, D. B., Szabo, A., and Nogradi, A., 2005, "Survival and Proliferative Ability of Various Living Cell Types after Laser-Induced Forward Transfer," Tissue Eng., Vol. 11(11/12), pp. 1817-1723.

Huang, H., Kamm, R. D., and Lee, R. T., 2004, "Cell Mechanics and Mechanotransduction: Pathways, Probes, and Physiology," Am J Physiol Cell Physiol, Vol. 287, pp. C1-C11.

Jayasinghe, S. N., Eagles, P. A., and Qureshi, A. N., 2006, "Electric Field Driven Jetting: an Emerging Approach for Processing Living Cells," Biotechnol J., Vol. 1, pp. 86-94.

Johnson, G. R., Stryk, R. A., and Neissel, S. R., 1996, "SPH for High Velocity Impact Computations," Compu. Methods Appl. Mech. and Engrg., Vol. 139, pp. 347-373.

Jost, P. J., Grabow, S., Gray, D., McKenzie, M. D., Nachbur, U., Huang, D. C. S., Bouillet, P., Thomas, H. E., Borner, C., Silke, J., Strasser, A., and Kaufmann, T., 2009, "XIAP Discriminates between Type I and Type II FAS-Induced Apoptosis," Nature, Vol. 460, pp. 1035-1039.

Kasza, K. E., Rowat, A. C., Liu, J., Angelini, T. E., Brangwynne, C. P., Koenderink, G. H., and Weitz, D. A., 2007, "The Cell as a Material," Current Opinion in Cell Biology, Vol. 19, pp. 101-107.

Kim, D., Ye, M., and Grigoropoulos, C. P., 1998, "Pulsed Laser-induced Ablation of Absorbing Liquids and Acoustic-Transient Generation," Appl. Phys. A., Vol. 67, pp. 169-181.

Kulms, D., Pöppelmann, B., Yarosh, D., Luger, T. A., Krutmann, J. and Schwarz, T., 1999, "Nuclear and Cell Membrane Effects Contribute Independently to the Induction of Apoptosis in Human Cells Exposed to UVB Radiation," Proc. Natl. Acad. Sci. USA, Vol. 96, pp. 7974-7979.

Lacour, S., Hammann, A., Grazide, S., Lagadic-Gossmann, L., Athias, A., Sergent, O., Laurent, G., Gambert, P., Solary, E., and Dimanche-Boitrel, M. T., 2004, "Cisplatin-Induced CD95 Redistribution into Membrane Lipid Rafts of HT29 Human Colon Cancer Cells," Cancer Research, Vol. 64, pp. 3593-3598.

Lanero, T. S, Cavalleri, O., Krol, S., Rolandi, R., and Gliozzi A., 2006, "Mechanical Properties of Single Living Cells Encapsulated in Polyelectrolyte Matrixes," Journal of Biotechnology, Vol. 124, pp. 723-731.

Lee, S., McAuliffe, D. J., Zhang, H., Xu, Z., Taitelbaum, J. Flotte, T. J. and Doukas, A. G., "Stress Wave Induced Membrane Permeation of Red Blood Cells is Facilitated by Aquaporins," Ultrasound in Med. & Biol, Vol. 23(7), pp. 1089-1094.

Lee, S. and Doukas, A. G., 1999, "Laser-Generated Stress Waves and Their Effects on the Cell Membrane," IEEE Journal of Selected Topics in Quantum Electronics, Vol. 5(4), pp. 997-1003.

Legewie, S., Blüthgen, N., and Herzel, H., 2006, "Mathematical Modeling Identifies Inhibitors of Apoptosis as Mediators of Positive Feedback and Bistability," PLos Computational Biology, Vol. 2, pp. 1061-1073.

Leverett, L. B., Hellums, J. D., Alfrey, C. P. and Lynch, E. C., 1972, "Red Blood Cell Damage by Shear Stress," Biophysical Journal, Vol. 12, pp. 257-273.

Lim, C. T., Zhou, E. H., and Quek, S. T., 2006, "Mechanical Models for Living Cells—a Review," Journal of Biomechanics, Vol. 39, pp. 195-216.

Lin, Y., Huang, Y., Wang, G., Tzeng, T. J., and Chrisey, D. B., 2009a, "Effect of Laser Fluence on Yeast Cell Viability in Laser-Assisted Cell Transfer," J. of Applied Physics, Vol. 106(4), pp. 043106-1-7.

Lin, Y., Huang, Y., and Chrisey, D. B., 2009b, "Droplet Formation in Matrix-Assisted Pulsed-Laser Evaporation Direct Writing of Glycerol-Water Solution," J. of Applied Physics, Vol. 105, pp. 093111-1-6.

Lin, Y., Huang, G., Huang, Y., Tzeng, T. J., and Chrisey, D. B., 2010a, "Effect of Laser Fluence in Laser-Assisted Direct Writing of Human Colon Cancer Cell," Rapid Prototyping Journal, Vol. 16(3), pp. 202-208.

Lin, Y., Huang, G., Huang, Y., Tzeng, T. J., and Chrisey, D. B., 2010b, "Process-Induced Cell Injury in Laser Direct Writing of Human Colon Cancer Cells," Tissue Engineering C, in press.

Lin, D. C., Yurke, B., and Langrana, N. A., 2004, "Mechanical Properties of a Reversible, DNA-Crosslinked Polyacrylamide Hydrogel," Journal of Biomechanical Engineering, Vol. 126, pp. 104-110.

Liu, M. B., Liu, G. R., and Lam, K. Y., 2002, "Investigations into Water Mitigation Using a Meshless Particle Method," Shock Waves, Vol. 12, pp. 181-195.

Liu, M. B., Liu, G. R., Lam, K. Y., and Zong, Z., 2003, "Meshfree Particle Simulation of the Detonation Process for High Explosives in Shaped Charge Unlined Cavity Configurations," Shock Waves, Vol. 12, pp. 509-520.

Lokhandwalla, M. and Sturtevant, B., 2001, "Mechanical Haemolysis in Shock Wave Lithotripsy (SWL): I. Analysis of Cell Deformation Due to SWL Flow-Fields," Phys. Med. Biol., Vol. 46, pp. 413-437.

LS-DYNA Theory Manual, 2006, Livermore Software Technology Corporation, Livermore, California.

LS-DYNA Keyword User's Manual, 2007, Livermore Software Technology Corporation, Livermore, California.

Lucy, L. B., 1977, "A Numerical Approach to the Testing of Fusion Process," Astronomical Journal, Vol. 88, pp. 1013-1024.

Lysne, P. C., 1970, "A Comparison of Calculated and Measured Low-Stress Hugoniots and Release Adiabats of Dry and Water-Saturated Tuff," J. Geophys. Res., Vol. 75, pp. 4375-4386.

Malvern, L. E., 1969, "Introduction of the Mechanics of a Continuous Medium," Prentice-Hall, Inc. Englewood Cliffs, New Jersey.

Mardikar, S. H., and Niranjan, K., 2000, "Observations on the Shear Damage to Different Animal Cells in a Concentric Cylinder Viscometer," Biotechnol. Bioeng. Vol. 68, pp. 697-704.

McAuliffe, D. J., Lee, S., Flotte, T. J. and Doukas, A. G., 1997, "Stress-Wave-Assisted Transport through the Plasma Membrane In Vitro," Laser in Surgery and Medicine, Vol. 20, pp. 216-222.

Midler, Jr. M., and Finn, R. K., 1966, "A Model System for Evaluating Shear in the Design of Stirred Fermentors," Biotechnology and Bioengineering, Vol. 8, pp. 71-84.

Monaghan, J. J., and Gingold, R. A., 1983, "Shock Simulation by the Particle Method SPH," Journal of Computational Physics. Vol. 52, pp. 374-389.

Nam, K., Watanabe, J., and Ishihara, K., 2005, "Network Structure of Spontaneously Forming Physically Cross-Link Hydrogel Composed of Two-Water Soluble Phospholipid Polymers," Polymer, Vol. 46, pp. 4704-4713.

Noack, J., and Vogel, A., 1999, "Laser-Induced Plasma Formation in Water at Nanosecond to Femtosecond Time Scales: Calculation of Thresholds, Absorption Coefficients, and Energy Density," IEEE J. Quantum Electron., Vol. 35(8), pp. 1156-1167.

Odde, D. J., and Renn, M. J., 2000, "Laser-Guided Direct Writing of Living Cells," Biotech. and Bioeng., Vol. 67(3), pp. 312-318.

Ohayon, J. and Tracqui, P., 2005, "Computation of Adherent Cell Elasticity for Critical Cell-Bead Geometry in Magnetic Twisting Experiments," Annals of Biomedical Engineering, Vol. 33(2), pp. 131-141.

O'Sullivan, M., O'Leary, S., Kelly, D. M., and Keane, J., 2007, "A Caspase-Independent Pathway Mediates Macrophage Cell Death in Response to Mycobacterium tuberculosis Infection," Infection and Immunity, Vol. 75, pp. 1984-1993.

Paltauf, G., and Schmidt-Kloiber, H., 1997, "Measurement of Laser-Induced Acoustic Waves with a Calibrated Optical Transducer," J. Appl. Phys., Vol. 82 (4), pp. 1525-1531.

Paltauf, G., and Schmidt-Kloiber, H., 1998, "Photoacoustic Waves Excited in Liquids by Fiber-Transmitted Laser Pulses," J. Acoust. Soc. Am., Vol. 104 (2), pp. 890-897.

Paltauf, G., and Dyer, P. E., 2003, "Photomechanical Process and Effects in Ablation," Chem. Rev., Vol. 103(2), pp. 487-518.

Park, H. K., 1994, "Heat and Momentum Transfer on the Rapid Phase Change of Liquid Induced by Nanosecond-Pulsed Laser Irradiation," University of California, Berkeley, Ph.D. Dissertation.

Park, H. K., Kim, D., Grigoropoulos, C. P., and Tam, A. C., 1996, "Pressure Generation and Measurement in the Rapid Vaporization of Water on a Pulsed-Laser-Heated Surface," J. Appl. Phys., Vol. 80(7), pp. 4072-4081.

Pini, R., Fossi, F., Salimbeni, R., Siano, S., Vannini, M., Carones, F., Trabucchi, G., Brancato, R. and Gobbi, P. G., 1996, "Experimental Investigation on Acoustic Phenomena Induced inside the Eyeball by Excimer Laser Ablation of the Cornea," Proc. SPIE, Vol. 2632, pp. 25-29.

Plesset, M. S., and Prosperetti, A., 1977, "Bubble Dynamics and Cavitation," Ann. Rev. Fluid Mech., Vol. 9, pp. 145-185.

Rice, K. C. and Bayles, K. W., 2003, "Death's Toolbox: Examining the Molecular Components of Bacterial Programmed Cell Death," Mol Microbiol, Vol. 50, pp. 729-738.

Ringeisen, B. R., Kim, H., Barron, J. A., Krizman, D. B., Chrisey, D. B., Jackman, S., Auyeung, R. Y. C., and Spargo, B. J., 2004, "Laser Printing of Pluripotent Embryonal Carcinoma Cells," Tissue Eng., Vol. 10(3-4), pp. 483-491.

Ringeisen, B. R., Othon, C. M., Barron, J. A., Young, D., and Spargo, B. J., 2006, "Jet-Based Methods to Print Living Cells", Biotechnol. J., Vol. 1, pp. 930-948.

Rioboo, R., Bauthier, C., Conti, J., Voue, M., and De Coninck, J., 2003, "Experimental Investigation of Splash and Crown Formation during Single Drop Impact on Wetted Surfaces," Exp. Fluids, Vol.35, pp. 648-652.

Rock, K. L., 2008, "Pathobiology of Inflammation to Cell Death," Biol Blood Marrow Transplant, Vol. 15, pp. 137-138.

Roeder, B. A., Kokini, K., Sturgis, J. E., Robinson, J. P., and Voytik-Harbin, S. L., 2002, "Tensile Mechanical Properties of Three-Dimensional Type I Collagen Extracellular Matrices with Varied Microstructure," Journal of Biomechanical Engineering, Vol. 124, pp. 214-222.

Rylander, M. N., Feng Y., Bass, J. and Diller, K. R., 2004, "Thermally Induced Injury and Heat-Shock Protein Expansion in Cells and Tissues," Ann. N.Y. Acad. Sci., Vol. 1066, pp. 222-242.

Sahoo, S., Rao, K. K., and Suraishkumar, G. K., 2006, "Reactive Oxygen Species Induced by Shear Stress Mediate Cell Death in Bacillus subtilis," Biotechnology and Bioengineering, Vol. 94, pp. 118-127.

Scaffidi, C., Fulda, S., Srinivasan, A., Friesen, C., Li, F., Tomaselli, K. J., Debatin, K. M., Krammer, P. H. and Peter, M. F., 1998, "Two CD95 (APO-1/Fas) Signaling Pathways," The EMBO Journal, Vol. 17, pp. 1675-1687.

Scoltock, A. B. and Cidlowski, J. A., 2004, "Activation of Intrinsic and Extrinsic Pathways in Apoptotic Signaling during UV-C-Induced Death of Jurkat Cells: the Role of Caspase Inhibition," Experimental Cell Research, Vol. 297, pp. 212-223.

Serbest, G., Horwitz, J., Jost M., and Barbee, K., 2006, "Mechanisms of Cell Death and Neuroprotection by Poloxamer 188 after Mechanical Trauma," FASEB J., Vol. 20, pp. 308-310.

Shive, M. S., Brodbeck, W. G., and Anderson, J. M., 2002, "Activation of Caspase 3 during Shear Stress-Induced Neutrophil Apoptosis on Biomaterials," J Biomed Mater Res Part A, Vol. 62, pp. 163-168.

Sigrist, M. W., and Kneubühl, F. K., 1978, "Laser-Generated Stress Waves in Liquids," J. Acoust. Soc. Am., Vol. 64(6), pp. 1652-1663.

Smith, A. E., Moxham, K. E., and Middelberg, A. P. J., 2000, "Wall Material Properties of Yeast Cells. Part II. Analysis," Chemical Engineering Science, Vol. 55, pp. 2043-2053.

Stammen, J. A., Williams, S., Ku, D. N., and Guldberg, R. E., 2001, "Mechanical Properties of a Novel PVA Hydrogel in Shear and Unconfined Compression," Biomaterials, Vol. 22, pp. 799-806.

Sundaram, J., Mellein, B. R., and Mitragotri, S., 2003, "An Experimental and Theoretical Analysis of Ultrasound-Induced Permeabilization of Cell Membranes," Biophysical Journal, Vol. 84, pp. 3087-3101.

Tomita, Y., Tsubota, M. and An-naka, N., 2003, "Energy Evaluation of Cavitation Bubble Generation and Shock Wave Emission by Laser Focusing in Liquid Nitrogen," Journal of Applied Physics, Vol. 93(5), pp. 3039-3048.

Tschumperlin, D. J., Oswari, J., and Margulies, S. S., 2000, "Deformation-Induced Injury of Alveolar Epithelial Cells: Effect of Frequency, Duration, and Amplitude," Am. J. Respir. Crit. Care Med., Vol. 162, pp. 357-362.

Tzima, E., Irani-Tehrani, M., Kiosses, W. B., Dejana, E., Schultz, D. A., Engelhardt, B., Cao, G., DeLisser, H. and Schwartz, M. A., 2005, "A Mechanosensory Complex that Mediates the Endothelial Cell Response to Fluid Shear Stress," Nature, Vol. 437, pp. 426-431.

Vijayasekaran S., Fitton J. H., Hicks C.R., Chirila T. V., Crawford, G. J., and Constable, I. J., 1998, "Cell Viability and Inflammatory Response in Hydrogel Sponges Implanted in the Rabbit Cornea," Biomaterials, Vol. 19(24), pp. 2255-2267.

Vogel, A., Busch, S., and Parlitz, U., 1996, "Shock Wave Emission and Cavitation Bubble Generation by Picosecond and Nanosecond Optical Breakdown in Water," J. Acoust. Soc. Am., Vol. 100(1), pp.148-165.

Vogel, A., and Venugopalan, V., 2003, "Mechanisms of Pulsed Laser Ablation of Biological Tissues," Chem. Rev., Vol. 103(2), pp. 577-644.

Wang, A. B. and Chen, C. C., 2000, "Splashing Impact of a Single Drop onto Very Thin Liquid Films," Phys. Fluids, Vol. 12, pp. 2155-2158.

Wang, T., Turhan, M., and Gunasekaran, S., 2004, "Selected Properties of pH-Sensitive, Biodegradable Chitosan-Poly (vinyl alcohol) Hydrogel," Polym. Int., Vol. 53, pp. 911-918.

Wang, W., Huang, Y., and Chrisey, D. B., 2007, "Numerical Study of Cell Droplet and Hydrogel Coating Impact Process in Cell Direct Writing," Transactions of NAMRI/SME, Vol. 35, pp. 217-223.

Wang, W., Huang, Y., Grujicic, M., and Chrisey, D. B., 2008, "Study of Impact-Induced Mechanical Effects in Cell Direct Writing Using Smooth Particle Hydrodynamic Method," ASME J. of Manufacturing Sci. and Eng., Vol. 130(2), pp. 021012-1-10.

Wang, W., Li, G., and Huang, Y., 2009a, "Modeling of Bubble Expansion-Induced Cell Mechanical Profile in Laser-Assisted Cell Direct Writing," ASME J. of Manufacturing Sci. and Eng., Vol. 131(5), pp. 051013-1-10.

Wang, W., Huang, Y., and Lin, Y., 2009b, "Modeling of Thermoelastic Stress Wave in Laser-Assisted Cell Direct Writing," Proceedings of the ASME 2009 International Manufacturing Science and Engineering Conference (MSEC2009), West Lafayette, Indiana, USA, MSEC2009-84373, pp. 1-8, October 4-7.

Wilson, W. C., and Boland, T., 2003, "Cell and Organ Printing 1: Protein and Cell Printers," Anat. Rec. Part A, Vol. 272A, pp. 491-496.

Xu, L., Zhang, W. W., and Nagel, S. R., 2005b, "Drop Splashing on a Dry Smooth Surface," Phys. Rev. Lett., Vol. 94, Vol. 184505-1-4.

Xu, T., Petridou, S., Lee, E. H., Roth, E. A., Vyavahare, N. R., Hickman, J. J., and Boland, T., 2004, "Construction of High-Density Bacterial Colony Arrays and Patterns by the Ink-Jet Method," Biotechnol. Bioeng., Vol. 85(1), pp. 29-33.

Xu, T., Jin, J., Gregory, C., Hickman, J. J., and Boland, T. 2005a, "Inkjet Printing of Viable Mammalian Cells," Biomaterials, Vol. 26, pp. 93-99.

Yamaguchi, T., Hashiguchi, K., Katsuki, S., Iwamoto, W., Tsuruhara, S. and Terada, S., 2008, "Activation of the Intrinsic and Extrinsic Pathways in High Pressure-induced Apoptosis of Murine Erythroleukemia Cells," Cellular & Molecular Biology Letters, Vol. 13, pp. 49-57.

Yarin, A. L., and Weiss, D. A., 1995, "Impact of Drops on Surfaces: Self-similar Capillary Waves, and Splashing as a New Type of Kinematic Discontinuity," J. Fluid Mech., Vol. 283, pp. 141-173.

Young, C. D., Wu, J. R., and Tsou, T. L., 1998, "High-Strength, Ultra-Thin and Fiber-Reinforced pHEMA Artificial Skin," Biomaterials, Vol. 19, pp. 1745-1752.

Young, D., Auyeung, R. C. Y., Piqué, A., Chrisey, D. B., and Dlott, D. D., 2001, "Time-Resolved Optical Microscopy of a Laser-Based forward Transfer Process," Appl. Phys. Lett., Vol. 78, pp. 3169-3171.

Zhang, T., Brazhnik, P. and Tyson, J. J., 2009, "Computational Analysis of Dynamical Responses to the Intrinsic Pathway of Programmed Cell Death," Biophysical Journal, Vol. 97, pp. 415-434.